

**ENERGY YIELD CALCULATIONS FOR SILICON-  
BASED TANDEM SOLAR CELLS**

**LIU HAOHUI**

*B.Eng. (Engineering Science, First Class Honours), NUS*

**A THESIS SUBMITTED**

**FOR THE DEGREE OF DOCTOR OF PHILSOPHY**

**NUS GRADUATE SCHOOL FOR INTEGRATIVE SCIENCES AND  
ENGINEERING**

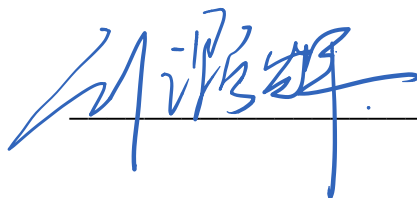
**NATIONAL UNIVERSITY OF SINGAPORE**

**2016**

## **DECLARATION**

I hereby declare that this thesis is my original work and it has been written by me in its entirety. I have duly acknowledged all the sources of information which have been used in the thesis.

This thesis has also not been submitted for any degree in any university previously.

 7 Dec 2016

**LIU Haohui**

**7 December 2016**

## ACKNOWLEDGEMENTS

I am deeply grateful to all the people who have supported me during the course of my PhD study.

Firstly, I would like to extend my deepest gratitude to my supervisors, Prof. Armin Aberle and Dr. Ian Marius Peters for their continuous support and valuable guidance. I have benefited enormously from their knowledge and deep insights in the field of solar energy and solar cell research. They never failed to provide timely feedback and help that I needed. I also thank Prof. Ho Ghim Wei and Prof. Feng Yuan Ping in my Thesis Advisory Committee for their time and feedback in evaluating my work.

I would like to thank Prof. Tonio Buonassisi and other close collaborators from Massachusetts Institute of Technology (MIT) and Singapore-MIT Alliance for Research and Technology (SMART). Tonio was both a good friend and an excellent mentor, from whom I received tremendous motivation and intellectual stimulus. I thank Dr Jonathan P. Mailoa, Sarah Sofia, Dr Siah Sin Cheng, Sterling Watson, and Felipe Oviedo from MIT. I also thank Dr Nasim Sahraei, and (especially) Ren Zekun from SMART for working closely to develop the physical models. I enjoyed working with them. I also had a lot of fun with our team building activities. Without them my work would not have been possible.

Many thanks to my colleagues in Solar Energy Research Institute of Singapore (SERIS): Liu Zhe, Dr Ke Cangming, Wang Puqun, Dr Ma Fajun, Li Mengjie, Dr Guo Siyu, Gautam Anand, and Dr Yang Dazhi for their helpful discussion, pleasant friendship and joyful company. Special thanks to Dr André Nobre for providing me the data used in my studies. I would also like to thank Dr. Rolf Stangl and Dr. Lin Fen from SERIS for their

advice and care. I personally thank my friends Zhao Xiahong and Pang Long for providing tips on the subject of statistics.

I truly appreciate NUS Graduate School for Integrative Sciences and Engineering (NGS) for awarding me a PhD scholarship, and SERIS for providing all the convenience and facility for my research work.

Finally, I would like to thank my beloved parents for their warm support, for helping me establish my own family, and for their kind understanding when I was not able to accompany and take care of them for the most part of my PhD life. I would also like to thank my adoring wife, Hu Meibo. Her support and company kept me strong and happy.

# Table of Contents

ACKNOWLEDGEMENTS .....	ii
Table of Contents .....	iv
Summary .....	vii
Table of figures .....	ix
Nomenclature .....	xviii
Chapter 1. Introduction.....	1
1.1. Motivation.....	1
1.2. Objectives .....	4
1.3. Thesis structure .....	6
Chapter 2. Backgrounds of Si based tandem solar cells and energy yield calculations .....	8
2.1. Basics of solar cells and the multi-junction concept.....	8
2.1.1. Principles of solar cell operation.....	8
2.1.2. Multi-junction solar cells: Going beyond the Shockley-Queisser limit.....	13
2.2. Overview of Si based tandem solar cells .....	23
2.3. Energy yield analysis .....	27
2.3.1. Standard testing condition (STC) and its limitations .....	27
2.3.2. Key questions of energy yield analysis.....	29
2.3.3. Prevailing practices of energy yield analysis.....	31
2.3.4. Specific considerations for flat-plate tandem solar cells .....	36
2.4. Chapter summary .....	37
Chapter 3. Realistic outdoor operating conditions .....	39
3.1. Measurements of outdoor conditions.....	39
3.1.1. Solar irradiance level measurements .....	40
3.1.2. Solar spectrum measurements .....	44

3.2.	Analysis of outdoor operation conditions .....	46
3.2.1.	Irradiance levels .....	46
3.2.2.	Spectral compositions .....	48
3.2.3.	Distribution map of illumination conditions .....	55
3.2.4.	Operating temperatures and others .....	57
3.3.	Year to year variations .....	58
3.4.	Chapter summary .....	60
Chapter 4.	Modelling of tandem solar cells and their efficiencies under various conditions .....	62
4.1.	Simulation framework .....	63
4.1.1.	Overview .....	63
4.1.2.	Device models for Si bottom cell .....	66
4.1.3.	Device models for III-V top cells .....	69
4.2.	Tandem models and efficiencies under STC .....	71
4.2.1.	Double-junction efficiencies for various sub-cell combinations .....	71
4.2.2.	Tandem models for energy yield calculations .....	73
4.3.	Tandem efficiencies under non-standard conditions .....	75
4.3.1.	Efficiencies under varying spectra and light intensity .....	75
4.3.2.	Temperature coefficients of tandem solar cells .....	78
4.3.3.	Operating temperatures .....	79
4.4.	Chapter summary .....	82
Chapter 5.	New methodology for energy yield calculation and outdoor loss analysis of tandem solar cells .....	85
5.1.	Fast yield calculation algorithm .....	86
5.2.	Theories and framework for outdoor loss analysis .....	90
5.2.1.	Quantification of outdoor losses .....	90

5.2.2.	Methodology for breaking down outdoor losses .....	92
5.3.	Impact of input illumination conditions.....	93
5.3.1.	Sources of input illumination conditions .....	93
5.3.2.	Calculation set up.....	95
5.3.3.	Effect of temporal resolution .....	96
5.3.4.	Effect of input spectrum .....	101
5.4.	Chapter summary .....	102
Chapter 6.	Energy yield of 1-Sun tandem solar cells and implications on design rules .....	104
6.1.	Time resolved energy yields for GaAs/Si tandem solar cells .....	104
6.1.1.	Device structure and simulation setup .....	105
6.1.2.	Time series of yield and discussion .....	106
6.1.3.	The influence of photon recycling and luminescent coupling .....	112
6.2.	Annual harvesting efficiency and outdoor loss analysis.....	114
6.2.1.	Summary of annual harvesting efficiencies and outdoor losses .....	114
6.2.2.	Implication on performance ratio.....	117
6.2.3.	Variation over the years .....	120
6.3.	Implications on design .....	121
6.4.	Chapter summary .....	123
Chapter 7.	Conclusion .....	126
7.1.	Summary .....	126
7.2.	Proposed future work.....	130
	Bibliography .....	133
	Appendix 1: Publications.....	143
	Appendix 2: MatLab code for yield calculation .....	145

## Summary

Silicon (Si) based tandem solar cells are promising in achieving the next quantum leap in flat-plate PV efficiency in a cost-effective way. While much efforts have been spent on their efficiency improvement under standard testing conditions, little investigation has been carried out on their realistic outdoor energy yield potentials. Also, accurate energy yield calculation methods that take secondary effects (such as the actual solar spectrum) into account are not extensively developed in the literature, despite the fact that they are important in the design of tandem solar cells and modules. This PhD thesis evaluates the outdoor energy yield potential and loss characteristics in two locations (Singapore and Denver) representing very different climates, using an elaborate energy yield calculation method that employs physical device simulation and detailed data on operating conditions. Measured solar irradiance levels, solar spectra, and air temperature data are processed and analysed. Solar cell outputs under different illumination conditions and temperatures are modelled for several III-V-on-Si (III-V/Si) tandem configurations. Based on these results, the annual energy yields are calculated and the outdoor losses are quantified. It is found that the more accurate yield calculation method can predict outdoor efficiency losses better than crude estimations, which produce about relative 20% to 60% error. In addition, the irradiance level, spectral composition and operating cell temperature are observed to be significantly different for the two investigated locations. This results in different predicted tandem solar cell performances, with losses in outdoor efficiency in Singapore about twice as much as those in Denver. Overall, the investigated III-V/Si tandem solar cells show more spectrum sensitivity (which lead to performance ratio drop as much as 5% absolute in



Singapore) but better temperature tolerance. In both locations, the performance ratios of III-V/Si tandem solar cells are expected to be as good, or even better, than those of conventional single-junction Si solar cells.

## List of figures

Figure 1.1.1: Learning curve for module price as a function of cumulative PV module shipments. Figure adopted from ITRPV 2016 [5]. .....	2
Figure 2.1.1: General structure of a solar cell as illustrated in PV Education [15]. Electron-hole pairs are generated by sunlight. The generated electrons and holes are separately collected by the front contact and the rear contact to drive the external circuit. ....	10
Figure 2.1.2: Equivalent circuit model of a solar cell, excerpt from [3]......	11
Figure 2.1.3: Relative spectral responses of various PV technologies (multicrystalline Si, amorphous Si, CdTe and CIGS), measured under STC temperature (25°C). The AM1.5G spectrum (grey) is also shown for reference.....	12
Figure 2.1.4: Illustration of the spectrum splitting concept. Spectrum splitting can be done via (a) spatial configuration, or (b) stacked configuration. The distribution of photons in the standard solar spectrum is shown in the top part. Different portions of light are absorbed in sub-cells with different bandgaps.....	15
Figure 2.1.5: Illustration of 2-terminal (2T) or 4-terminal (4T) configuration for connecting the sub-cells in a tandem solar cell.....	16
Figure 2.1.6: Theoretical dual-junction efficiency limit for 4-terminal configuration (case a). The global maximum occurs at the bandgap combination of 1.73 eV and 0.95 eV. For bandgap combination of GaAs (1.42 eV) and Si (1.1 eV), the efficiency limit is 42%.....	19
Figure 2.1.7: Theoretical dual-junction efficiency limit for 2-terminal configuration without top cell thinning (case b). The global maximum occurs at the	

bandgap combination of 1.6 eV and 0.93 eV. Another local maximum with nearly as high efficiency occurs at the combination of 1.73 eV and 1.13 eV. Efficiency drops off rapidly as top bandgap decreases towards bottom bandgap. For bandgap combination of GaAs (1.42 eV) and Si (1.1 eV), the efficiency limit is 23%..... 20

Figure 2.1.8: Theoretical efficiency limit for 2-terminal configuration with top cell thinning to enable current matching (case c). The global maximum occurs at the bandgap combination of 1.6 eV and 0.93 eV. Another local maximum with nearly as high efficiency occurs at the combination of 1.73 eV and 1.13 eV. For bandgap combination of GaAs (1.42 eV) and Si (1.1 eV), the efficiency limit is 39%..... 21

Figure 2.1.9: Schematics of a typical GaInP/Ga(In)As/Ge multi-junction solar cell. The sub-cells are series connected by tunnel junctions. A/R represents antireflection coating. Figure is adopted from [32]. ..... 22

Figure 2.2.1: Some published efficiency values of Si based tandem solar cells of different categories. Some values are reported under different test conditions (such as AM0 spectrum, or concentrated illumination), therefore should only be taken as a rough indication of efficiency levels. In 2016, tandem solar cells reaching 30% 1-Sun (AM1.5G) efficiency have been fabricated in the laboratory (Fraunhofer ISE and NREL)..... 26

Figure 2.3.1: Illustration of the breakdown of performance ratio related losses for a typical commercial Si-based PV system in Singapore. The typical outdoor losses and their usual contributions are shown. Figure is adopted from National Solar Repository of Singapore [61]. ..... 29

Figure 3.1.1: The PV Monitoring Lab in SERIS. A variety of meteorological parameters such as instantaneous solar irradiance level, spectrum, wind speed, ambient temperature, and real-time performance of PV systems are measured and monitored. .... 42

Figure 3.1.2: The Solar Radiation Research Laboratory, Baseline Measurement System is a facility supporting NREL's resource assessment and forecasting research. The Baseline Measurement System has a large collection of radiometers that record surface meteorological conditions. .... 43

Figure 3.2.1: The daily irradiance level profile for (a) a clear and sunny day in Denver during February 2013, and (b) a partially sunny day with occasional cloud coverage in Singapore during February 2013. .... 47

Figure 3.2.2: Distribution of solar insolation with respect to irradiance levels for (a) Singapore and (b) Denver. .... 48

Figure 3.2.3: The average spectrum of Singapore and Denver, derived from measured data in the year 2013, shown together with the AM1.5G spectrum. The spectra are all normalized to the same intensity in the wavelength range of 350 nm to 1060 nm. .... 49

Figure 3.2.4: Characteristic set of spectra in (a) Singapore and (b) Denver. All spectra are scaled to the same intensity as the standard AM1.5G spectrum. The APE values indicate the left bound of the interval. .... 51

Figure 3.2.5: Distribution of solar insolation with respect to APE for (a) Singapore and (b) Denver. .... 52

Figure 3.2.6: The time series of (a) irradiance level and (b) APE value for an average day in Singapore. The data points marked blue in (b) correspond to those marked blue in (a). In general, APE values rise when there is a dip in the irradiance level..... 53

Figure 3.2.7: The daily average APE value of the spectra versus daily insolation in the year of 2014 for (a) Singapore, and (b) Denver. APE seems to be correlated negatively to insolation in a roughly linear way for Singapore. The correlation is more complicated in the case of Denver, where seasonal variations of climate and sun positions are more prominent..... 53

Figure 3.2.8: Annual occurrence distribution of illumination conditions for (a) Singapore and (b) Denver in the year 2013. .... 56

Figure 3.2.9: The distribution of insolation content with respect to APE and intensity levels for Singapore (left) and Denver (right) in the year 2013. .... 57

Figure 3.2.10: The distribution of annual insolation content with respect to the ambient air temperature for (a) Singapore and (b) Denver in the year 2013. .... 58

Figure 3.3.1: Comparison of insolation distribution with different spectral compositions across three years, 2013 to 2015, in Singapore. .... 59

Figure 3.3.2: Comparison of insolation distribution with different spectral compositions across three years, 2013 to 2015, in Denver..... 60

Figure 4.1.1: The process flow for simulating a tandem solar cell (left), and the 1D schematics of the tandem device structures to be simulated (right). Both 2-terminal (2T) and 4-terminal (4T) configurations are investigated. The insulator layer in 4T is only conceptual and has zero thickness in the simulated device structure. .... 64

Figure 4.2.1: Simulated STC efficiencies for 2T and 4T double-junction tandem solar cells with different sub-cell combinations. The typical single-junction cell efficiencies using individual sub-cell technologies are indicated as green lines. The tandem configurations written in red text along the horizontal axis are selected for further energy yield studies..... 72

Figure 4.3.1: Simulated tandem solar cell efficiencies for (a) a 2T and (b) a 4T configuration under different spectral compositions (represented by the APE in eV) and light intensities (in suns). The calculated efficiencies range from 17% to 28% for 2T tandem cells and from 27% to 33% for 4T tandem cells..... 76

Figure 4.3.2: (a) The calculated operating temperature for a 19% efficient single-junction Si solar cell and for a 29% efficient double-junction tandem solar cell. The temperature difference (right axis) between the two types of solar cells, at 800 - 1000 W/m<sup>2</sup>, can be as much as 3 to 4 °C, which is significant. (b) The calculated operating temperature difference, at 1 Sun intensity, between a 19% Si solar cell and a tandem solar cell with varying efficiency..... 81

Figure 5.1.1: Time series of the calculated energy yield (blue line) of a 2-terminal GaAs/Si tandem solar cell during Feb 2013 in (a) Singapore and (b) Denver. The available solar irradiance is represented by the brown line. It can be seen that the cloudy nature of Singapore’s weather results in significantly more fluctuations in the energy yield compared to that of Denver. The integration time for the energy yield is 5 minutes. .... 86

Figure 5.1.2: Schematic flow of the algorithm used in calculating energy yield for tandem solar cells..... 88

Figure 5.2.1: Procedure for performing the outdoor loss analysis.....	92
Figure 5.3.1: Box plot of the errors of (a) daily, (b) weekly and (c) monthly losses in harvesting efficiencies of a 2-terminal GaAs/Si tandem solar cell in Singapore. The losses in harvesting efficiencies are calculated from measured spectra with different time resolutions (30 min, 1 hour, 2 hours), as well as from SMARTS generated spectra and their intensity modified version. The errors are represented by the relative deviation from the reference values calculated using the full simulation.....	97
Figure 5.3.2: Box plot of the errors in the calculated (a) daily, (b) weekly and (c) monthly losses in harvesting efficiencies of a 2-terminal GaAs/Si tandem solar cell in Denver.....	98
Figure 5.3.3: Box plot of the errors in the calculated (a) daily, (b) weekly and (c) monthly losses in harvesting efficiencies of a 2-terminal InGaP/Si tandem solar cell in Singapore. ....	99
Figure 6.1.1: Schematics of the three simulated GaAs/Si tandem solar cells..	105
Figure 6.1.2: Integrated spectral irradiance and simulated $2T$ GaAs/Si power as a function of sunshine hours for Sep 2013, in (a) Singapore and (b) Denver. Fluctuations in solar radiation are captured in fine detail. Two days of particular interest are highlighted for further comparison. ....	106
Figure 6.1.3: Simulated daily energy yield of the three investigated tandem solar cell configurations in (a) Singapore and (b) Denver, for September 2013. The integrated spectral irradiance (ISI) of the solar radiation and the theoretical output limit calculated using the detailed-balance method are also shown for comparison. The harvesting efficiency of the detailed-balance limit is shown in (c) for Singapore and (d) for Denver,	

together with the daily averaged average photon energy (APE) values. Taking the detailed-balance output as the benchmark, the performance of each configuration in (e) Singapore and (f) Denver is shown. The 2T configuration is significantly more sensitive to spectral variations, especially on days with low insolation. The two days of particular interest (days 2 and 10) for Singapore are circled in red in graph (e). ..... 107

Figure 6.1.4: Comparison of average solar spectra in Singapore on day 2 and day 10 of Feb 2013, for the wavelength range 300 to 1050 nm. The spectrum of day 10 is significantly blue shifted, causing larger current mismatch for the 2T tandem cell configuration. The AM1.5G spectrum is also shown for comparison. All three spectra were normalized to the same integrated spectral irradiance (ISI) of 761 W/m<sup>2</sup>, which corresponds to an intensity of 1000 W/m<sup>2</sup> for the complete wavelength range (280 nm to 4000 nm). ..... 110

Figure 6.1.5: Simulated average daily energy yield of 2T and 4T GaAs/Si tandem solar cells over 12 months (from Feb 2013 to Jan 2014) at two locations (Singapore and Denver). On average, the 4T output is more than 15% higher than the 2T output. .... 111

Figure 6.1.6: The ratio of the calculated energy output considering photon recycling ( $E_{\text{with PR}}$ ), and without photon recycling ( $E_{\text{w/o PR}}$ ) versus the APE of the input spectrum, in August 2013. The higher the APE values are, the greater the photon recycling effect is. Overall, the total energy yield increases by around 1% after including photon recycling in the calculation. .... 112

Figure 6.2.1: The breakdown of outdoor losses of Si based tandem solar cells with various III-V top cells, for the year 2014 in Singapore. The loss breakdown for single-



junction (SJ) GaAs and Si solar cells using the same device models is also included for comparison. The STC efficiencies and the final harvesting efficiencies taking into account the three losses are indicated in the graph. .... 114

Figure 6.2.2: The breakdown of outdoor losses of Si based tandem solar cells with various III-V top cells, for year 2014 in Denver. The spectral loss and temperature loss are much lower than in the case of Singapore. Several of the investigated tandem cell structures achieve better harvesting efficiency than a high-quality single-junction GaAs solar cell. .... 115

Figure 6.2.3: The predicted PR after taking into account the spectral effect, the low-irradiance effect, and the temperature effect for a single-junction Si and GaAs cell as well as several Si based tandem solar cells operating in Singapore. Single-junction GaAs and 4T InGaP/Si tandem solar cells experience a slight efficiency gain due to the blue-rich spectrum, which increases the PR to over 100%. .... 118

Figure 6.2.4: The predicted PR after taking into account the spectral effect, the low-irradiance effect, and the temperature effect for a single-junction Si and GaAs cell as well as several Si based tandem solar cells operating in Denver. The PR loss due to spectral effect and temperature effect are greatly reduced from Singapore's case. Low-irradiance loss is also slightly less. .... 118

Figure 6.2.5: The annual harvesting efficiency of a 2T GaAs/Si tandem cell in Denver, calculated for five years from 2011 to 2015. The harvesting efficiencies considering only loss from fluctuating illumination conditions show a variation of around 0.1%, where harvesting efficiencies considering both illumination conditions and temperatures show a variation of around 0.2%. .... 120

Figure 6.3.1: The loss breakdown for the various 2T III-V/Si tandem configurations before (striped) and after (solid) customizing for the local spectrum of Singapore. The improved harvesting efficiency is indicated in bold text. It should be noted that the STC efficiency would decrease due to these customizations. The improvement in the final harvesting efficiency is mainly due to a reduction in systematic current mismatch loss..... 122

## Nomenclature

$J_{sc}$	Short circuit current
$V_{oc}$	Open circuit voltage
FF	Fill factor
$T_c$	Cell operating temperature
$T_a$	Ambient air temperature
$k$	Ross coefficient
$G_T$	In-plane irradiance level
CPV	Concentration Photovoltaics
LCOE	Levelised Cost of Electricity
SR	Spectral Response
QE	Quantum Efficiency
STC	Standard Testing Condition
PR	Performance Ratio
TMY	Typical Meteorological Year
APE	Average Photon Energy
TC	Temperature Coefficient
ISI	Integrated Spectral Irradiance

# Chapter 1. Introduction

## 1.1. Motivation

Solar energy is one of the most promising sources of clean energy that can mitigate the risks of global climate change. Over the past few decades, solar cell efficiencies have increased remarkably [1]. Together with rapidly dropping costs, the global PV installations grew by more than 30 GW per year in recent years [2]. Silicon (Si) is one of the most abundant elements on Earth. Solar cells made from Si wafers dominate today's solar market, with a share of over 90% [3]. Efficient solar cells are also made from other materials such as gallium arsenide (GaAs), cadmium telluride (CdTe), and copper indium gallium diselenide (CIGS), in the form of thin-film solar cells. Most of these solar cells for terrestrial applications use non-concentrated light, and are also called 1-Sun or flat-plate solar cells. Another design that uses lenses or mirrors to concentrate sunlight onto small high-efficiency solar cells is called concentrator or concentration photovoltaics (CPV), and accounts for only a small fraction of total PV deployment. In most flat-plate applications, multiple solar cells are connected and encapsulated into a solar module, which is the basic unit for PV systems. The costs for solar cells or modules are commonly measured in dollar per watt peak ( $\$/W_p$ ), which is the manufacturing costs divided by the cell (or module) power under 1-Sun intensity (namely  $1000 \text{ W/m}^2$ , the typical intensity of sunlight at mid-day). At present, flat-plate solar cells and modules are comparatively cheaper and more versatile than their CPV counterparts [4]. The module costs have been dropping as installation capacities increased. Figure 1.1.1 illustrates this trend of declining module costs, which

is often regarded as the learning curve of the PV industry [5]. As a result, the portion of the solar cell related costs in the total PV system cost decreased significantly. Area related costs and costs associated with all other components necessary to build a PV system, which are lumped into the ‘balance of system’ (BOS) costs, now account for over half of the total cost [6, 7]. Another important measure of costs is Levelised Cost of Electricity (LCOE) [8], which is the sum of costs over the entire PV system lifetime over the total electrical energy produced over the lifetime. Module efficiency increases can effectively lower the total system cost as well as the LCOE, by enabling more energy to be produced per unit area. Thus, further solar cell efficiency increases are needed to make PV more cost competitive.

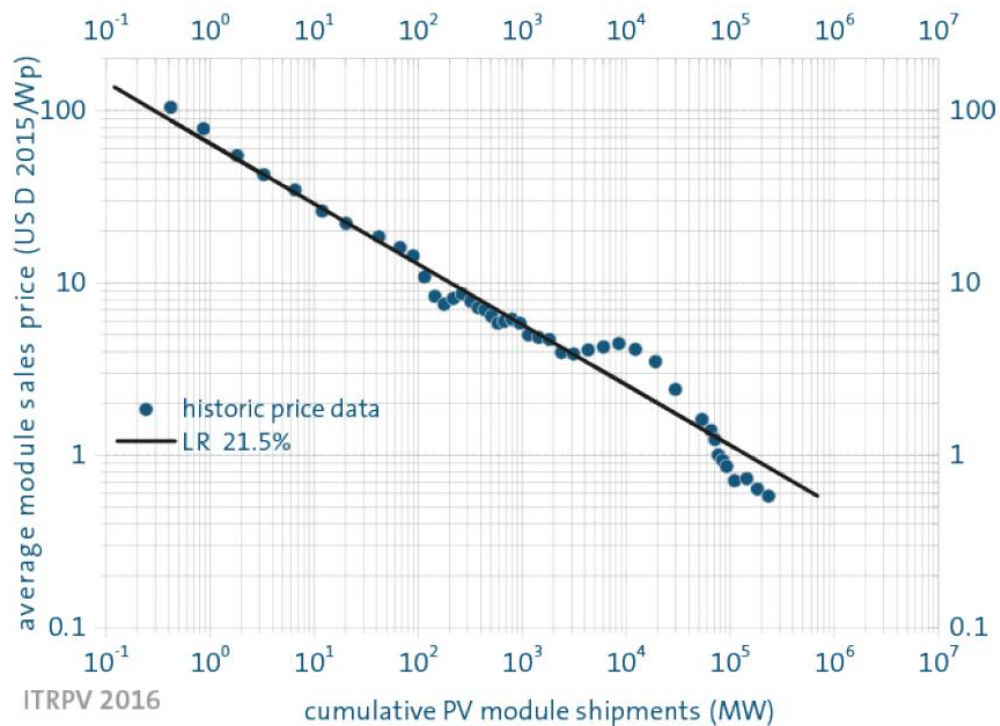


Figure 1.1.1: Learning curve of PV module sales price as a function of cumulative PV module shipments. Figure adopted from ITRPV 2016 [5].

However, the efficiencies of traditional flat-plate solar cells are plateauing [9]. These traditional flat-plate solar cells mostly make use of only one  $p$ - $n$  junction (single-junction solar cells). The most efficient single-junction solar cells, such as the world record 25.6% Si solar cell [10] and the record 28.8% GaAs solar cell [11], are already close to their theoretical efficiency limits of around 30% [12], with very limited room for further improvements. Advanced solar cell concepts are required to surpass the efficiency limits of single-junction solar cells. One approach is the use of multi-junction, or tandem, solar cells. Tandem solar cells make use of more than one  $p$ - $n$  junction, and in this way utilize the solar spectrum more efficiently by reducing losses due to thermalisation and incomplete absorption. In fact, tandem solar cells with around 45% efficiency under concentration have already been demonstrated [9]. However, these cells use expensive substrates and expensive material growth methods, and thus their use is limited to CPV or space applications. One way to reduce the cost of tandem solar cells, while still achieving high efficiency, is to use Si as the substrate and an active sub-cell. Si is a cheap material, and Si PV is a mature technology. Combining Si with thin-film materials into a tandem configuration is, thus, a potentially cost-effective way to realize highly efficient solar cells and modules. Recently, interest in Si based tandem solar cells has been growing, and rapid progress has been made. However, the realistic outdoor performance of flat-plate Si based tandem solar cells has not been investigated. Previous studies on the outdoor performance of other single-junction solar cells, or CPV multi-junction cells, are not directly applicable, for two main reasons: firstly, flat-plate tandem solar cell behaviour is different from that of other types of solar cells. For instance, monolithically integrated tandems tend to be much more sensitive to spectrum

variations than single-junction solar cells due to the current matching requirement of the sub-cells [13]. The likely difference in sub-cell combinations, cell architectures, integration schemes and module designs also distinguish them from traditional CPV multi-junction cells. Secondly, the outdoor operation of flat-plate tandem solar cells differs significantly from that of CPV multi-junction cells. While in CPV applications, solar cells only collect the direct sunlight, flat-plate solar cells also collect indirect and diffuse sunlight. This makes them more suitable for locations with cloudy climates, such as the tropics. Therefore, it is important to develop an energy yield calculation methodology that is more suitable for flat-plate tandem solar cells, and to study their outdoor performance by modelling their behaviour under different operating conditions. This study is also important for determining their economic viability in different areas of applications, as well as for choosing the appropriate tandem configuration that maximizes yield under actual operating conditions.

In this thesis, the term tandem solar cell, by default, refers to flat-plate tandem solar cells unless otherwise stated.

## **1.2. Objectives**

This work aims to study the realistic energy yield potential and outdoor performance of flat-plate Si based tandem solar cells in different climates. More specifically, the energy yield of several III-V-on-Si tandem solar cells (hereafter referred to as III-V/Si tandem) are calculated for the moderate climate of Denver (USA) and the tropical climate of Singapore. Only III-V top cells are considered because of

their well-known material properties and ease of device simulation. However, they may also shed insight on the behaviour of tandem solar cells with top cells made from other materials (such as perovskites).

The main objectives of this thesis were:

- Develop yield calculation methods that are suitable for flat-plate Si based tandem solar cells, in particular by taking into account spectral composition of incoming sunlight and rapid fluctuations of illumination conditions caused by cloud movements.
- Model tandem solar cell behaviour under various conditions using physical device simulation and empirical models.
- Calculate the potential energy yield of various III-V/Si tandems. Compare their outdoor performance, and analyse the losses under outdoor conditions by comparing to their efficiencies under standard testing conditions.

To achieve these goals, outdoor measured solar irradiance and spectrum data with high temporal resolution were obtained and analysed. Detailed device behaviour was modelled by coupled optical-electrical device simulation. Special effort was taken to incorporate spectrum information into yield calculations in a fast and computationally efficient way. In addition, several variations of yield calculation methods were compared and evaluated to reveal the necessary refinements for yield analysis of flat-plate tandem solar cells.



### **1.3. Thesis structure**

The main body of this thesis is organized as follows:

Chapter 2 gives the background of the main subject matter that this thesis is concerned with. It starts by describing the basics of solar cell operation, and the multi-junction concept as a promising strategy to surpass the efficiency limits of single-junction solar cells. Recent developments in Si based tandem solar cells are reviewed to demonstrate the intense research interest and encouraging progress in this area. This will be followed by a detailed introduction to the topic of energy yield analysis, including the key questions of interest and a review of current prevailing practices.

Chapter 3 to Chapter 6 aim to answer some key questions of energy yield studies, namely:

1. What are the outdoor operating conditions experienced by flat-plate tandem solar cells?
2. What is the device performance under these conditions?
3. What are the energy yields and actual outdoor power conversion efficiencies?
4. What are the losses, and how can they be mitigated?

Chapter 3 addresses question 1, and describes the realistic operating conditions that flat-plate tandem solar cell modules may experience during outdoor operations in Singapore and Denver. This chapter also gives some background information on the experimental set-ups for solar irradiance measurement. The instrument specifications and the collected data used for this work are introduced. Basic statistical analysis will be performed on these data.

Chapter 4 focuses on device modelling to address question 2. This chapter outlines the simulation framework and the PC1D physical device models for III-V and Si sub-cells. Tandem solar cell efficiencies under standard testing condition, as well as under various operating conditions as identified in Chapter 3 are obtained.

Chapter 5 looks specifically at the energy yield calculation methodology for flat-plate tandem solar cells. This chapter outlines the fast yield calculation algorithm developed in this thesis, which can incorporate various spectra into yield analysis in an efficient way. Then, a methodology for outdoor loss analysis is proposed. Subsequently, comparisons are made between different yield calculation methods using illumination condition inputs with different levels of detail and accuracy. Through this exercise, it is shown how subtleties in the temporal resolution and accuracy of illumination spectra affect the calculated energy yield in the analysis of outdoor performance of flat-plate tandem solar cells. This sheds light on what the necessary refinements to yield analysis are in order to reliably calculate the yield of flat-plate tandem solar cells.

Chapter 6 addresses questions 3 and 4. This chapter presents energy yield calculation results for several III-V/Si tandems. Both time resolved and annual energy yields are calculated. An analysis is performed to break down the outdoor losses due to different loss mechanisms. As a result, the implications on the potential performance ratios of III-V/Si tandems can be quantified. Then, attempts are made to utilize these results to inform tandem solar cell design and optimization.

Finally, the conclusion chapter (Chapter 7) gives a summary of the main findings and contributions of this work. Some potential future work is also outlined.

## **Chapter 2. Backgrounds of Si based tandem solar cells and energy yield calculations**

This chapter reviews the basics of tandem solar cells and the practice of energy yield analysis. An understanding of solar cell operation characteristics is important in modelling solar cell behaviour under changing operating conditions.

Multi-junction (tandem) solar cells for flat-plate terrestrial applications have additional design dimensions compared to single-junction solar cells. As a result, tandem solar cell response under changing operating condition is more complicated. This necessitates a sophisticated energy yield analysis in order to adequately predict the realistic energy generation by tandem solar cells. A brief introduction of solar cell operation principles and the multi-junction concept will be given in Section 2.1. Recent Si based tandem solar cell developments will be reviewed in Section 2.2. This will be followed in Section 2.3 by a definition of energy yield analysis and a review on its prevailing practices. Specific considerations will be given with regard to flat-plate tandem solar cells.

### **2.1. Basics of solar cells and the multi-junction concept**

#### **2.1.1. Principles of solar cell operation**

Solar cells are devices that directly convert energy from sunlight into electrical energy. In principle, photovoltaic energy conversion can be realized by a variety of

physical processes, with the use of a variety of materials. The essential photovoltaic requirement is the existence of selective contacts, one to the excited states to extract excited electrons, and the other to the ground state to replenish them [14]. In practice, nearly all solar cells nowadays are made of semiconductor devices with a p-n junction. The general p-n junction device structure is shown in Figure 2.1.1 [15]. In these devices, electron-hole pairs are generated by absorbed photons, where electrons are excited from the valence band of the semiconductor to the conduction band. These electron-hole pairs are separated by the bandgap, and need to “survive” (stay separated) for a long enough time without recombining, so that they can move through the material and be collected at the respective contacts, to drive the external load. This is facilitated by the *n*- and *p*-type doped regions, which suppress the concentration of the minority carriers, thus allowing only one type of carrier to reach the contact. The built-in electric field across the p-n junction helps to sweep minority carriers across the p-n junction, into the thin emitter and the thicker base region, respectively.

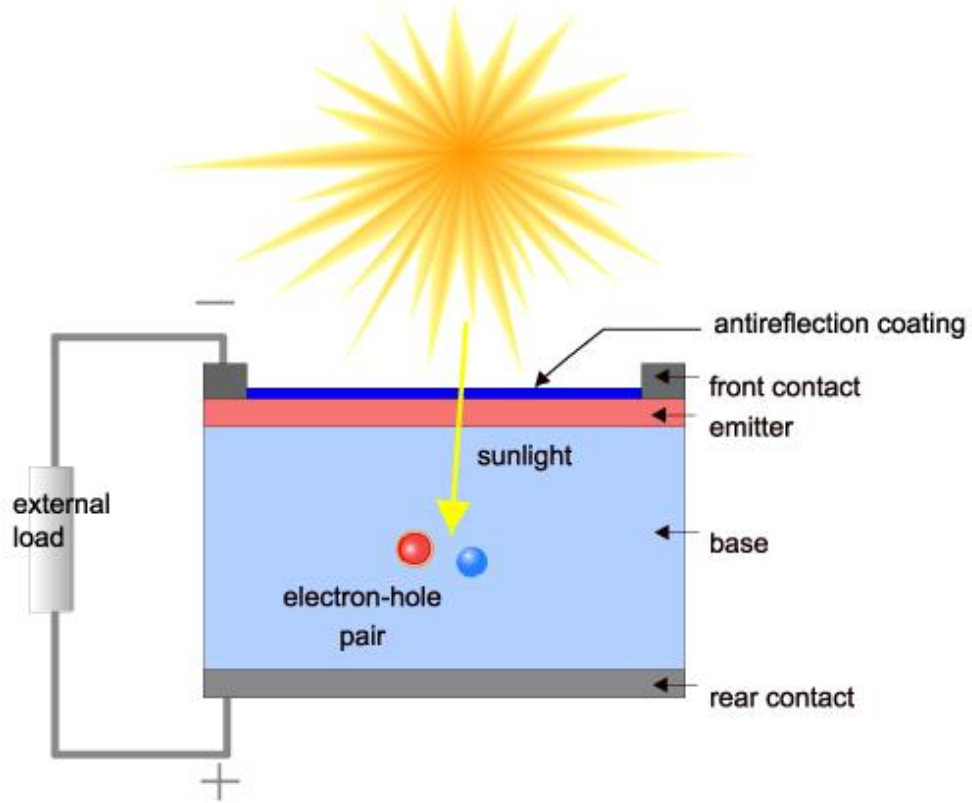


Figure 2.1.1: General structure of a n-p solar cell as illustrated in PV Education [15]. Electron-hole pairs are generated by sunlight. The generated electrons and holes are separately collected by the front contact and the rear contact to drive the external circuit.

The current-voltage (I-V) characteristics of solar cells can be represented by an equivalent circuit model consisting of a current source, one or several diodes, a parasitic series resistance and a parasitic shunt resistance element (Figure 2.1.2) [3]. The equation describing the I-V characteristics for a two-diode representation is given as:

$$I(V) = I_{SC} - I_{o1} \left( e^{\frac{q(V+IR_S)}{kT}} - 1 \right) - I_{o2} \left( e^{\frac{q(V+IR_S)}{2kT}} - 1 \right) - \frac{V+IR_S}{R_{Sh}} \quad (\text{Eq. 1})$$

where  $I$  and  $V$  are the output current and voltage respectively,  $I_{SC}$  is the short-circuit current,  $I_{o1}$  is the dark saturation current due to recombination in the quasi-

neutral regions of the p-n semiconductor (diode 1), and  $I_{o2}$  is the dark saturation current due to recombination in the space-charge region (diode 2). The currents through the two diodes can be regarded as leakages in the semiconductor due to recombination. The lower they are, the better the solar cell efficiency.

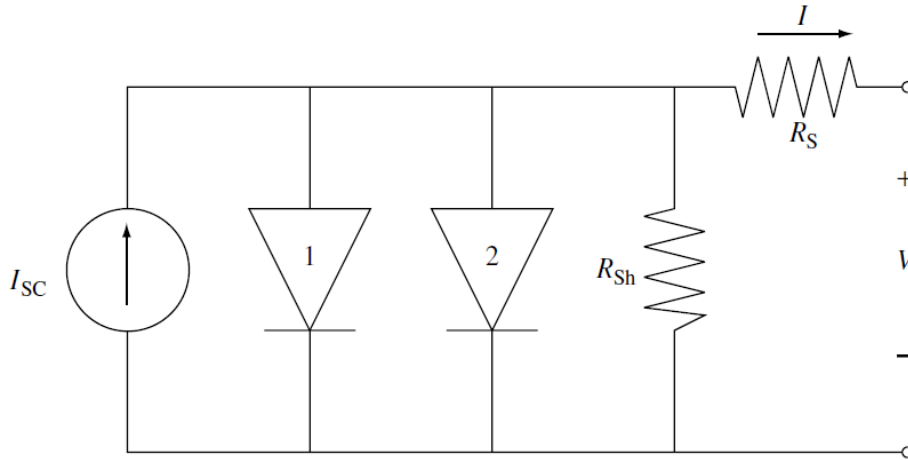


Figure 2.1.2: Equivalent circuit model of a solar cell. After Ref. [3].

The short-circuit current  $I_{sc}$  depends on the light absorption and charge carrier collection of the solar cell, as well as the incoming solar spectrum and its intensity. The solar cell efficiency for 1-Sun applications is commonly rated and compared under the standard testing condition (STC) [16] (see Section 2.3.1 for more details). The spectrum selected for STC is the ASTM<sup>1</sup> G173-03 Reference Spectrum (International standard ISO 9845-1, 1992) [17], commonly referred to as the AM1.5G spectrum (shown in Figure 2.1.3). The absorption and collection characteristics can be described by the

---

<sup>1</sup> An international standards organization, acronym stands for “American Society for Testing and Materials”.

quantum efficiency (QE) of the solar cell, which is the ratio of the number of collected carriers to the number of photons in a certain wavelength (or energy) interval [15]. Alternatively, it can be described by a similar concept called the spectral response (SR), which is the ratio of the generated current to the power incident on the solar cell [15]. As an illustration, the relative spectral responses (obtained by scaling of the measured SRs so that the maximum SR value is unity) of different PV technologies (multicrystalline Si, amorphous Si, CdTe and CIGS) [18, 19] are shown in Figure 2.1.3. Usually, the SR (or QE) is negligible for photon energies below the bandgap of the semiconductor. In addition, the QE is not unity for all photons having energies above the bandgap of the semiconductor. Therefore, the photogenerated current of the solar cell is influenced by the spectral composition of the incoming sunlight.

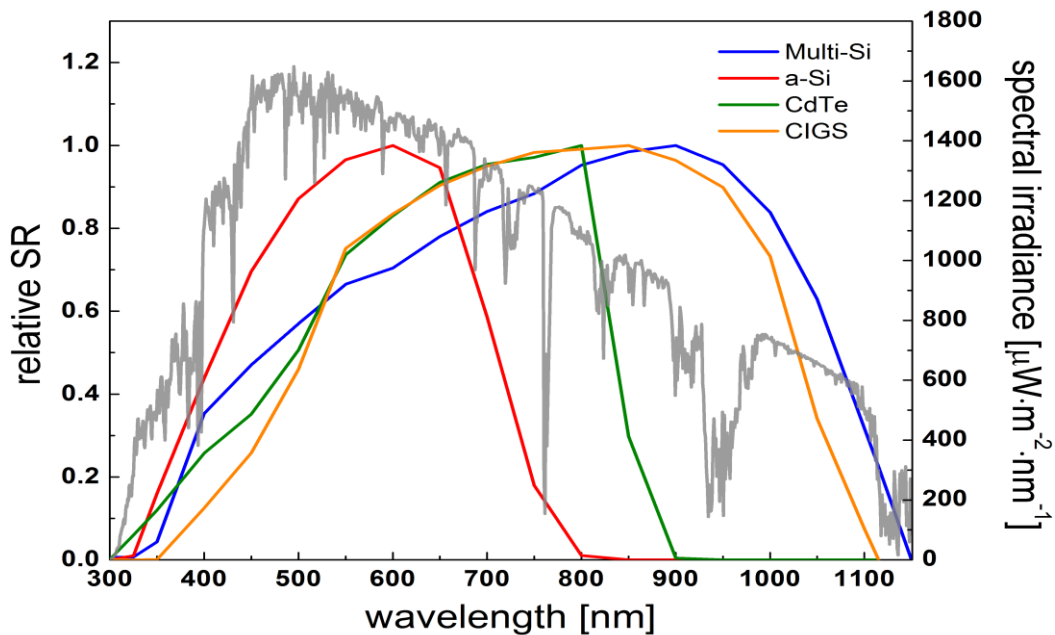


Figure 2.1.3: Relative spectral responses of various PV technologies (multicrystalline Si, amorphous Si, CdTe and CIGS), measured under STC temperature (25°C). The AM1.5G spectrum (grey) is also shown for reference.

The open-circuit voltage of the solar cell depends on the amount of current generated (i.e., the injection level in the bulk of the solar cell), the shunt resistance, the amount of charge carrier recombination (represented by the diode currents), and the operating temperature. Neglecting the effects of the parasitic resistances and diode 2, the open-circuit voltage can be approximated as [3]:

$$V_{OC} \approx \frac{kT}{q} \ln \left( \frac{I_{SC}}{I_{o1}} \right) \quad (\text{Eq. 2})$$

As can be seen, the open-circuit voltage depends roughly logarithmically on  $I_{SC}$ , and thus the incoming light intensity. It is also strongly influenced by the cell temperature. Besides the explicit dependence on  $T$  as shown in Eq. 2, the dark saturation current  $I_{o1}$  (as well as  $I_{o2}$ ) also depends on temperature, due to the dependence of the intrinsic carrier concentration ( $n_i$ ) on temperature. Overall,  $V_{OC}$  drops when the cell temperature increases. As a result, solar cell efficiencies generally drop with increasing temperature. More detailed treatment on the temperature behaviour of solar cells can be found in [20] and [21].

## **2.1.2. Multi-junction solar cells: Going beyond the Shockley-Queisser limit**

### **2.1.2.1. Concept introduction**

Single-junction solar cells, which consist of only one p-n junction, have an efficiency limit that is commonly referred to as the Shockley-Queisser limit. Based on the detailed balance method proposed by Shockley and Queisser [22], the limiting efficiency for single-junction solar cells as a function of their bandgaps, under the



standard AM1.5G spectrum, can be calculated. The maximum efficiency is slightly above 30% [12] and is reached for a bandgap of about 1.3 eV. The peak is quite broad, ensuring that the efficiency limits of c-Si (1.1 eV) and GaAs (1.4 eV) are quite close to the maximum 1-Sun efficiency limit. State-of-the-art Si and GaAs solar cells come quite close to their Shockley-Queisser limits [10, 11], and thus there is very limited room for further efficiency improvements of these PV technologies.

One way of overcoming the Shockley-Queisser limit is to employ the multi-junction (also called tandem) configuration. In this configuration, multiple  $p-n$  junctions made from materials of different bandgaps are arranged so that different portions of the incoming spectrum fall on different sub-cells. This concept is called spectrum splitting. It can take a stacked or spatial configuration, see Figure 2.1.4. With spectrum splitting, each sub-cell absorbs the portion of the solar spectrum which corresponds best to its bandgap. In this way, higher energy photons are absorbed in higher-bandgap materials, thus reducing the thermalisation loss (which is the loss when excited charge carriers lose their excess energy to phonons when they relax back to the respective band edge). Hence, a higher overall voltage can be obtained. Therefore, a multi-junction solar cell is able to make better use of the solar spectrum and achieve a higher efficiency than a single-junction cell.

The sub-cells can be connected in series or stay independent. For instance, a double-junction solar cell can form a 2-terminal (2T) or a 4-terminal (4T) configuration, as illustrated in Figure 2.1.5. More than 4T configurations are also possible for tandem solar cells with three or more junctions, but this case will not be considered in this thesis. For 2-terminal tandem solar cells, the same amount of current flows through all

series connected sub-cells. It is required that the sub-cells are of the same polarity, and that the photogenerated currents of all sub-cells are closely matched. Otherwise, the sub-cell that produces the lowest current will limit the current of the entire device, and the overall efficiency will suffer. This places stringent constraints on the choice of bandgaps and thicknesses of the sub-cells, and at the same time makes the 2T tandem solar cell very sensitive to spectrum changes. In contrast, there is no such constraint in 4-terminal devices, as power is independently drawn from each sub-cell. However, this configuration is hard to realize monolithically. Also, more complicated tandem cell structures, device processing, and electronics are likely needed.

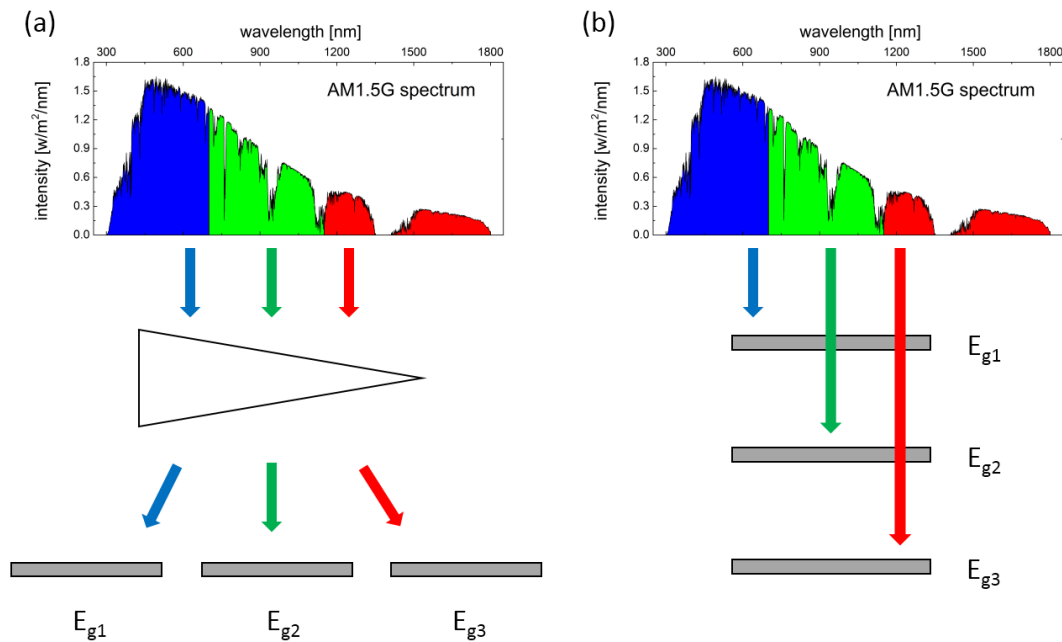


Figure 2.1.4: Illustration of the spectrum splitting concept. Spectrum splitting can be done via (a) a spatial configuration or (b) a stacked configuration. The distribution of photons in the standard solar spectrum is shown at the top. Different portions of light are absorbed in sub-cells with different bandgaps.

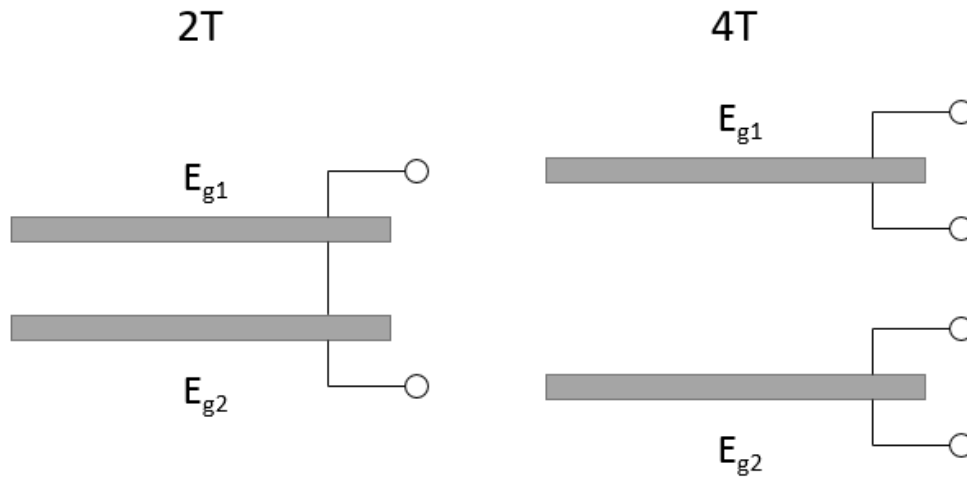


Figure 2.1.5: Illustration of 2-terminal (2T) or 4-terminal (4T) configuration for connecting the sub-cells in a tandem solar cell.

#### 2.1.2.2. Efficiency potentials

Using the detailed balance method, the theoretical efficiency limit of a double-junction tandem solar cell is calculated in this thesis using Mathematica. The calculation makes certain assumptions on the nature and operation of the solar cell. These are:

- Radiative recombination is the only recombination mechanism present in the solar cell;
- One photon generates one electron-hole pair;
- Carrier mobility is assumed to be infinite, therefore no ohmic loss is present and quasi-Fermi level splitting is constant throughout the device.

The method does not consider specific material properties other than the bandgap, and is, thus, very general. It should be noted that numerous studies of tandem solar cell

efficiency limits already exist in the literature [23-26]. What is presented here is a recalculation based on own models and assumptions of optical absorptions.

Three cases were considered here:

a) 4-terminal contact scheme:

The two sub-cells are independently connected, and power is separately drawn from the two sub-cells. No current matching is required, and each sub-cell completely absorbs photons with energy above its bandgap.

b) 2-terminal contact scheme without top cell thinning:

The two sub-cells are series connected, and it is assumed that the top cell has infinite thickness and absorbs all photons with energy above its bandgap. The bottom cell absorbs what is left.

c) 2-terminal contact scheme with top cell thinning:

The two sub-cells are series connected, and the thickness of the top cell is allowed to be reduced so that additional light can pass through to the bottom cell. In this way current matching is always ensured. The amount of optical absorption in each sub-cell is calculated using the transfer matrix method (TMM) [27]. However, it should be noted that sometimes this may result in an unrealistically thin top cell. Another option to achieve current matching is to reduce the top cell area, a concept termed “areal current matching” [28] or “step-cell” [29].

Using the AM1.5G solar spectrum, the efficiency limits as a function of the bandgaps of the top and bottom cells are obtained for the three cases mentioned above.

Figure 2.1.6 shows the contour plot of efficiency limits for 4-terminal contact scheme (case a). Figure 2.1.7 and Figure 2.1.8 show the efficiency limits for 2-terminal contact scheme without and with top cell thinning (cases b and c). The global maximum and local maximum close to the global maximum are indicated by plus signs. For the Si bottom cell bandgap of 1.1 eV, the ideal top cell bandgap is around 1.7 eV, giving an efficiency limit of around 45% for both configurations (2T, 4T). For other bandgap combinations, the maximum efficiency attainable drops quickly when moving away from this optimum, if there is no top cell thinning (Figure 2.1.7). However, the bandgap requirements are greatly relaxed for 4T and 2T with top cell thinning. For example, one promising top cell candidate is GaAs (1.42 eV). Without top cell thinning, the highest efficiency attainable is 23%. However, its 4T efficiency limit hits 42%, which is not much lower than that of the ideal bandgap combination. With top cell thinning, its 2T efficiency limit is also very high (39%), close to that of the 4T configuration. In this case careful design is needed to ensure current matching.

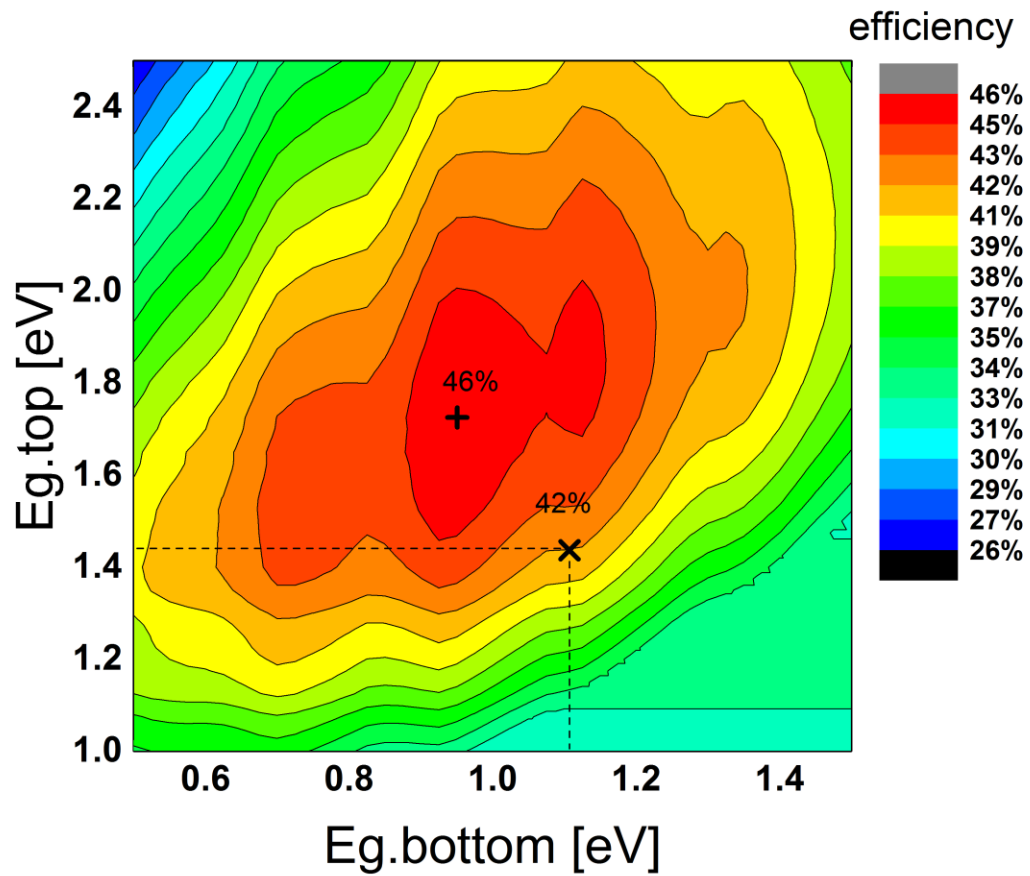


Figure 2.1.6: Theoretical dual-junction efficiency limit for 4-terminal configuration (case a). The global maximum occurs at the bandgap combination of 1.73 eV and 0.95 eV. For the bandgap combination of GaAs (1.42 eV) and Si (1.1 eV), the efficiency limit is 42%.

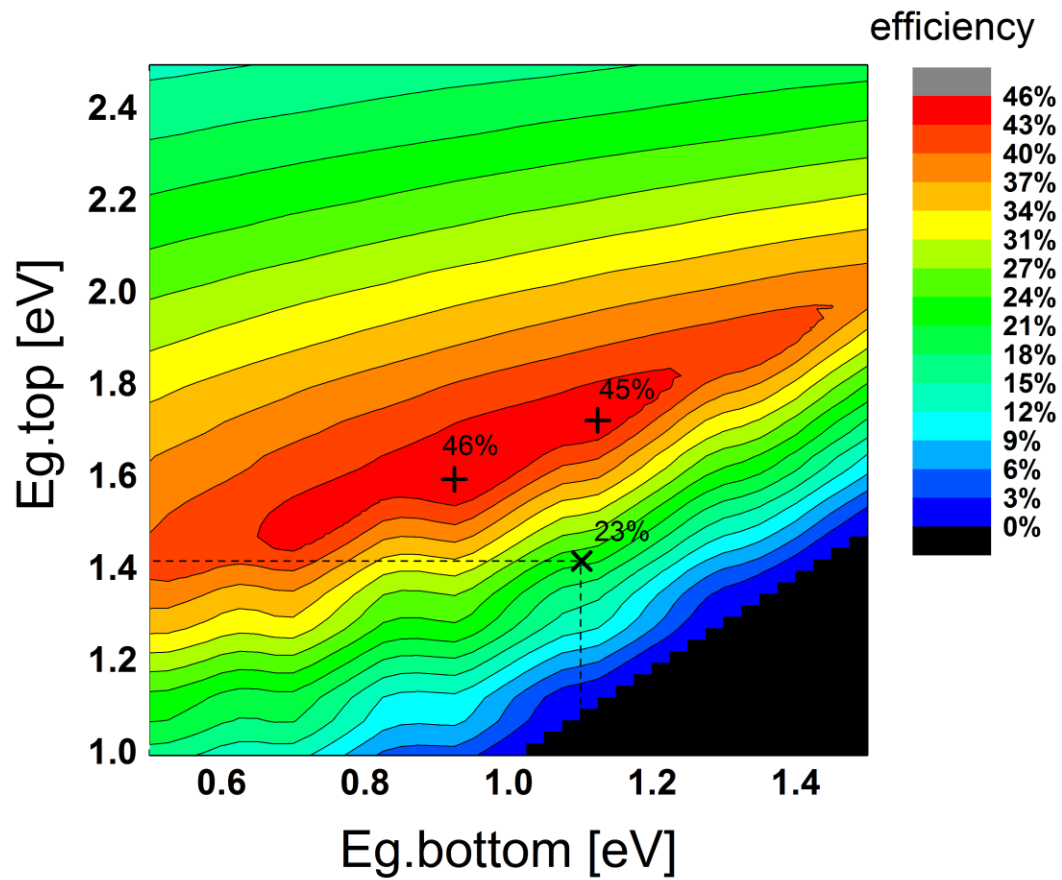


Figure 2.1.7: Theoretical dual-junction efficiency limit for 2-terminal configuration without top cell thinning (case b). The global maximum occurs at the bandgap combination of 1.6 eV and 0.93 eV. Another local maximum with nearly as high efficiency occurs at the combination of 1.73 eV and 1.13 eV. Efficiency drops off rapidly as the top bandgap decreases towards the bottom bandgap. For the bandgap combination of GaAs (1.42 eV) and Si (1.1 eV), the efficiency limit is 23%.

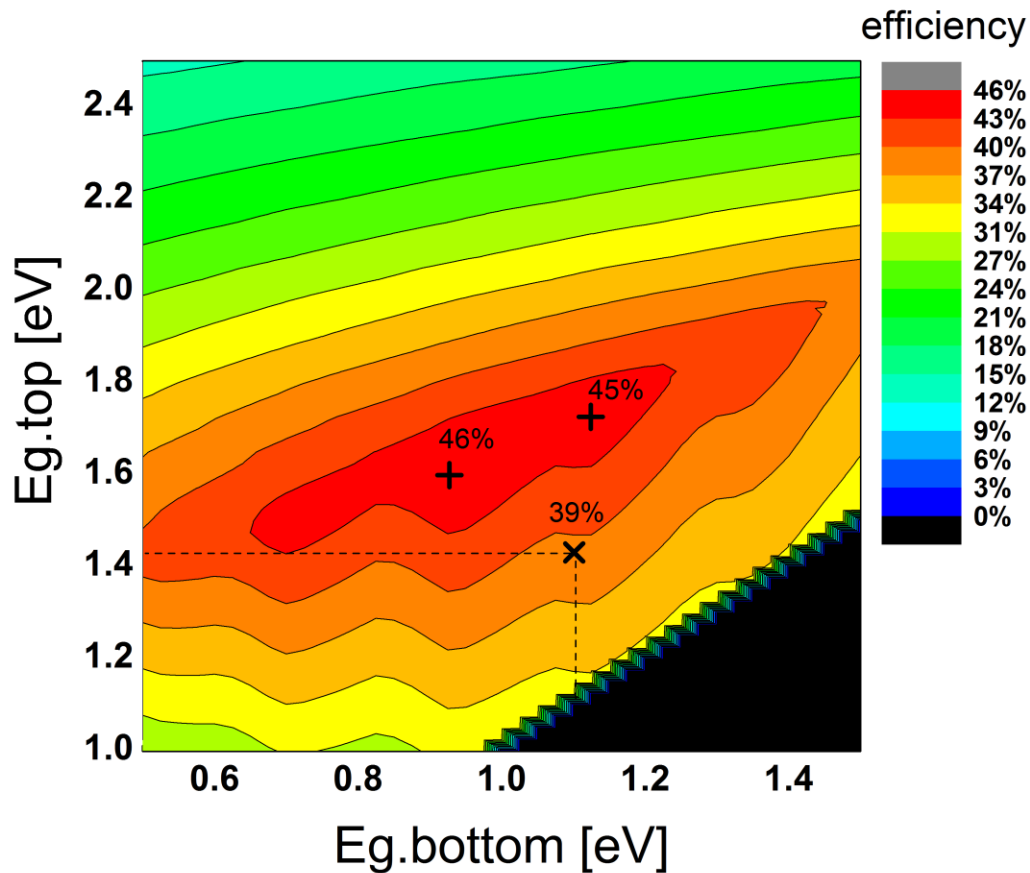


Figure 2.1.8: Theoretical efficiency limit for 2-terminal configuration with top cell thinning to enable current matching (case c). The global maximum occurs at the bandgap combination of 1.6 eV and 0.93 eV. Another local maximum with nearly as high efficiency occurs at the combination of 1.73 eV and 1.13 eV. For the bandgap combination of GaAs (1.42 eV) and Si (1.1 eV), the efficiency limit is 39%.

### 2.1.2.3. Multi-junction solar cells for concentrated PV applications

The best multi-junction solar cells available to date are made from monolithic stacks (i.e. 2T) of III-V materials, or III-V materials on Ge substrates, such as the one shown in Figure 2.1.9. Substantial research efforts have been put into developing the technology to grow and fabricate III-V multi-junction cells in the past few decades [30]. The highest efficiency is now around 45% for III-V material stacks under concentrated illumination [9]. Commercially available III-V multi-junction solar cells are made by



epitaxially growing latticed matched III-V materials on Ge substrates in the GaInP/Ga(In)As/Ge configuration, forming a monolithic tandem stack. The efficiency potential demonstrated by these III-V multi-junction cells is encouraging. The efficiency record is expected to reach 50% in the future [31].

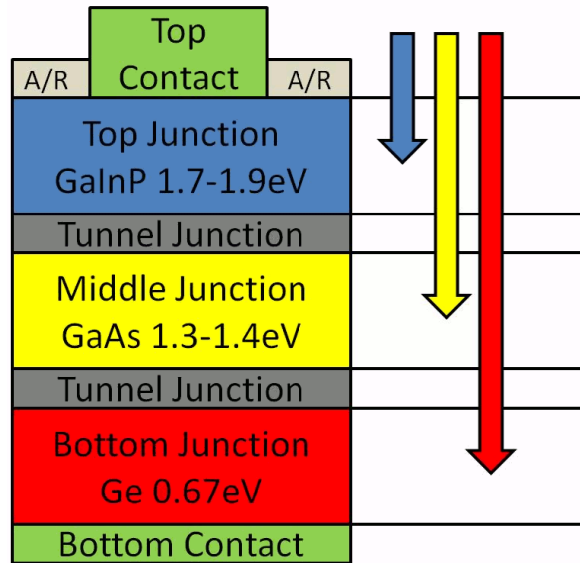


Figure 2.1.9: Schematic of a typical GaInP/Ga(In)As/Ge multi-junction solar cell. The sub-cells are series connected by tunnel junctions. A/R represents antireflection coating. Figure is adopted from [32].

However, one important drawback of III-V multi-junction solar cells is their high cost. This is due to both the employment of expensive Ge or GaAs substrates as well as the low throughput of growing III-V materials [33]. This limits their applications to high-end space or concentrated PV (CPV) systems. Moreover, CPV only uses the direct component of sunlight, and is therefore only suitable for places with mostly clear sky conditions. Tropical regions, such as Singapore, have frequent cloud coverage, fast cloud movements, and a high share of diffuse light, rendering CPV an inappropriate option. Therefore, flat-plate PV systems with cost-effective high-efficiency solar cells are required for such applications.

## 2.2. Overview of Si based tandem solar cells

Monocrystalline or multicrystalline wafer-based Si solar cells are mature and commercially successful technologies that dominate the market today. As balance of system (BOS) and area related costs now take up a large portion of the total system cost, improving the solar cell efficiency has a great impact on reducing the final Levelised Cost of Electricity (LCOE). Therefore, integrating Si with higher-bandgap materials into a high-efficiency tandem solar cell is a topic of great interest to the PV community. Perovskites are presently hot candidates for top cell materials, with efficiencies improving at a breath-taking pace, but still have serious degradation issues [9, 34-36]. Perovskite-on-Si, therefore, represents a low-cost approach with moderate efficiency potential and uncertain reliability. III-V materials as top cells are also very promising. Compared to Ge or GaAs substrates, Si is much cheaper and more widely available. Furthermore, its lighter weight, higher thermal conductivity and stronger mechanical strength render it a better substrate [37]. Depending on the choice of III-V materials for the top cells, its bandgap (1.12 eV) may confer an additional efficiency gain compared to Ge [38]. In addition, common III-V solar cells, such as GaAs or InGaP solar cells, are highly efficient and reliable [11, 39]. Therefore, III-V-on-Si tandem solar cells (III-V/Si tandems) represent a high-efficiency but high-cost approach.

There are several approaches for making III-V/Si tandems:

- Direct epitaxial growth of III-V on Si;
- Wafer bonding of epitaxial lift-off III-V top cell(s) to Si bottom cell;

- Mechanical stacking of top and bottom cells.

Historically, considerable efforts have been made to directly (i.e., hetero-epitaxially) grow III-V solar cells on Si substrates. Respectable III-V/Si efficiencies of around 20% have been demonstrated [40, 41]. However, the technological challenges associated with this approach are huge because of lattice mismatch, differences in thermal expansion coefficients, and difficulties associated with “polar-on-nonpolar” growth. Hence the material quality of epitaxially grown layers is generally not good enough for making high-efficiency tandem solar cells. More recently, growth on graded virtual substrates using the  $\text{Ge}_x\text{Si}_{1-x}$  or GaP alloy systems are being explored [42-46], but no very high efficiency tandem solar cell has been demonstrated yet for this approach.

With the advent of epitaxial lift-off (ELO) and the wafer bonding technology, widely employed to make III-V on Si optoelectronic devices, more options are now available for sub-cell integration. Direct wafer bonding involves bonding of separately made III-V top cells (typically thin films obtained by ELO) on the Si bottom cell after surface activation or passivation. This technique can overcome various constraints encountered in heteroepitaxy. Wafer bonded materials show little degradation of material quality as defects are confined at the bonded interface. Therefore, III-V materials can be grown on GaAs or Ge substrates before transferring them to Si, ensuring high material quality. In 2003, Taguchi *et al.* reported a GaAs/Si tandem cell fabricated this way, with overall efficiency of 19.4% [47]. The transferred GaAs top cell had good quality, with no serious degradation during the transplantation process, and a bulk lifetime comparable to homoepitaxial GaAs. Derendorf *et al.* produced a

multi-junction cell by bonding a GaInP/GaAs dual-junction cell and a Si bottom cell, and achieved an efficiency of 23.6% under concentration [48]. The surface activated direct wafer bonding process they employed resulted in a 5 nm thin amorphous layer, which was found to introduce no significant series resistance across the interface. With optimization, the bonded multi-junction cell has achieved even higher efficiency more recently, reaching nearly 30% without concentration [49]. However, there are also significant challenges associated with this approach, as it imposes stringent requirements on the surface smoothness and as it is difficult to achieve large-area high-throughput fabrication.

Another approach, mechanical stacking, is conceptually much simpler. It involves attaching separately made III-V and Si sub-cells together by adhesives. It allows the use of the best single-junction solar cells as sub-cells without having to overcome the epitaxial growth challenges associated with monolithic tandem cells. In addition, it allows easy realization of the 4-terminal configuration and offers more freedom in circuit wiring at the module level [50]. However, an effective way is required to integrate sub-cells together that minimizes additional optical and electrical losses. If significant loss is introduced in device integration, there may be a danger of offsetting benefits gained from the additional junction. The need for a free-standing top cell with a transparent back contact and more fabrication steps can also be a drawback. Other approaches of tandem integration are also proposed in the literature, such as III-V nanowires on Si [51-55]. These novel concepts will not be reviewed in this thesis.

In recent years, there has been rapid progress in Si based tandem solar cell efficiency. The progression of tandem efficiencies made with different top cells, or

fabricated via different approaches, are summarized in Figure 2.2.1. The most notable progress comes from wafer bonding and mechanical stacking of III-V/Si tandem solar cells. Around 30% efficiencies were achieved by a wafer bonded InGaP/GaAs//Si [49], and a mechanically stacked InGaP/Si solar cell [56]. This highlights the intense research interest as well as the promising efficiency potential of Si based tandem solar cells. In this thesis, only III-V/Si tandems will be modelled. The configurations investigated include both dual-junction and triple-junction cells, with 2-terminal or 4-terminal connection.

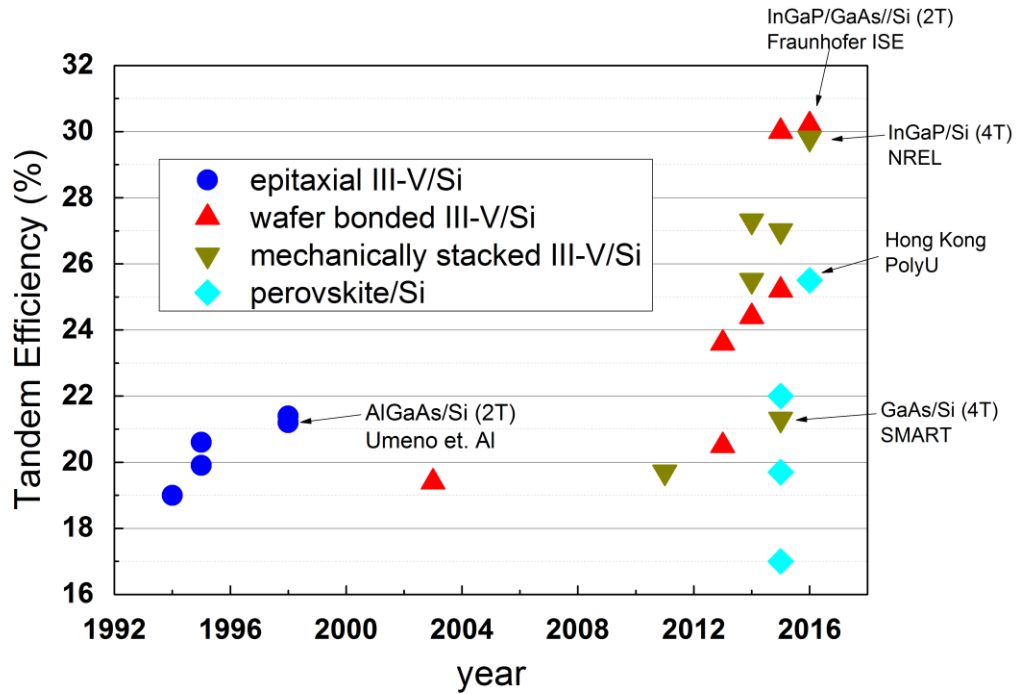


Figure 2.2.1: Some published efficiency values of Si based tandem solar cells of different categories. Some values are reported under different test conditions (such as AM0 spectrum, or concentrated illumination), therefore should only be taken as a rough indication of efficiency levels. In 2016, tandem solar cells reaching 30% 1-Sun (AM1.5G) efficiency were fabricated in the laboratory (Fraunhofer ISE and NREL).

## 2.3. Energy yield analysis

### 2.3.1. Standard testing condition (STC) and its limitations

Solar cells and modules are commonly rated under the Standard Testing Condition (STC) [16]. This set of conditions is:

- Irradiance level of  $1000 \text{ W/m}^2$  (often called 1 Sun);
- AM1.5G spectrum (or AM1.5D for concentration cells), as defined in ASTM G173-03 [17];
- Cell temperature of  $25 \text{ }^\circ\text{C}$  (room temperature).

The use of a standardised testing condition facilitates comparisons among different solar cells and modules. It is an important standardisation for both laboratory research and industrial manufacturing. The efficiency values under this set of conditions, together with the open-circuit voltage, short-circuit current, and maximum power, are often stated in the manufacturer's data sheets for the produced modules. However, the use of STC efficiency in predicting actual device energy yield under deployment has been frequently questioned, as the actual long term energy conversion efficiencies of solar cells were often found to be significantly lower than the STC efficiency [57, 58]. This is because realistic outdoor operating conditions deviate to a substantial degree from STC.

One way to account for this change of efficiency under actual operation is the introduction of the harvesting efficiency ( $\eta_{har}$ ) and the performance ratio (PR). The harvesting efficiency is defined as the ratio between the total electric energy generated and the total solar energy received during the same period [59]. It indicates the true

power conversion efficiency of the PV generator. Performance ratio, as defined in the IEC standard 61724 (1998) [60], is the ratio between the actual energy yield and the expected energy yield of the PV generator based on its rated efficiency under STC. PR is usually used to describe the realistic performance of a PV system relative to its rated nameplate performance. PRs of commercial PV systems commonly range from 70% to 90% [58]. In this thesis, the scope of PR is broadened to describe solar cells or modules as well. The mechanisms that cause outdoor operation losses are illustrated in Figure 2.3.1. In particular, the losses due to spectrum, low irradiation, and temperature are mainly associated with responses of solar cells, and will be closely examined in this thesis. The losses from inverters, cabling and other system components are sometimes called system losses. This part of PR loss is not within the scope of this thesis.

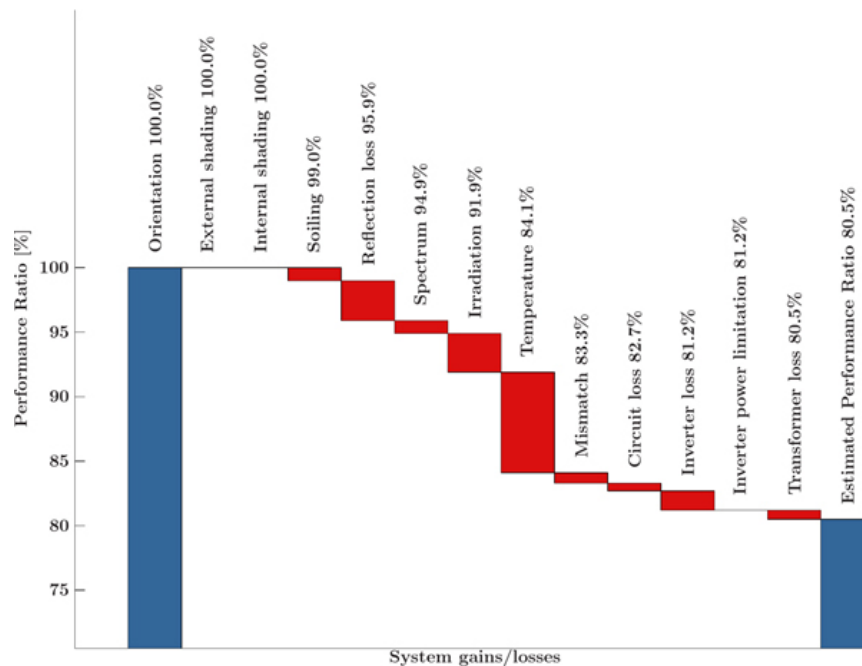


Figure 2.3.1: Illustration of the breakdown of performance ratio related losses for a typical commercial Si-based PV system in Singapore. The typical outdoor losses and their usual contributions are shown. Figure is adopted from the National Solar Repository of Singapore [61].

### 2.3.2. Key questions of energy yield analysis

Energy yield analysis, as defined in this thesis, is the calculation of electric energy delivered by a PV device or system, and the determination of the relative performance when compared with the STC efficiency by quantifying various outdoor losses. The key questions to address include the following:

- What is the expected solar irradiation?

The amount of solar irradiation available is a key piece of information for any solar project. Its prediction based on historical data and site considerations form one major component of the energy yield calculation.

- What are the outdoor operating conditions?

The operating conditions for solar cells need to be adequately described in order to determine the solar cell output. There are several major aspects. One important aspect is the illumination conditions, which refers to the intensity and spectral composition of the incoming light. Another important one is the operating temperature. The impact of these conditions on the power output of tandem solar cells will be studied in this thesis. Other relevant conditions such as shading will not be covered.

- What is the device / system performance under these conditions?

The power output of solar cells or systems varies for different conditions. It is therefore necessary to measure or model their response under relevant operating conditions.

- What are the time scales concerned (short term or long term)?



The energy yield of a solar cell can be calculated for a certain time period - for example a day, a month, or a year. Long-term yield, such as the annual yield, is usually considered when overall energy generation or Levelised Cost of Electricity (LCOE) calculations are concerned. However, short-term energy yield is also important, for example for estimating the required solar cell size and electricity storage capacity for certain applications, in forecasting and assessing the impact on power grids, as well as in monitoring system output and fault detection. Therefore, how to calculate the energy yield for different time periods with a firm accuracy is a relevant question.

- What are the energy yields and harvesting efficiencies?

With adequate data and modelling, the final harvesting efficiency, and the amount of energy yield for a certain time period can be obtained.

- What are the losses, and how to mitigate them?

The contribution of different outdoor loss mechanisms to the performance drop can be analysed and quantified. This is helpful in advising design and optimization in order to minimize overall losses.

- What is the implication on the financing of projects and the economics?

The results from energy yield calculations are important inputs to the cost calculation for a particular solar cell technology or a solar project.

This thesis is organized in such a way to address these questions in the context of flat-plate Si based tandem solar cells targeted for non-concentration applications. However, the prediction of solar irradiation and the implications on the costs of electricity will not be covered.

Two purposes which energy yield analysis serves should be distinguished. They put different requirements on the way the yield analysis is carried out. One purpose is PV system design, the other one is cell/module development, optimization, as well as comparison. The amount of predicted energy yield and cost consideration is the key focus for the first area, whereas the latter is more concerned with minimizing losses and customization. In other words, the former looks more at the absolute value of electricity delivery of a system, while the latter looks more at the relative performance. As a consequence, the methodologies used for energy yield analysis for these two different purposes can be vastly different. Sophisticated modelling, be it on solar irradiation, operating conditions, or PV generator output, is generally not critical for the system designers, as statistical uncertainties in solar resource prediction are usually much larger than model inaccuracies. However, for optimizing solar cell designs and comparing different cell architectures, detailed device simulation is useful in distinguishing subtle performance differences. Second-order effects and non-linearity in device response need to be adequately captured. More details about practices within these two regimes will be reviewed in the following section (Section 2.3.3).

### **2.3.3. Prevailing practices of energy yield analysis**

Energy yield analysis is, traditionally, only thought of as a broad collection of yield prediction exercises for PV system designers. The objectives for applying this calculation include for example sizing of stand-alone systems, prediction of long-term energy generation, optimisation of tilt angles, and assessing the impact of shadowing. For nearly all practical purposes in yield prediction, the amount of solar irradiation

(energy density in kWh/m<sup>2</sup>) is of primary concern. Secondary effects, such as effects from solar spectrum, low irradiance, wind speed, incidence angles, and sometimes even temperatures, are deemed of minor importance, and thus are often neglected in real engineering practices [57]. This is because the uncertainty in forecasting the amount of solar irradiation is much larger, and, thus, sets a limit to the accuracy attainable, irrespective of model sophistication.

The first important task, which is intensely researched, is to find out how much solar irradiation is available. To determine the amount of expected solar irradiation on the horizontal surface of a particular site over a period of time, the average monthly mean values of daily irradiation, obtained from historical data, is usually used. Alternatively, the Typical Meteorological Year (TMY) [15], which is a hypothetical reference year with the collection of average months (picked from different years) throughout the whole measurement period for which data are available, can be taken as the representative year. Common TMY databases, such as that curated by the National Renewable Energy Laboratory (NREL) from the United States [62], contains hourly solar irradiance data (power density in W/m<sup>2</sup>) for various locations. In contrast, long-time series of historical data are less available, and are seldom used for yield calculations. Furthermore, it is observed that calculations done with different solar irradiation data sources, be it historical time series, TMY, or just 12 average monthly mean values, produce very similar results [57].

Given the average monthly mean values of daily global irradiation on the horizontal surface, which is the most widely available form of solar radiation data, the hourly irradiance throughout the course of a day can be estimated. It is then

decomposed into direct, diffuse, and albedo components using decomposition models, such as the Hay and Davies model [63] or Perez model [64, 65]. Subsequently, transposition models [66, 67] are used to transpose these irradiance components into corresponding components on inclined module surfaces. Available solar energy content over a certain period of interest can then be obtained by integration.

A large number of correlation models to predict solar irradiation and its components have been proposed in the literature [68]. Some of them use sophisticated equations and more rigour in statistical fitting, while others are location specific. They were derived from different data sources, and may use different predictors. The results obtained with different models can sometimes be quite different from each other.

Another important task of yield calculation is to determine the PV device response under diverse operating conditions. In most cases, the device behaviour under changing conditions needs to be modelled, instead of extensively measured due to operational and economic reasons. Modelling and analysis of system components other than solar cells, such as inverters and batteries, may be important as well. Usually, the modelling of PV module and system behaviour is kept simple, with judicious simplifications, assumptions, and empirically fitted parameters [57]. More detailed system simulation methodologies are available, with second-order corrections of device behaviour, more accurate treatment of non-prevalent outdoor conditions, and consideration of more factors [69]. However, there is contention over how useful the marginal improvements are, and whether that justifies the increase in complexity [57]. Detailed physical device simulation is never invoked in normal system designing processes. This is again because the uncertainties associated with the inherent random

nature of future solar irradiation are thought to render the small inaccuracies of crude models insignificant.

Nonetheless, the importance of a more accurate energy yield analysis is being increasingly appreciated, both in academia and in the industry [70-72]. This is especially the case in designing solar cells and modules. There are several reasons behind this.

Firstly, a large number of solar cell technologies and architectures have been developed. Solar cell behaviours can vary significantly. For instance, high-bandgap thin-film solar cells (such as amorphous Si solar cells) and tandem solar cells are sensitive to the solar spectrum [73, 74], while crystalline Si wafer based solar cells are generally not [75]. For another example, heterojunction (HIT) [10, 76] Si solar cells exhibit different spectral response from traditional diffused-junction Si solar cells, and thus tend to result in different performance ratios. A physical device simulation can help to capture these differences under realistic operating conditions. This is particularly useful for cells or modules under development, when no established simple empirical models exist to describe their properties. This is also important for designing solar cells and modules towards lower LCOE (instead of cost per watt peak,  $\$/W_p$ ), as well as to facilitate comparison across different technologies as deployment options. This objective, as opposed to yield analysis for solar projects, has received little attention in the past, and is relatively unestablished. No systematic way to perform yield analysis to assess the outdoor potential for different solar technologies has been proposed.

Secondly, the installed PV capacity is growing at a fast pace, and PV systems are deployed in more locations, with a wide span of climatic conditions. The scale and diversity of PV deployment makes accurate and location specific yield assessments more important than before, due to a larger impact on the economics and financial risk assessment [70]. The inclusion of second-order effects, such as from changing solar spectrum and from device non-linearity, can lead to a better description of solar cell outputs, and thus reduce systematic errors in energy yield predictions for PV systems. A better understanding of second-order effects is also important in monitoring real time PV system outputs. For instance, spectral effects on energy generation may be small for most Si solar cells on a yearly basis, but may be sometimes large on an hourly basis [57], and thus constitute a major reason behind short-term irregularities in PV outputs.

Thirdly, the quest for more sophisticated yield calculation is also fuelled by a more powerful computation infrastructure and increased availability of measurement data. Therefore, more elaborate models can be used to better model solar irradiation, operating conditions, as well as device performance, with only a small marginal increase in costs.

In particular, spectral effects have been extensively studied in the literature. Numerous studies have investigated the spectral effects on CPV multi-junction cells and systems [13, 59, 74, 77-80]. A few similar studies were also conducted for some non-concentrating PV cells and modules [70, 75, 81-83]. These studies usually used simulated spectra from the SMARTS clear sky radiative transfer model [84] or from similar programs. Depending on the level of sophistication, these energy yield models simply invoke historical average values for atmospheric parameters (with the exception

of air mass), or use time varying inputs with resolution of just one value per month. The use of measured atmospheric parameters as inputs for spectrum simulation programmes is largely constraint by their limited availability. In addition, as SMARTS is a clear sky model, the effect of clouds are not taken into account. Therefore, the simulated spectra are expected to have some degree of deviation from real spectra.

#### **2.3.4. Specific considerations for flat-plate tandem solar cells**

Si based tandem solar cells, due to cost reasons, may be used in flat-plate non-concentrated applications. Their operation will differ significantly from traditional III-V multi-junction solar cells used in CPV. Also, they will behave differently from single-junction solar cells. Therefore, specific considerations different from previous studies need to be taken for Si based tandem solar cells.

Few previous studies for tandem solar cells looked at the effect of the global spectrum (most looked at the direct normal spectrum). In addition, few looked at the combined effect of changing spectrum, fluctuating irradiance levels, and fluctuating operating temperature. This is because multi-junction cells typically operate in locations with abundant solar irradiance and mostly clear, smooth weather conditions as CPV applications, and the conventional ways of estimating spectral effects are sufficient. However, this may not be the case for flat-plate tandem solar cells deployed in cloudy locations such as tropical Singapore. In these locations, both the spectrum and intensity are altered frequently by clouds. Spectrum changes impact tandem solar cells, especially 2-terminal devices due to current mismatch issues. Other than the

spectral effect, the low-irradiance loss for tandem solar cells might also be a concern, since sub-cells divide incoming irradiance and each thus operates at lower injection. Therefore, it is of interest to assess how a fluctuating global irradiance affects their power generation. The characteristics of operating temperatures of flat-plate tandem solar cells are also different from CPV cells. Their thermal features will likely be closer to flat-plate single-junction solar cells and modules, but they have different efficiencies and thermal coefficients. This will also make a difference in the energy yield. In this thesis, energy yield calculation taking these specific considerations into account will be developed and applied to flat-plate Si based tandem solar cells.

## **2.4. Chapter summary**

In this chapter, the basic operation principles of solar cells were introduced. It was seen that solar cell outputs vary with changing operating condition, in particular light intensity, spectrum, and temperature. The concept of multi-junction (or tandem) solar cells, which can surpass the efficiency limit of single-junction solar cells, was explained. It was found that tandem solar cells using Si as the bottom cell have very high 1-Sun efficiency potential of 42% for 4-terminal configuration and 39% for 2-terminal configuration. Therefore, Si based tandem solar cells have attracted intense research interest, and rapid progress has been made recently. The energy yield analysis of flat-plate Si based tandem solar cells is a relevant topic, but has not yet been adequately explored. In the latter half of this chapter, the motivation and objectives of energy yield analysis in general was established. It was deemed important in both PV system design and solar cell or module development, but detailed methodologies might



differ for different purposes. The prevailing practices of energy yield analysis were reviewed, and requirements specific to flat-plate tandem solar cells that were lacking in previous practices were identified. In later chapters, energy yield calculation methods suitable for flat-plate Si based tandem solar cells will be developed to assess their outdoor performance.

## **Chapter 3. Realistic outdoor operating conditions**

This chapter describes the realistic operating conditions that flat-plate tandem solar cell modules may experience in outdoor applications. The major variables to represent these conditions include irradiance level, spectrum, and ambient temperature. These variables are used as inputs for energy yield studies. The first section (3.1) describes the experimental setup for measurements of the irradiance and spectral data in Singapore and Denver, which are the two locations selected in this thesis for the energy yield studies. In Section 3.2, a detailed description and analysis of the measured outdoor conditions for the two locations is given. The analysis sheds insights on the relevant range of illumination conditions and possible solar cell operating temperatures. It is also useful in determining the most important conditions for which a solar cell, designed for a specific location, should be optimized. Finally, Section 3.3 briefly describes the year-to-year variability of these conditions.

### **3.1. Measurements of outdoor conditions**

The data used to describe outdoor operating conditions of PV systems include solar irradiance level, spectrum, ambient temperature, relative humidity, wind speed, module temperature, and various other meteorological parameters. Among these variables, the irradiance level, spectrum, and ambient temperature are used as inputs for energy yield studies in this thesis. This section introduces how solar irradiance data are collected and monitored in the Solar Energy Research Institute of Singapore (SERIS) [85]. The data collected are used as input for energy yield calculations for flat-

plate tandem solar cells in Singapore. In addition, a similar set of data from Denver are also used. These data were collected by the National Renewable Energy Laboratory (NREL) in the US. This data set is also introduced in this section.

### **3.1.1. Solar irradiance level measurements**

The solar irradiance level, i.e. the sunlight intensity, is commonly measured by a (thermopile) pyranometer or a Si reference cell in PV applications [86]. Pyranometers use thermocouples to detect temperature differences caused by the incident solar irradiation [87]. The temperature differences result in a voltage signal, via the Seebeck effect, and the signal is detected by an electronic circuit. One advantage of this instrument is that it has virtually no spectral selectivity, as the black carbon coating of the thermocouple absorbs radiation over a very wide range of wavelengths. Also, the directional errors are usually low. The response time is usually in the range of a few seconds to tens of seconds [88]. A Si reference cell, on the other hand, makes use of the photocurrent output of the solar cell, and has a very fast response time. However, Si solar cells have a wavelength-dependent spectral response and an incomplete coverage of the entire solar wavelength range, only up to the bandgap of Si, which is around 1120 nm. Therefore, errors will result when the spectral composition of the incoming sunlight shifts from the standard spectrum used to calibrate the reference cell. In addition, the directional errors are considerably larger than for pyranometers, due to the absence of dome shaped entrance optics. However, due to convenience and much lower cost, Si reference cells are commonly installed along with the PV modules to measure the in-plane solar irradiance level.

In SERIS, the PV Monitoring Lab (Figure 3.1.1) routinely collects and monitors a plethora of meteorological parameters, such as instantaneous solar irradiance level, spectrum, wind speed, ambient temperature and many others, with very high temporal resolution (one data point per minute). The measurement stations are geographically spread across the island of Singapore. Performances of several PV systems are also measured with time stamps that are highly synchronized to meteorological measurements. In this thesis, the more accurate measurement of solar irradiance level, using the pyranometer (model SPN1, Delta-T Devices [89]) installed in one of SERIS' meteorological stations, is used. The specifications of the pyranometer are listed in Table 3.1.1. The spectral response range is from 400 to 2700 nm, which corresponds to an intensity of  $946.5 \text{ W/m}^2$  in the standard AM1.5G spectrum.



Figure 3.1.1: The PV Monitoring Lab in SERIS. A variety of meteorological parameters such as instantaneous solar irradiance level, spectrum, wind speed, ambient temperature, and real-time performance of PV systems are measured and monitored.

Table 3.1.1: Specifications of the model SPN1 pyranometer used to collect solar irradiance level data in Singapore. The pyranometer is mounted horizontally with zero tilt.

Spectral response	400 - 2700 nm
Cosine error	$\pm 2\%$ of incoming radiation over 0-90° zenith angle
Zero offset	$< 3 \text{ W/m}^2$
Overall accuracy - Total (Global) and Diffuse radiation	$\pm 5\%$ Daily integrals $\pm 5\% \pm 10 \text{ W/m}^2$ Hourly averages $\pm 8\% \pm 10 \text{ W/m}^2$ Individual readings
Non-linearity	$< 1\%$

The solar irradiance data for Denver were obtained from NREL. Measurements are carried out by the Solar Radiation Research Laboratory, Baseline Measurement System [90], located at 39.74° North and 105.18° West, with an elevation of 1829 m above sea level. The pyranometer used is an Eppley Laboratory Inc. model PSP instrument, tilted 40° and facing south. The specifications of this pyranometer are listed in Table 3.1.2. The spectral response range is from 285 to 2800 nm, which corresponds to an intensity of 992.6 W/m<sup>2</sup> in the standard AM1.5G spectrum.

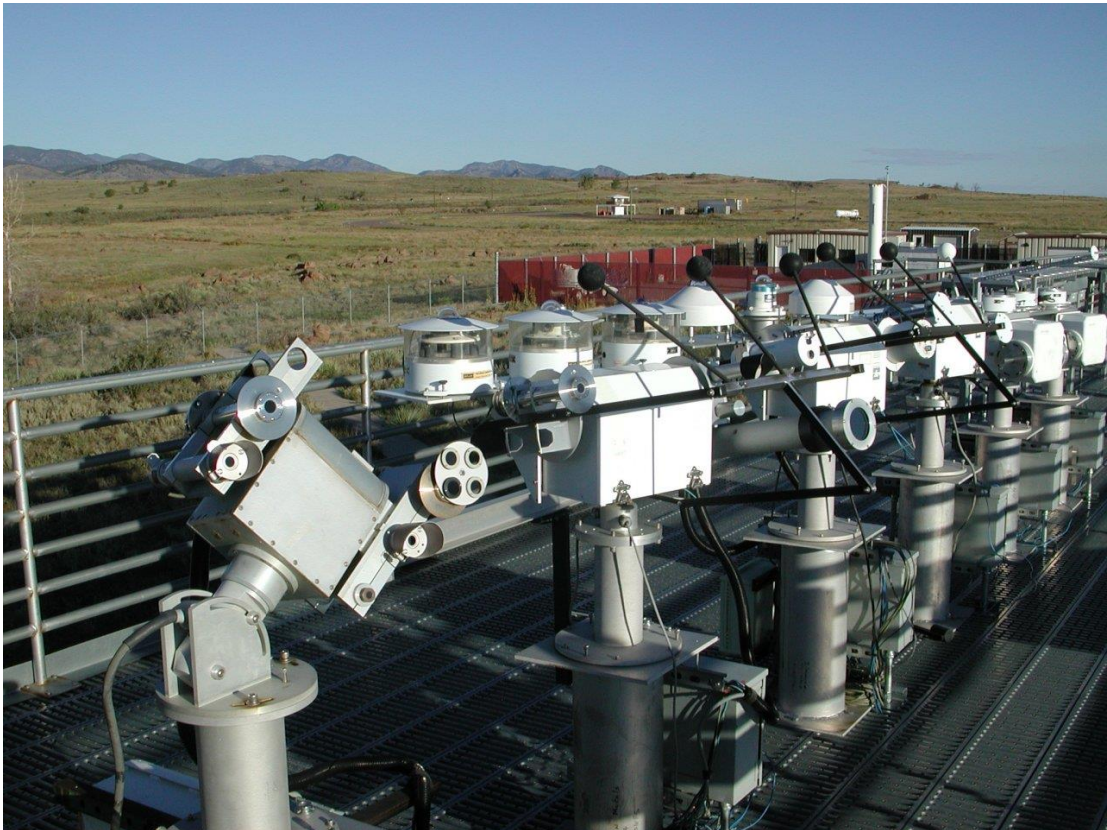


Figure 3.1.2: The Solar Radiation Research Laboratory, Baseline Measurement System is a facility supporting NREL's resource assessment and forecasting research. The Baseline Measurement System has a large collection of radiometers that record surface meteorological conditions.

Table 3.1.2: Specifications of the model PSP pyranometer used to collect solar irradiance level data in Denver. The pyranometer is mounted with a tilt of 40° and is facing south.

Spectral response	285 - 2800 nm
Cosine error	±1% (0-70°), ±3% (70-80°)
Zero offset	-5 to 2 W/m <sup>2</sup>
Overall accuracy	absolute accuracy of calibration is ±3-4%
Non-linearity	±0.5% from 0 to 2800 W/m <sup>2</sup>

### 3.1.2. Solar spectrum measurements

The spectral composition of the incoming sunlight is most accurately measured using a spectroradiometer [91]. A spectroradiometer consists of entrance optics, a monochromator that usually uses diffraction gratings to disperse incoming light, and a detector. It measures the wavelength resolved spectral irradiance over a certain wavelength range. The spectral data used in this thesis were also obtained from SERIS and NREL. The spectroradiometer used to collect the spectral data for both Singapore and Denver is a model EKO MS-700 [92], installed at the same location as the pyranometer. The specifications are listed in Table 3.1.3. The wavelength range is from around 350 nm to around 1060 nm, which corresponds to an intensity of 773.5 W/m<sup>2</sup> in the standard AM1.5G spectrum. This wavelength range covers most of the relevant range usable by the tandem solar cells considered in this thesis.

Table 3.1.3: Specifications of the model EKO MS-700 spectroradiometer used to collect solar spectral data in Singapore and Denver. The spectroradiometer is mounted horizontally in Singapore and tilted 40° facing south in Denver.

Wavelength range	345.4 - 1066.5 nm
Cosine error	< 7%
Exposure time	10 ms - 5 s
Temperature dependency (-20°C to 50°C)	< ±1%
Weight	4 kg

### 3.1.2.1. *Intensity issues with spectrum measurement*

It should be noted that spectroradiometers were found to give lower readings for the integrated intensity than what was measured by pyranometers for both datasets from Singapore and Denver. In the AM1.5G spectrum, the wavelength range of 350 nm to 1060 nm provides around 80% of the total power in the spectrum (1000 W/m<sup>2</sup>). After accounting for this factor, the integrated spectral irradiance (ISI) from spectral data in both Singapore and Denver was still about 10% lower than the measured insolation. Similar problems have been reported by other groups [93-95], suggesting multiple possible sources of error and uncertainty in spectroradiometer measurements. In this thesis, the discrepancy is rectified by scaling the spectrum data to fit the measured irradiance level from the pyranometer. This preserves the spectral composition and only alters the intensity. This scaling only introduces marginal errors in the absolute intensity, and will not affect the analysis of tandem solar cell losses that are related to spectral variations.



## **3.2. Analysis of outdoor operation conditions**

Outdoor illumination conditions and operating temperatures may deviate significantly from conditions defined under standard testing condition (STC). This section provides an overview of the measured datasets of solar irradiance (Section 3.2.1) and spectrum (Section 3.2.2). Their features and characteristics are described. This is useful for illustrating the deviations of outdoor illumination conditions from STC. A correlation is found from the datasets between the spectral composition and the irradiance level. This will be analysed and presented in Section 3.2.2. In Section 3.2.3, a useful way to sort the illumination conditions based on intensity levels and spectral compositions is proposed. The occurrence frequency and the energy content distribution of different illumination conditions for Singapore and Denver are presented. This is followed by a discussion of outdoor operating temperatures based on the available data of measured ambient temperatures in Section 3.2.4.

### **3.2.1. Irradiance levels**

Solar cells experience a wide range of irradiance levels during their outdoor operation. As solar cell efficiencies under different injection levels vary, the knowledge of aggregate insolation received is not sufficient for the accurate determination of energy yield. Information about the changing irradiance levels is needed.

The irradiance levels throughout a representative day for Denver and Singapore are shown in Figure 3.2.1 (a) and (b), respectively. For a clear day, which is quite

common in Denver, the irradiance level profile follows a bell shaped curve. In contrast, clear sky occurrences for extended time periods are extremely rare in tropical Singapore, where clouds play an important role in shaping the illumination conditions. The irradiance level is attenuated by the passage of clouds, which block the direct sunlight (dips in Figure 3.2.1b). However, the effects of clouds are more complicated at times. Reflections off the cloud edges cause a change in the intensity as well as the spectrum. This can *increase* the irradiance level received on the ground, an effect known as cloud edge effect [96, 97]. Clouds may also act as lenses, and this can potentially increase the irradiance level as well (cloud enhancement effects). Sometimes, this can boost ground received irradiance to more than the theoretical clear sky maximum [98]. Another consequence of clouds is a much larger share of diffuse light. In Singapore, the average diffuse share of the global irradiance is found to be more than 50% [99].

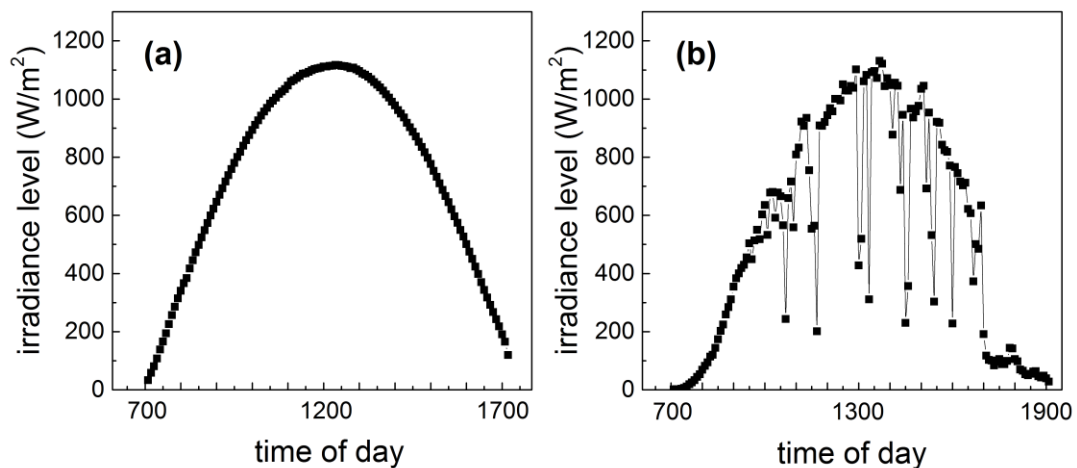


Figure 3.2.1: The daily irradiance level profile for (a) a clear and sunny day in Denver during February 2013, and (b) a partially sunny day with occasional cloud coverage in Singapore during February 2013.

With regard to overall PV power generation, it may be more relevant to look at the contribution to annual insolation by different irradiance levels. This distribution with respect to irradiance levels in units of Suns for Singapore and Denver for the year of 2013 is calculated and shown in Figure 3.2.2 (a) and (b), respectively. For Denver, most of the insolation is concentrated at higher irradiance levels around 0.8 Suns to 1 Sun. In contrast, the spread of available insolation in Singapore is more even. This implies that low to middle irradiance levels are also important for the annual PV energy generation in Singapore.

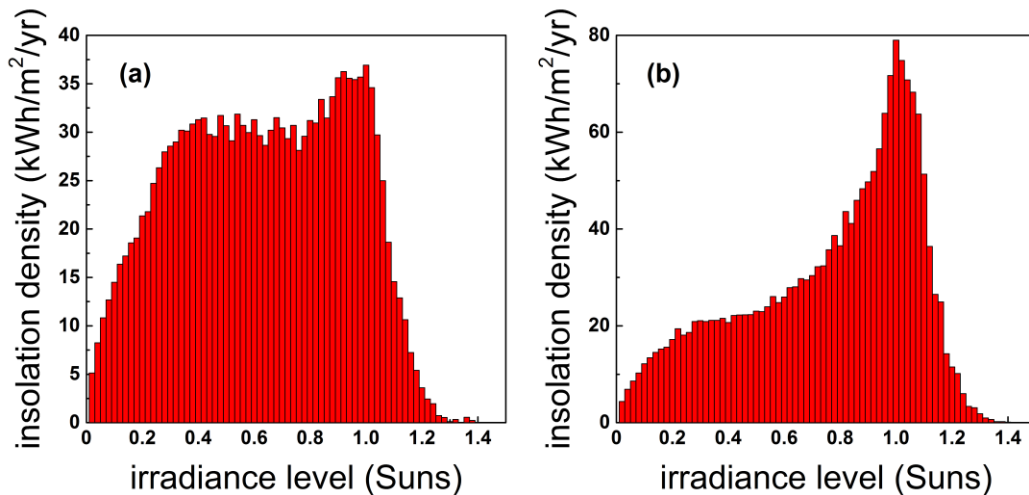


Figure 3.2.2: Distribution of solar insolation with respect to irradiance levels for (a) Singapore and (b) Denver.

### 3.2.2. Spectral compositions

Spectral composition is influenced by air mass, water vapour, aerosol optical depth, and several other atmospheric properties that determine the scattering and absorption of light during its passage through the atmosphere. Air mass is the relative pathlength of sunlight through the atmosphere [13]. It depends on the zenith angle

between the sun and the vertical. Low-latitude regions such as Singapore have, on average, lower air mass than high-latitude regions. Tropical Singapore also has a greater amount of precipitable water vapour. Therefore, the spectrum of Singapore differs considerably from both the AM1.5G spectrum and the spectrum of Denver. The average spectra for Singapore, Denver, as well as the AM1.5G spectrum are shown in Figure 3.2.3 for comparison. The spectra are all normalized to the same intensity in the shown wavelength ranges of 350 nm to 1060 nm. The spectrum of Denver is close to the AM1.5G spectrum, as Denver has very similar latitude and atmospheric conditions as those used to generate the AM1.5G spectrum. The spectrum for Singapore is considerably more blue-rich, and shows deeper troughs in the water absorption bands.

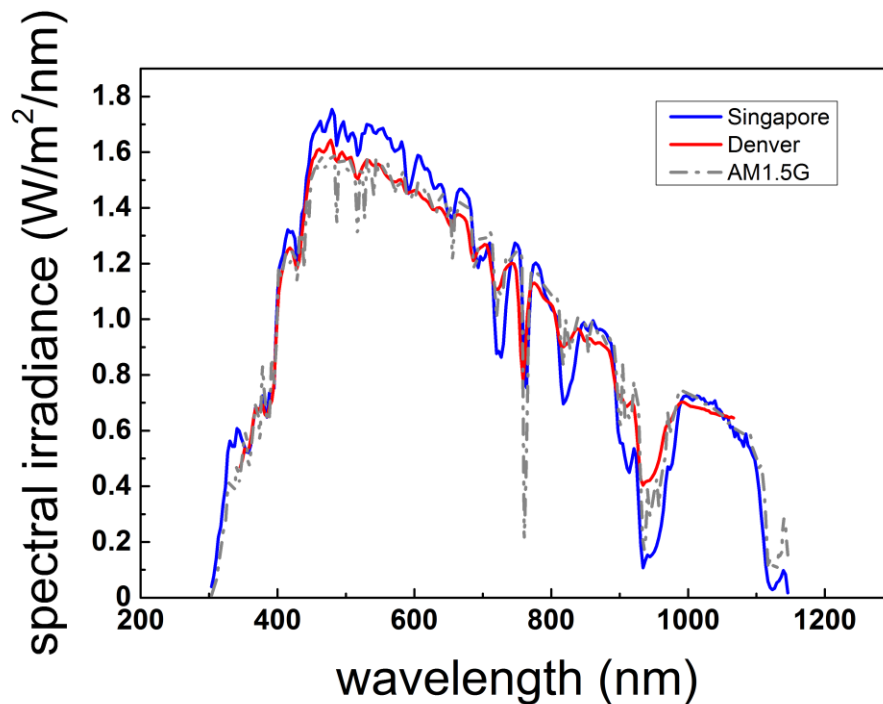


Figure 3.2.3: The average spectrum of Singapore and Denver, derived from measured data in the year 2013, shown together with the AM1.5G spectrum. The spectra are all normalized to the same intensity in the wavelength range of 350 nm to 1060 nm.

One way to characterize a spectrum is to determine its average photon energy (APE) value, which is calculated by dividing the integrated irradiance in a certain wavelength range by the total photon number in the same wavelength range:

$$APE = \frac{\int_{\lambda_1}^{\lambda_2} I(\lambda) d\lambda}{\int_{\lambda_1}^{\lambda_2} \Phi(\lambda) d\lambda} = \frac{\int_{\lambda_1}^{\lambda_2} I(\lambda) d\lambda}{\int_{\lambda_1}^{\lambda_2} \frac{I(\lambda)}{hc/\lambda} d\lambda} \quad (\text{Eq. 3.1})$$

where  $I(\lambda)$  is the wavelength resolved intensity distribution of a spectrum, and  $\Phi(\lambda)$  is the wavelength resolved photon flux density. APE values reported in this thesis use a wavelength range from 350 nm to 1060 nm, which is the wavelength range of the used spectroradiometer (EKO MS-700). The APE value characterizes how blue or red-rich a spectrum is. In general, the spectra in Singapore tend to be significantly more blue-rich than the AM1.5G spectrum, and have average APE values of over 1.9 eV. The APE of Denver's average spectrum is closer to the AM1.5G value of 1.87 eV. However, there is a wide variation in spectral compositions at different moments, and the average APE value is not sufficient for comprehensively describing the available illumination conditions. For illustration, we sorted the collected spectra in the year 2013 into bins of different APE values, with an interval width of 0.05 eV. Then we took the average spectrum within each bin and generated the representative spectra for different spectral compositions. These representative spectra are shown in Figure 3.2.4. It can be seen that a solar cell experiences a wide range of spectra during its outdoor operation. It is important to note that these sets are unique representations for the possible spectral compositions in a given location, despite some small variations in spectra for a certain APE [100]. In other words, one APE corresponds to only one spectral shape in a given location, with little variation over time. We have confirmed this observation for

Singapore and Denver. The characteristic set of spectra is, thus, a very useful representation, and can be used to obtain the solar cell efficiency as a function of APE.

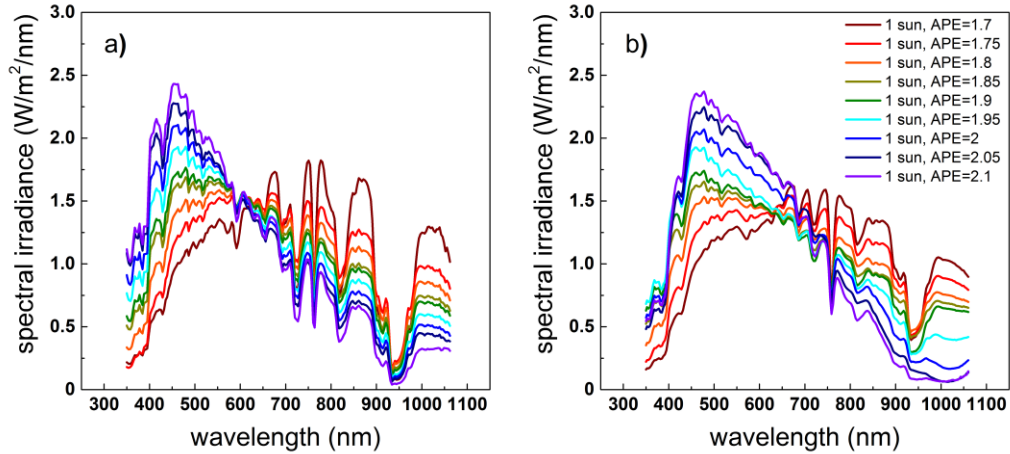


Figure 3.2.4: Characteristic set of spectra in (a) Singapore and (b) Denver. All spectra are scaled to the same intensity as the standard AM1.5G spectrum. The APE values indicate the left bound of the interval.

Different spectra do not occur with the same frequency and intensity. Figure 3.2.5 shows the contribution of annual insolation by different spectra, characterized by their APE values. The distributions for the two locations are different. For Singapore, the spectral composition that contributes most to PV energy generation has an APE value in the 1.90 - 1.91 eV range, the available energy falls off exponentially from this value. In contrast, the APE of the AM1.5G spectrum is 1.87 eV, which is more red-rich. For Denver, more contribution comes from spectra with APE values between 1.85 eV and 1.90 eV. This reflects the distinctly different climatic and atmospheric conditions prevalent in these two different locations. This has important implications for tandem solar cell designs as well as operations, as will be shown in Chapter 6.

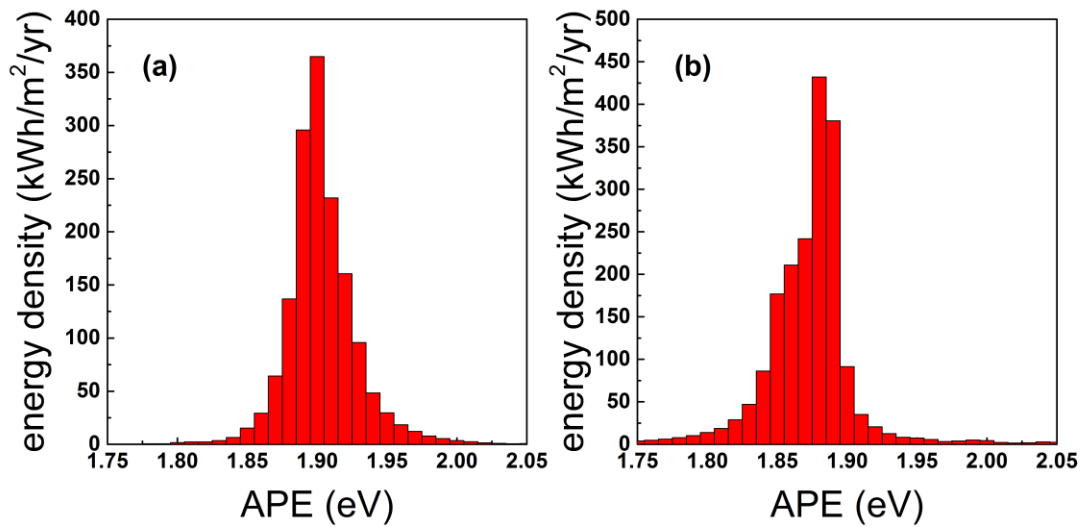


Figure 3.2.5: Distribution of solar insolation with respect to APE for (a) Singapore and (b) Denver.

### 3.2.2.1. Correlation between spectral composition and intensity

Through examination of solar irradiance and spectra data, it was observed that spectral composition has some degree of correlation with the irradiance level. Figure 3.2.6 shows the time series of irradiance levels and APE values for an average day in Singapore. It is the same partially sunny day as was used in Figure 3.2.1, which is typical for Singapore. It can be observed that the APE values tend to rise when there is a dip in the irradiance level. This is most likely due to an increase of the diffuse share of the irradiance (which is blue-rich as a result of more scattering in the short-wavelength range) when clouds blocked direct sunlight. Also, cloud reflections of sunlight may cause the spectrum to be additionally blue-shifted. In Figure 3.2.7, the daily average APE values of the spectra versus daily insolation in the year of 2014 is obtained and plotted for Singapore as well as Denver. APE is correlated negatively to insolation in a roughly linear way for Singapore. The correlation is more complicated

in the case of Denver, where seasonal variations of climate and sun positions are more prominent.

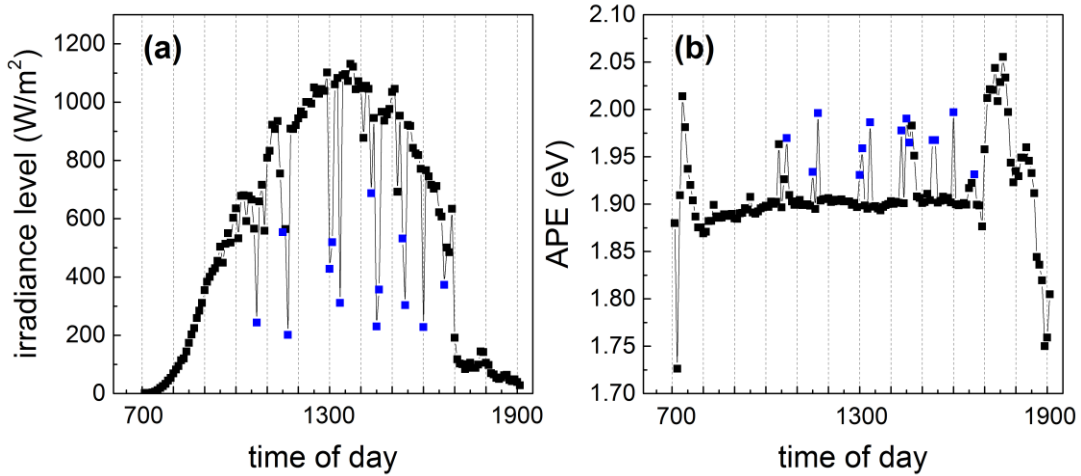


Figure 3.2.6: The time series of (a) irradiance level and (b) APE value for an average day in Singapore. The data points marked blue in (b) correspond to those marked blue in (a). In general, APE values rise when there is a dip in the irradiance level.

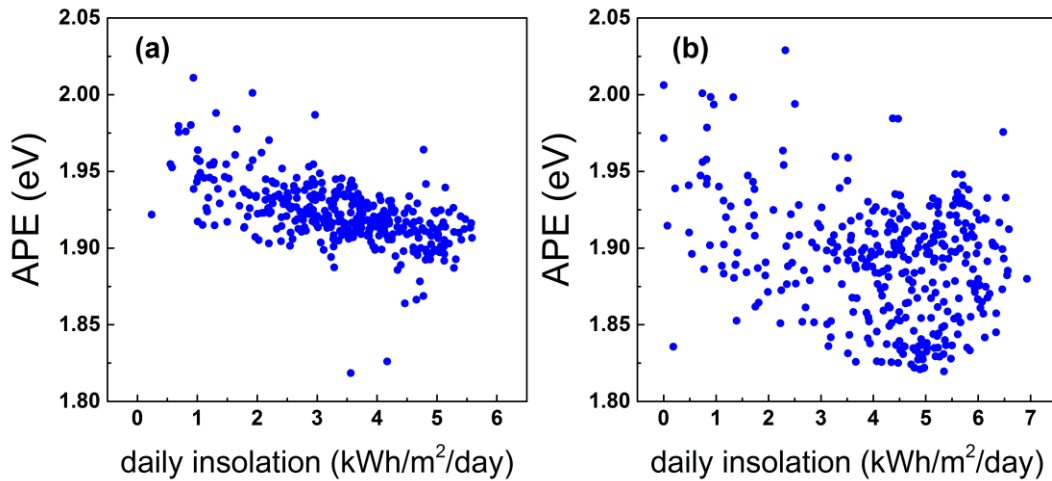


Figure 3.2.7: The daily average APE value of the spectra versus daily insolation in the year of 2014 for (a) Singapore, and (b) Denver. APE seems to be correlated negatively to insolation in a roughly linear way for Singapore. The correlation is more complicated in the case of Denver, where seasonal variations of climate and sun positions are more prominent.

To examine the correlation more closely, statistical analysis is performed on the complete dataset of Singapore and Denver. The Singapore dataset consists of the following parameters, with one data per 5 minutes: global irradiance level, diffuse



irradiance level, temperature, APE values, and air mass. The Denver dataset contains the same parameters as Singapore, with the additional meteorological parameters of cloud coverage (in terms of percentage values, as analysed from sky images), albedo, and relative humidity. Using a univariate linear regression model and analysis of variance (ANOVA), the correlation between APE and irradiance level is quantified. In ANOVA, the effect size quantifies the magnitude of change of the observed variable given a unit change of predictor variable, and the p-value indicates the probability of obtaining a result equal to, or more extreme than the actually observed variation, given the assumed null-hypothesis of no correlation. In other words, a small p value indicates the likely existence of correlation. For both Singapore and Denver, a negative effect size and very small p value ( $< 0.0001$ ) is obtained, which confirms a statistically significant negative correlation.

To adjust for possible confounding effects from other variables such as air mass and albedo, a multivariate model is implemented as well. The analysis results for the multivariate regression model are shown in Table 3.2.1 for Singapore and Table 3.2.2 for Denver. For Singapore, it is found that both irradiance level and diffuse fraction are strong predictors of APE, with p values smaller than the threshold value of 0.05. With the effect size of  $-4.33 \times 10^{-5}$ , per  $200 \text{ W/m}^2$  irradiance level increase leads to around 0.01 eV decrease of APE, which corresponds to a significant spectral change that produces visible effects for the energy yield of tandem solar cells. Arguably the effect of the diffuse fraction is larger, as every 10% increase in diffuse fraction leads to 0.025 eV increase in APE. In Singapore, air mass alone is not a good predictor of spectral composition, due to the stronger influence of clouds and other factors.

Therefore, it only appears as a confounding variable here. For Denver, it is found that APE is significantly correlated with all investigated variables, except the albedo.

Table 3.2.1: The effect size and p value for a multivariate regression model  $APE = b_1 \cdot \text{irradiance level} + b_2 \cdot \text{air mass} + b_3 \cdot \text{diffuse fraction}$ , applied to variables of Singapore.

Variables	Effect size	p value
Irradiance level	$-4.326 \times 10^{-5}$	< 0.0001
Air mass	$-3.865 \times 10^{-6}$	0.0878
Diffuse fraction	$2.514 \times 10^{-3}$	< 0.0001

Table 3.2.2: The effect size and p value for a multivariate regression model  $APE = b_1 \cdot \text{irradiance level} + b_2 \cdot \text{air mass} + b_3 \cdot \text{cloud coverage} + b_4 \cdot \text{albedo} + b_5 \cdot \text{relative humidity}$ , applied to variables of Denver.

Variables	Effect size	p value
Irradiance level	$-3.712 \times 10^{-5}$	< 0.0001
Air mass	$-2.127 \times 10^{-4}$	0.0003
Cloud coverage	$3.215 \times 10^{-7}$	< 0.0001
Albedo	$-3.784 \times 10^{-7}$	0.414
Relative humidity	$5.808 \times 10^{-4}$	< 0.0001

### 3.2.3. Distribution map of illumination conditions

To concisely summarize the information about outdoor illumination conditions within a certain time period, a distribution map describing the occurrence duration of different conditions is calculated and used for yield calculation in this thesis. This is obtained by sorting the measured solar irradiance data according to different APE and

intensity levels (I), and by determining how often these conditions occur. This distribution map describes the time duration  $t(\text{APE}, I)$  during which a condition with a certain APE and intensity occurs, and can be seen as a fingerprint of the illumination conditions at a given location. This is found to be a useful way of representation that includes both irradiance levels and spectral composition at the same time. The annual distributions for Singapore and Denver in 2013 are illustrated in Figure 3.2.8. It can be seen that the distributions are distinctly different for the two locations. The distribution map of illumination conditions obtained from these datasets will be used to compute the energy yield of tandem cells, as will be explained in Chapter 5. The distribution map in terms of insolation content is shown in Figure 3.2.9. It can be seen that very low intensity irradiation does not contribute much to total insolation, despite long duration of occurrence.

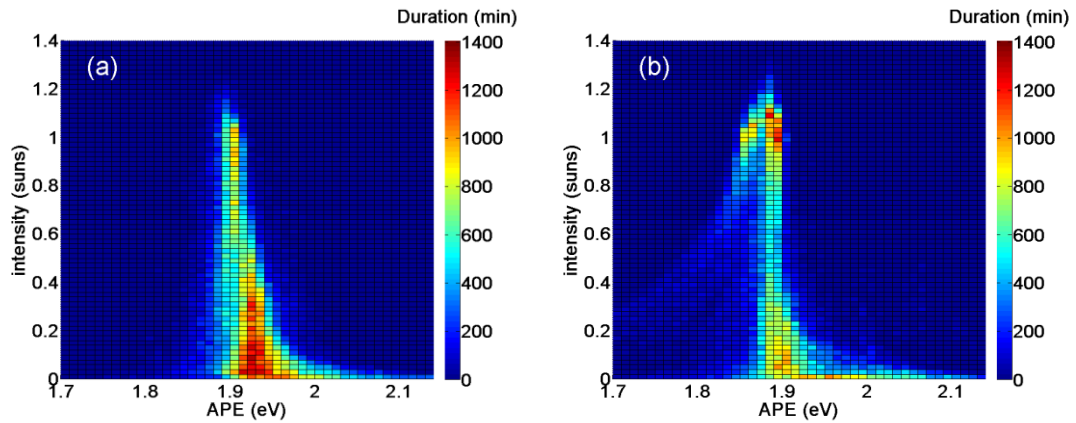


Figure 3.2.8: Annual occurrence distribution of illumination conditions for (a) Singapore and (b) Denver in the year 2013.

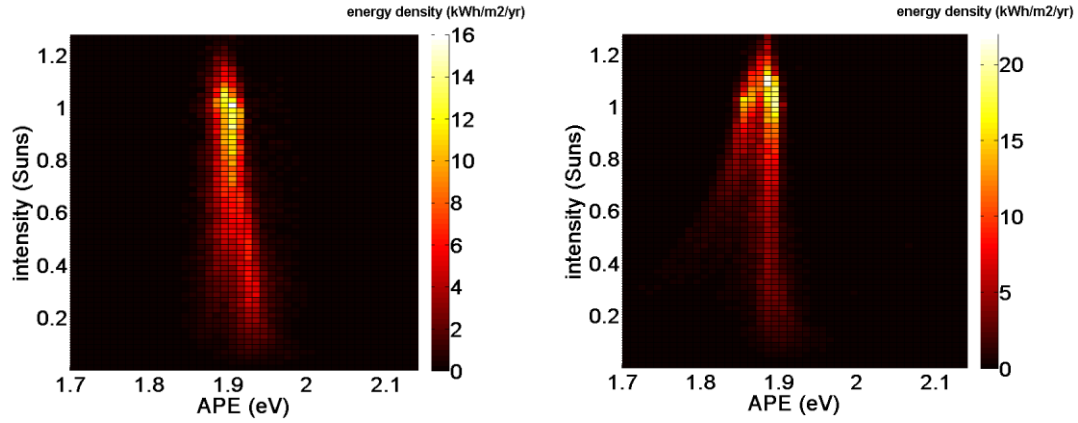


Figure 3.2.9: The distribution of insolation content with respect to APE and intensity levels for Singapore (left) and Denver (right) in the year 2013.

### 3.2.4. Operating temperatures and others

The operating temperature of a solar cell can vary significantly, depending on the ambient air temperature, solar irradiance level, wind speed, the design and also the mounting environment of the corresponding PV module. Prediction of operating temperatures based on the physical modelling of thermal environment and heat transfer is generally challenging. Instead, numerous empirical models exist [101-106]. A basic model relates cell temperature to ambient air temperature and irradiance level by a linear model [103, 107]:

$$T_c = T_a + kG_T \quad (\text{Eq. 3.2})$$

where  $k$  is known as the Ross coefficient. The range of Ross coefficient normally encountered is in the range of 0.02 to 0.06 K m<sup>2</sup>/W [104]. This depends on the type of the PV array as well as the mounting scheme. A preliminary estimation of III-V/Si tandem solar cell operating temperatures will be done in Chapter 4, based on the air temperature and solar irradiance data available for Singapore and Denver. The

distribution of annual insolation with respect to the occurring air temperature in 2013 is shown in Figure 3.2.10.

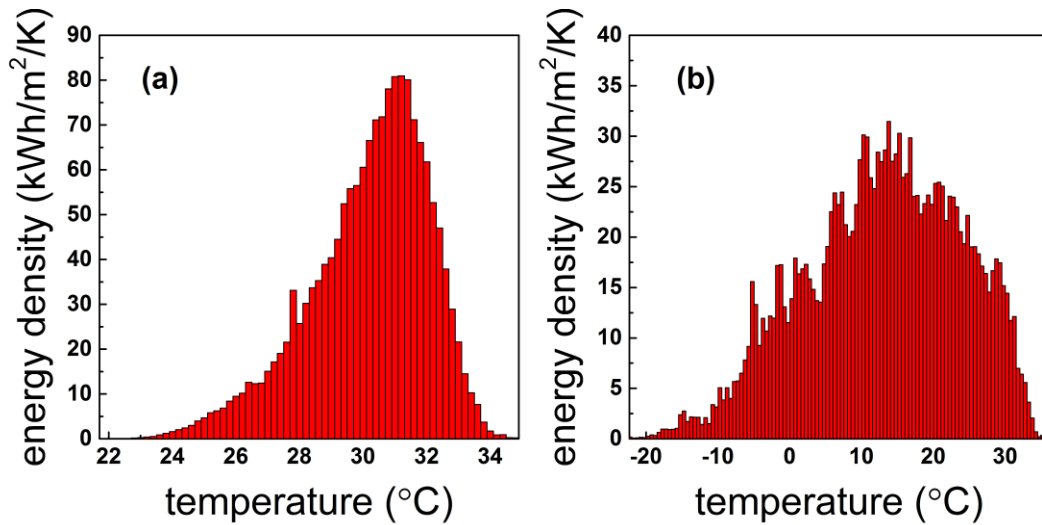


Figure 3.2.10: The distribution of annual insolation content with respect to the ambient air temperature for (a) Singapore and (b) Denver in the year 2013.

Other outdoor factors that influence PV operation include shading, soiling, and reflection. These factors are relevant for performance analysis at the module level, since they affect the whole module instead of individual solar cells. They are also more specific to project sites and installation types, thus are harder to generalize. These factors are out of the scope of this thesis and are thus not considered.

### 3.3. Year to year variations

Solar irradiance on the ground varies from year to year, and as a consequence the solar cell performance (both total energy generated and power conversion efficiency) varies as well. It is, thus, important to quantify the amount of variation that can be

expected. In terms of annual total, it was found that the ground horizontal insolation in Singapore shows less than 10% variation from the average [99]. For Denver, the variation in tilted global irradiance (40°, facing south) is less than 5% from the average, based on the irradiance datasets for the years 2011 to 2015.

To estimate the year-to-year variations in the spectrum, the annual distribution of spectral composition is computed from 2013 to 2015. The distributions for Singapore and Denver are shown in Figure 3.3.1 and Figure 3.3.2, respectively. The peak, variance and skewness of the distributions are quite consistent throughout the years. With no prior assumption of what distribution it is, a nonparametric test - the paired Wilcoxon signed rank test [108] - is used to compare the year-to-year variation. It is found that the p value is 0.003 for Singapore and 0.43 for Denver. This implies that there is virtually no year-to-year variation for Denver, and a very small amount of year-to-year variation for Singapore. Therefore, it is expected that the effect of spectral variations on the tandem solar cell are relatively consistent from year to year.

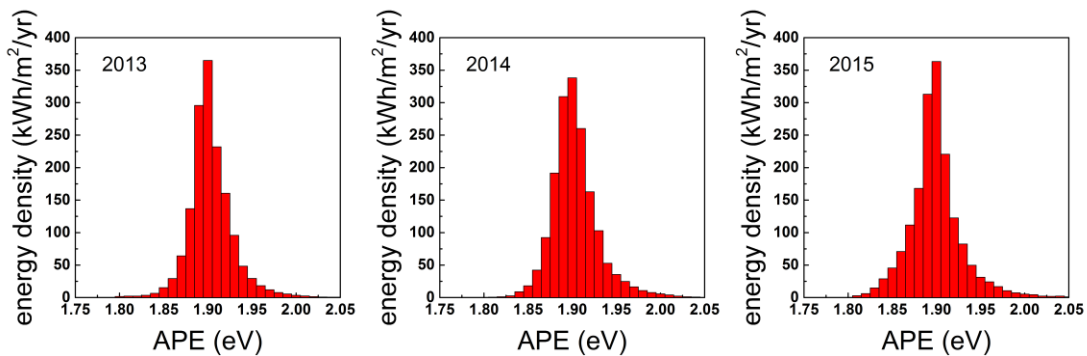


Figure 3.3.1: Comparison of insolation distribution with different spectral compositions across three years, 2013 to 2015, in Singapore.

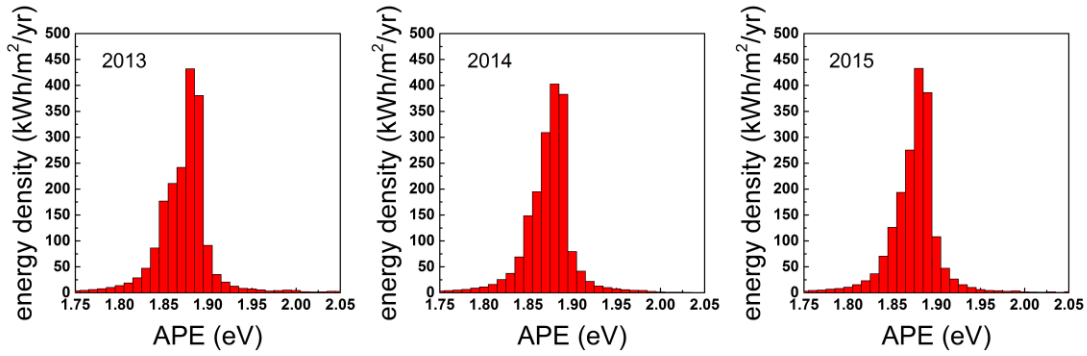


Figure 3.3.2: Comparison of insolation distribution with different spectral compositions across three years, 2013 to 2015, in Denver.

### 3.4. Chapter summary

In this chapter, realistic outdoor operating conditions were illustrated using measured datasets of solar irradiance and ambient air temperature in Singapore and Denver. The general background of irradiance level and spectrum measurement was introduced, and the experimental measurement set-ups for the datasets used in this thesis was described. From the measured data, it was observed that the illumination conditions in Singapore and Denver are significantly different. In comparison, Singapore has more fluctuations in the irradiance level, due to the abundance of clouds. Most insolation comes from high irradiance levels in Denver, but in Singapore a significant portion of the insolation is contributed by low to medium irradiance levels. The spectral compositions for Singapore and Denver are also very different. The average spectrum in Singapore is more blue-rich than that of Denver. In addition, it was found that the spectral composition and the irradiance level are negatively correlated, particularly for Singapore. Further, using the average photon energy (APE) to characterize the spectral composition, a characteristic set of spectra was calculated for each location. This characteristic set of spectra is unique and relatively time

invariant for a fixed location. The illumination conditions were obtained by sorting measured spectra based on intensities and APE values. This summary, which is called the distribution map of illumination conditions, will be used in subsequent chapters for computing the energy yield of tandem solar cells. The difference in the illumination conditions is expected to result in different tandem solar cell performances. This will be explored in the analysis of yield and outdoor losses in later chapters. Finally, an empirical model relating operating temperature, ambient air temperature and irradiance level was introduced. Year to year variations in illumination conditions were found to be relatively small.



## **Chapter 4. Modelling of tandem solar cells and their efficiencies under various conditions**

As seen in Chapter 3, a tandem solar cell in a flat-plate PV module deployed outdoors may experience a wide range of operating conditions. To determine the energy yield at a certain location, the tandem solar cell performance under varying operating conditions needs to be known. Tandem solar cell response to changing solar spectrum, light intensity, and cell temperature may be significantly different from that of single-junction solar cells. This is particularly so for 2-terminal devices due to current matching issues. In this chapter, device modelling is used to estimate tandem solar cell outputs. Modelling tandem solar cells is generally more challenging than modelling single-junction solar cells, and there exists only a limited number of software packages that can do it. In this chapter, an alternative and time-saving way of modelling tandem solar cells using transfer matrix method (TMM) optical calculations coupled with PC1D device simulations is used to obtain the tandem solar cell performance under various illumination conditions. The simulation framework and device models used are introduced first, followed by simulated tandem cell efficiencies under standard testing conditions (STC). We also investigate the impact of different sub-cell combinations on the STC PV efficiency. Subsequently, the tandem solar cell efficiencies under varying illumination conditions relevant to yield calculation are determined. In addition, common temperature coefficients of sub-cell materials are used to predict the temperature dependence of tandem solar cells.

## **4.1. Simulation framework**

### **4.1.1. Overview**

Device simulation is used to predict tandem solar cell output under STC, as well as various other input illumination conditions. As a tandem solar cell contains more than one junction, its simulation is generally more complicated than that of single-junction cells. Sub-cells can be connected via a tunnel junction or a mechanical integration scheme. Proper description of the optical and electrical properties of the tunnel junction or interconnection components, on top of proper physical models for the sub-cells, is needed to obtain accurate tandem device behaviour. Simulation packages such as Sentaurus TCAD or Silvaco Atlas can be used to achieve good simulation results. However, this requires setting up elaborate physical models for the device, and consumes much computation power during execution. This approach is most useful for studying particular physical phenomena in the device, fine tuning of processing, and for design optimization. Usually it also requires reference physical devices for calibration of input parameters. The objective at this early stage of theoretical investigation of tandem solar cells for flat-plate PV module applications is to estimate their qualitative behaviour; thus, PC1D device simulation is used instead.

PC1D is a well-established 1D solver of semiconductor device properties that solves the diffusion and continuity equations self-consistently [109]. In PC1D device simulation, the properties and parameters for 1D semiconductor regions or surfaces are first defined. The solver then meshes the regions using finite elements to solve for Boltzmann transport equations, continuity equations, and Poisson equation. It requires

little computation power and can generate results in a short time. However, one difficulty with using PC1D is that it is unable to simulate a tandem solar cell. Therefore, in this work optical calculation is performed first for the whole tandem structure using the transfer matrix method (TMM) [27], which can analyze the propagation of electromagnetic waves through layered mediums. In TMM, the electromagnetic field at the end of a layer is calculated from the known field at the beginning of the layer based on continuity conditions across boundaries, using a matrix operation. A system of multiple layers can be represented as a system matrix, which is obtained by combining transfer matrix of individual layers. The electrical calculation for each sub-cell is subsequently done separately by PC1D, using the photogeneration profiles obtained in the optical calculation. The overall electrical characteristics of the tandem device are then calculated by summing the I-V curves of the sub-cells. The simulation process flow is illustrated in Figure 4.1.1.

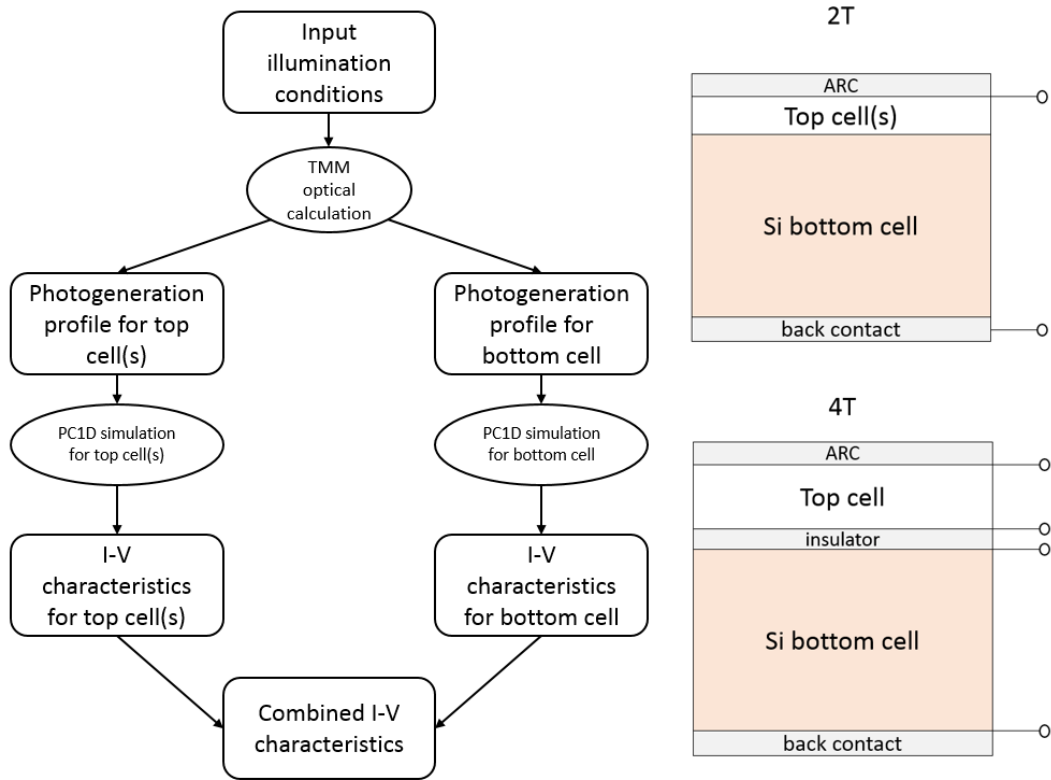


Figure 4.1.1: The process flow for simulating a tandem solar cell (left), and the 1D schematics of the tandem device structures to be simulated (right). Both 2-terminal (2T) and 4-terminal (4T) configurations are investigated. The insulator layer in 4T is only conceptual and has zero thickness in the simulated device structure.

To assess realistic tandem solar cell efficiencies, published material parameters of fabricated and characterized solar cells are used to simulate each sub-cell. The Si cell and III-V cell models are presented in Sections 4.1.2 and 4.1.3, respectively. Sub-cell parameters that represent mature or commercially available solar cells are chosen, in order to investigate tandem solar cells that have a realistic chance of being practically realised using existing technologies. As shown in Figure 4.1.1, the tandem device structures to be simulated include both 2-terminal (2T) and 4-terminal (4T) configurations. In this work only a simplified 1D structure is considered, and thus 2D

effects like contact patterns and surface textures are ignored. We also do not include losses related to adhesive interconnection layers or tunnel junctions. Only the 2T contact scheme is considered for triple-junction tandem cells; both contact schemes, 2T and 4T, are considered for double-junction GaAs/Si and InGaP/Si solar cells. It should be noted that the interconnection schemes for 4T will affect the optics, but this effect is not considered in this thesis for simplicity and for a more direct comparison between 2T and 4T to quantify the extent of current mismatch losses. More details on the tandem model will be presented in Section 4.2.

#### **4.1.2. Device models for Si bottom cell**

There are many different types of crystalline Si solar cells, classified according to different processing technologies, device architectures, material types or material qualities. There are also some distinctions between laboratory solar cells and mass-produced industrial solar cells. Common types of crystalline Si solar cells are [110]:

- p-type Aluminium Back-Surface-Field (Al-BSF) crystalline Si solar cells with screen-printed metallization [111],
- diffused-junction solar cells on Upgraded Metallurgical Grade (UMG) multicrystalline Si wafers [112],
- p-type Passivated Emitter and Rear Cell (PERC) crystalline silicon solar cells [113],
- Passivated Emitter Rear Locally diffused (PERL) solar cells [114],
- n-PASHA bifacial n-type cells [115],

- n-type heterojunction (HJT) solar cells [10],

and various others. Different types of solar cells have different efficiency levels; different external quantum efficiencies (EQE), different passivation qualities and voltages, and different costs.

In this study, three different Si solar cell models are chosen: (a) p-type UMG multi-Si wafer with screen-printed contacts and full-area Al-BSF at the rear, abbreviated as UMG-Si, (b) Same cell structure as (a) but with a standard-quality (“solar-grade”) p-type multi-Si wafer, abbreviated as multi-Si, and (c) p-type monocrystalline PERC solar cell, abbreviated as PERC-Si. These three models represent three different levels of absorber material quality and conversion efficiency. The UMG-Si model represents a low-cost approach using the cheapest feedstock material, as UMG Si is cheaper than standard grade (or “solar grade”) Si used in PV. However, this model has the lowest PV efficiency. The multi-Si model represents the industrial standard, and has a moderate PV efficiency. The PERC-Si model represents a high-efficiency concept, but is also more expensive (in terms of \$/W). The device parameters used for the PC1D simulations are listed in Table 4.1.1. The parameter values can in fact differ significantly even for the same type of solar cell. The numbers listed in Table 4.1.1 are chosen to reflect typical values from the literature [110-113, 116]. Using the cell models, and assuming a planar cell structure with  $\text{SiN}_x$  antireflection coating (ARC), the  $V_{oc}$ ,  $J_{sc}$  and efficiency for a stand-alone Si cell under AM1.5G illumination were simulated and are shown in Table 4.1.1. Since a planar structure (i.e., no surface texture) is assumed, the cell efficiencies are lower than what is usually achieved for their textured counterparts. Also, all the Si models presented here have lower efficiencies

than the record-level Si solar cells, which are 25-26 % efficient [117]. The Si cell models of the present work were chosen because they represent Si solar cells that can be mass produced readily with relatively low costs (\$/W).

Table 4.1.1: Device parameters for the three Si solar cell models used in this thesis. The simulated outputs for a planar cell with SiN<sub>x</sub> antireflection coating (ARC), using the three cell models, together with typical efficiencies realized by these technologies, are also shown.

	(a) UMG-Si [112, 116]	(b) Multi-Si [110, 111]	(c) PERC-Si [110, 113]
Thickness (μm)	200	200	200
Background doping (cm <sup>-3</sup> )	8×10 <sup>17</sup> (p-type)	1.5×10 <sup>16</sup> (p-type)	7.2×10 <sup>15</sup> (p-type)
Emitter doping (cm <sup>-3</sup> )	6×10 <sup>20</sup> (n-type, Erfc)	7.2×10 <sup>20</sup> (n-type, Erfc)	8.9×10 <sup>19</sup> (n-type, Erfc)
Bulk lifetime (μs)	10	200	360
Surface recombination velocity (cm/s)	Front 6×10 <sup>5</sup> Back 1×10 <sup>3</sup>	Front 6×10 <sup>5</sup> Back 1×10 <sup>3</sup>	Front 5×10 <sup>4</sup> Back 80
$V_{oc}$ (mV)*	601	621	656
$J_{sc}$ (mA/cm <sup>2</sup> )*	30.8	33.8	36.1
Simulated efficiency*	14.0%	16.7%	19.1%
Typical efficiencies of industrial cells (textured)	14 - 15 %	17.5 - 18.5 %	20 - 21 %

\* Values are for planar cells with ARC under AM1.5G illumination.

#### 4.1.3. Device models for III-V top cells

III-V solar cells can be made by epitaxial growth on a suitable substrate using Liquid Phase Epitaxy (LPE), Molecular Beam Epitaxy (MBE) or Metal-Organic Chemical Vapour Deposition (MOCVD) [3]. The solar cell efficiency depends on the film quality, doping, window layer materials used and interface passivation. In general, the bulk carrier lifetime (i.e., the electronic quality of the film), is related to the threading dislocation density (TDD) in the film [118], which in turn is influenced by the substrate and the process control during epitaxial growth. Most high-quality III-V solar cells nowadays are made using MOCVD. The cost (\$/W) is high due to expensive equipment, expensive substrates, and low throughput [33].

In this thesis, two GaAs models and one InGaP model are used. The two GaAs models represent a baseline moderate-efficiency GaAs solar cell [119] and an advanced high-efficiency GaAs solar cell [11, 120, 121], respectively. The InGaP model represents a high-quality but not record-efficient InGaP solar cell [39, 122, 123]. The device parameters for the absorber layers (excluding the window layers, i.e. high bandgap passivating layers usually used in III-V solar cells) are listed in Table 4.1.2. The  $V_{oc}$ ,  $J_{sc}$  and simulated efficiency for a stand-alone cell with MgF/ZnS double-layer ARC and back reflector give an indication of cell quality. It should be noted that photon recycling may affect the efficiency of III-V solar cells [124, 125]. The extent of influence depends on the optical features, which determine the trapping of re-emitted photons within the III-V cell and the luminescent coupling with other sub-cells. The effect is strongest at open circuit, where the excess carrier density is largest, but is less significant at the maximum power point and least significant at short-circuit conditions.



Collaborators at SMART (Singapore-MIT Alliance for Research and Technology) have developed a code that can include photon recycling and luminescent coupling in PC1D simulations [126]. For simplicity, the simulation results presented here do not include this effect. The effect of photon recycling on yield results will be briefly discussed in Chapter 6.

Table 4.1.2: The device parameters for two GaAs and one InGaP cell models used in this thesis. The simulated outputs for a planar cell with MgF/ZnS double layer antireflection coating (ARC), using the three cell models, together with typical efficiencies realized by these technologies, are also included.

	Baseline GaAs	Advanced GaAs	InGaP
Thickness ( $\mu\text{m}$ )	2	2	1
Background doping ( $\text{cm}^{-3}$ )	$1 \times 10^{17}$ (p-type)	$1 \times 10^{17}$ (p-type)	$1 \times 10^{17}$ (p-type)
Emitter doping ( $\text{cm}^{-3}$ )	$1 \times 10^{18}$ (n-type)	$6 \times 10^{17}$ (n-type)	$3 \times 10^{18}$ (n-type)
Bulk lifetime (ns)	4	28	2
Surface recombination velocity (cm/s)	Front $7 \times 10^4$ Back $7 \times 10^4$	Front 2600 Back 30	Front 5800 Back 5800
$V_{oc}$ (mV)*	996	1066	1405
$J_{sc}$ ( $\text{mA}/\text{cm}^2$ )*	29.9	30.3	16.0
Simulated efficiency*	24.7%	28.1%	19.2%
Typical efficiencies	24%	28%	19%

\* Values are for solar cells with ARC and back reflector under AM1.5G illumination.

## **4.2. Tandem models and efficiencies under STC**

There are many possible combinations of sub-cell technologies when making a tandem solar cell using wafer bonding or mechanical stacking. Different combinations of sub-cells result in different tandem cell efficiencies, which can be higher or lower than those of the individual sub-cells alone. They also have different cost (\$/W). While it is straightforward to estimate what is required to reach high efficiencies, it is still unclear which particular technology is the most cost-effective in terms of \$/W. As a first step, the efficiency gain by integrating the sub-cells needs to be estimated in order to determine the optimal combination. In this study, the STC efficiencies of double-junction tandem solar cells with several sub-cell combinations are simulated using the sub-cell models described in Sections 4.1.2 and 4.1.3. The objective is to quantify the benefit of sub-cell integration in terms of efficiency improvements. The tandem models selected for the energy yield calculation are then listed.

### **4.2.1. Double-junction efficiencies for various sub-cell combinations**

The simulated 2T and 4T double-junction tandem efficiencies are shown in Figure 4.2.1. The typical single-junction cell efficiencies using individual sub-cell technologies are also indicated. The top cell thicknesses are always adjusted to maximize the double-junction tandem efficiency. Note that for 2T GaAs/Si, the top cell thickness is thinned to give a matched current with the Si bottom cell. A thicker GaAs top cell is used for the 4T GaAs/Si configuration so that more high-energy photons are absorbed in the top cell, thereby giving higher PV efficiency. It can be seen that for 2T

GaAs-on-Si tandem solar cells, having a low-efficiency UMG-Si or multi-Si bottom cell results in a lower tandem efficiency than the GaAs top cell alone. Therefore, there is no benefit in such a sub-cell combination. An increase in the bottom cell efficiency brings about a proportional increase in the 2T tandem cell efficiency. Therefore, in order for the combination to be beneficial, it is important that the bottom cell has a sufficiently high efficiency, on a similar level as the top cell efficiency.

The 4T configuration always gives a higher tandem cell efficiency than the top cell alone. However, it remains a question whether the efficiency boost can justify the additional cost. In the (likely) case where the cost of a baseline GaAs solar cell is not significantly lower than that of an advanced GaAs solar cell, it is more desirable to use the more efficient GaAs top cell. For InGaP-on-Si tandem solar cells, the benefit of integration is considerably higher. The efficiency difference between 2T and 4T is also lower. However, for the sub-cell models considered here, none of the combinations surpassed the efficiency of world-record single-junction GaAs solar cells. Better InGaP top cells and Si bottom cells need to be used in order for InGaP/Si tandem cells to be competitive.

The conditions under which a tandem solar cell is more cost-effective in terms of Levelised Cost of Electricity (LCOE) than a single-junction solar cell are still to be identified. A cost modelling framework required to do this is recently developed at MIT [127]. In this thesis, only the tandem cell models presented in Section 4.2.2 are considered in the energy yield calculation, but not the other tandem configurations described in this section (4.2.1).

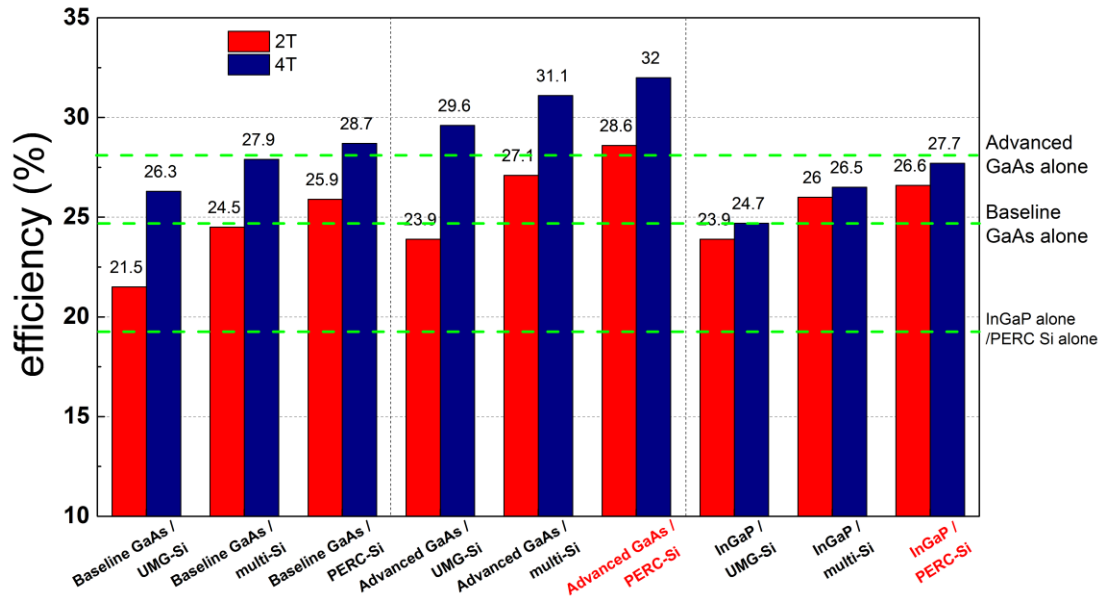


Figure 4.2.1: Simulated STC efficiencies for 2T and 4T double-junction tandem solar cells with different sub-cell combinations. The typical single-junction cell efficiencies using individual sub-cell technologies are indicated as green lines. The tandem configurations written in red text along the horizontal axis are selected for further energy yield studies.

#### 4.2.2. Tandem models for energy yield calculations

The tandem solar cells investigated in the energy yield calculations include: 2T GaAs/Si, 4T GaAs/Si, 2T InGaP/Si, 4T InGaP/Si, 2T InGaP/GaAs/Si, and 2T GaAs/GaAs/Si. For each tandem solar cell configuration chosen for yield calculation, only the best sub-cell models are chosen, and the top cell thicknesses are adjusted to maximize the tandem efficiency. As seen in the previous section, this combination is most likely to be beneficial. Details about the tandem models are listed in Table 4.2.1. It should be noted that ultra-thin (i.e. with sub-micron thickness) GaAs sub-cells are used for the 2T GaAs/Si and GaAs/GaAs/Si tandems, but an ultra-thin GaAs solar cell with good efficiency is yet to be demonstrated. In practice, the efficiency of an ultra-thin GaAs sub-cell may be lower than what is simulated by PC1D model used here.

This is due to additional quantum effects such as back diffusion and contact to contact diffusion, according to a theoretical investigation by Cavassilas et al. [128]. For InGaP/Si, a good Si bottom cell usually produces excess current in the InGaP/Si tandem, as the maximum short-circuit current of InGaP solar cells achieved so far is only about 16 mA/cm<sup>2</sup> [39, 129]. The 2T InGaP/Si is almost current matched here; however, this is only the case because a *planar* Si bottom cell (which produces less current) is considered.

Table 4.2.1: Device architectures and parameters for the tandem models used in energy yield calculations. The simulated sub-cell output and STC tandem efficiency is also shown.

	GaAs/Si	InGaP/Si	InGaP/GaAs/Si	GaAs/GaAs/Si
Sub-cell thicknesses (μm)	0.2 / 200 (2T) 1 / 200 (4T)	2.5 / 200 (both 2T and 4T)	0.285 / 0.65 / 200	0.095 / 0.45 / 200
Background doping (cm <sup>-3</sup> )	p - 1×10 <sup>17</sup> / p - 1.5×10 <sup>16</sup>	p - 1×10 <sup>17</sup> / p - 1.5×10 <sup>16</sup>	p - 1×10 <sup>17</sup> / p - 1×10 <sup>17</sup> / p - 1.5×10 <sup>16</sup>	p - 1×10 <sup>17</sup> / p - 1×10 <sup>17</sup> / p - 1.5×10 <sup>16</sup>
Emitter doping (cm <sup>-3</sup> )	n - 6×10 <sup>17</sup> / n - 7.2×10 <sup>20</sup>	n - 3×10 <sup>18</sup> / n - 7.2×10 <sup>20</sup>	n - 6×10 <sup>17</sup> / n - 3×10 <sup>18</sup> / n - 7.2×10 <sup>20</sup>	n - 6×10 <sup>17</sup> / n - 6×10 <sup>17</sup> / n - 7.2×10 <sup>20</sup>
Bulk lifetime (μs)	0.028 / 360	0.002 / 360	0.002 / 0.028 / 360	0.028 / 0.028 / 360
Sub-cell V <sub>oc</sub> (mV)*	1105 / 639 (2T) 1082 / 622 (4T)	1408 / 635	1392 / 1065 / 625	1113 / 1077 / 630
Sub-cell J <sub>sc</sub> (mA/cm <sup>2</sup> )*	19.4 / 19.6 (2T) 28.5 / 10.2 (4T)	15.9/ 16.8	11.4 / 11.5 / 11.6	13.0 / 13.0 / 13.5
STC efficiencies	28.6% (2T) 32.0% (4T)	27.7% (2T) 27.9% (4T)	29.9%	31.4%

\* Values are for sub-cells inside the tandem structure under AM1.5G illumination.

### **4.3. Tandem efficiencies under non-standard conditions**

In the field, solar cell operating conditions can deviate significantly from STC. The knowledge of tandem solar cell behaviour under various operating conditions is thus very important for studying their energy yield. This section presents the simulated tandem solar cell efficiencies under a range of possible illumination conditions, with differing spectral composition and intensity levels. Their temperature dependent performance and potential outdoor operating temperatures are also discussed.

#### **4.3.1. Efficiencies under varying spectra and light intensity**

Tandem solar cells are sensitive to spectral variations. When the spectrum changes, the current generation in the sub-cells also changes. For 2-terminal devices, where the sub-cells are series connected, the cell that produces the lowest current will limit the overall current. Therefore, the overall efficiency is high only when all sub-cells generate an approximately equal current. When the spectral composition deviates from this requirement, the tandem cell efficiency will suffer. In the 4T configuration, tandem devices are also influenced by the spectrum, albeit to a much smaller extent. For tandem solar cells intended for 1-Sun applications, the low-irradiance loss might also be a concern, since the sub-cells divide the incoming irradiance and each cell operates at lower injection. According to the diode equations describing the solar cell I-V characteristics, the voltage output of p-n junction solar cells decreases logarithmically with decreasing light intensity. However, the exact behaviour of solar cells under low-light conditions also depends on non-linear effects from additional charge carrier

recombination losses (i.e., lower carrier lifetime) under low injection levels, as well as the shunt resistance losses which become relatively more important with decreasing light intensity.

In this study, 2T and 4T GaAs/Si tandem solar cell behaviour under various spectra and light intensities is studied via the device simulation method established in the previous sections. The relevant illumination conditions which tandem solar cells may experience under outdoor conditions were treated in Chapter 3. Tandem cell outputs under the characteristic set of spectra (sorted into different APE categories) scaled to different intensities were obtained. Their efficiencies as a function of APE value and intensity in Singapore are shown in Figure 4.3.1. For a given APE, the efficiency varies logarithmically with the intensity level, as expected from the diode equation. In comparison, the magnitude of variation of efficiency due to changing APE values can be more significant. For 2T tandems, extreme spectra with high APE result in a larger drop in efficiency than low light intensities. 4T tandems also suffer from spectral variations, but to a much smaller extent due to the absence of the current matching requirement. For the 4T configuration, a general rule is: the higher the APE, the lower the tandem cell efficiency. This is because the bottom cell receives a much smaller portion of the available irradiance under a blue-rich spectrum. It should also be noted that the more blue-rich the spectrum is, the smaller the total current will be for a given light intensity. As a result,  $J_{sc}$  of the bottom cell decreases significantly, while  $V_{oc}$  and FF decrease as well. This is not compensated by the marginal increase of the efficiency of the top cell. Therefore, it can be said that the major effect of changing illumination conditions is in current generation in the two sub-cells, especially the Si

bottom cell, due to changes in spectral composition. This makes photon management for the bottom cell a very important topic in the design of high-efficiency GaAs/Si tandem cells.

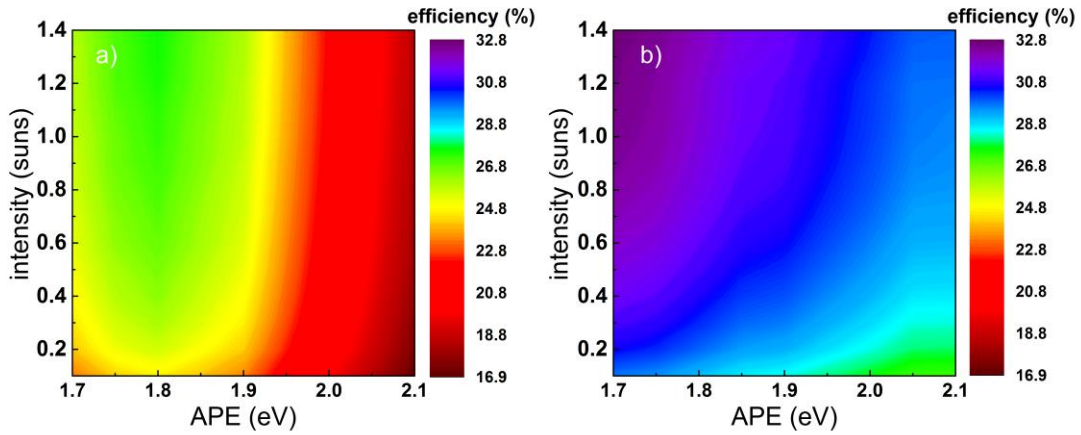


Figure 4.3.1: Simulated tandem solar cell efficiencies for (a) a 2T and (b) a 4T configuration under different spectral compositions (represented by the APE in eV) and light intensities (in suns). The calculated efficiencies range from 17% to 28% for 2T tandem cells and from 27% to 33% for 4T tandem cells.

The behaviour of other tandem cell configurations, and under operating conditions of other locations, may vary slightly compared with the results of Figure 4.3.1, whereby the exact behaviour will depend on the bandgaps of the sub-cells, the exact device configuration of the tandem solar cell, and the exact spectral composition. Efficiency maps similar to Figure 4.3.1 for other tandem configurations will be calculated in Chapter 6 in the context of energy yield calculations.



### 4.3.2. Temperature coefficients of tandem solar cells

The current, voltage and fill factor of a solar cell change with changing cell temperature, and generally lead to a decrease of the PV efficiency with increasing cell temperature. This is mainly a result of increasing free carrier concentrations with increasing temperature [20, 21, 130]. For III-V solar cells and Si solar cells, at ambient temperatures, the relative change in PV efficiency scales approximately linearly with temperature.

The tandem solar cell behaviour at elevated temperatures (relative to STC) can in principle be simulated by PC1D as well. However, the PC1D models used here are found to be inaccurate in predicting the temperature dependence of the III-V sub-cells, most probably due to an inadequacy in handling the interface property and band structures adequately across heterojunctions. Therefore, theoretical temperature coefficients (TC) of the sub-cell materials are used instead to estimate the sub-cell outputs under different temperatures. The temperature coefficients used in this study are listed in Table 4.3.1.

Table 4.3.1: Temperature coefficients used in this study [20, 130]. The temperature coefficients for stand-alone InGaP solar cells are less well known, so the same value as for GaAs were assumed. The temperature dependence of the currents is small and thus was neglected.

	Si	GaAs	InGaP
$dV_{oc}/dT$ (mV/K)	-2.20	-1.90	-1.90
$dFF/dT$ (K <sup>-1</sup> )	-0.13	-0.08	-0.08
$d\eta/dT$ (rel%/K)	-0.45	-0.20	-0.20

Using the temperature coefficients for the sub-cells, the outputs of the tandem solar cells are modified accordingly. The final 1-Sun tandem cell efficiencies under various cell temperatures are then obtained, from which the temperature coefficients of the efficiencies of the tandem solar cells are extracted. The results are listed in Table 4.3.2. They show that tandem solar cells tend to have lower temperature coefficients than single-junction Si solar cells, which is consistent with the findings for III-V concentrator solar cells [131, 132]. In fact, the TCs of tandem cells are closer to that of single-junction GaAs solar cells. This is expected since a significant portion of the power conversion happens in higher bandgap III-V materials, which tend to have smaller temperature coefficients [20]. Therefore, the use of a III-V top cell improves the overall temperature performance of tandem solar cells having a c-Si bottom cell.

Table 4.3.2: Calculated efficiency temperature coefficients of single-junction and tandem solar cells considered in the energy yield calculations. The TCs for SJ Si and SJ GaAs solar cells were obtained from PC1D simulations and are slightly different from the theoretical values shown in Table 2.

	Si SJ	GaAs SJ	GaAs/Si 2T	GaAs/Si 4T	InGaP/Si 2T	InGaP/Si 4T	InGaP/GaAs/Si 2T	GaAs/GaAs/Si 2T
Efficiency TC (rel%/K)	-0.478	-0.265	-0.376	-0.300	-0.339	-0.300	-0.336	-0.354

### 4.3.3. Operating temperatures

Under outdoor operation, the temperature of solar cells depends both on the irradiance level, the ambient temperature, wind speed, and the heat transfer characteristics of the encapsulating modules as well as mounting environment. This can be

modelled by a simple energy balance, where absorbed energy from solar irradiation ( $G_T$ ) is either extracted as electrical energy, or dissipated as heat [104]:

$$\alpha G_T = \eta G_T + U_L(T_c - T_a) \quad (\text{Eq. 4.1})$$

Here  $\alpha$  is the percentage of solar irradiation absorbed,  $\eta$  is the PV efficiency of the solar cell,  $U_L$  is the overall thermal loss coefficient, which lumps the effect of wind speed, encapsulation, and mounting environment, and  $T_c$  and  $T_a$  are the cell temperature and ambient temperature, respectively. The outdoor operating temperature of the solar cell can thus be predicted from solving the energy balance. However, accurate determination of module temperature is not easy. It depends on the detailed module encapsulation design, as well as many site specific factors. Roughly, outdoor cell temperatures relate to incoming irradiance by a simple linear model [103]:

$$T_c = T_a + k G_T \quad (\text{Eq. 4.2})$$

where  $k$  is known as the Ross coefficient. However, the Ross coefficient is influenced by both thermal losses as well as the cell efficiency, which is itself a function of cell temperature. To take this implicit relationship into account, a variety of implicit equations that relate  $T_c$ ,  $T_a$ ,  $G_T$  and  $\eta$  can be used instead [104]. In the present study we used the following equation [133]:

$$T_c = T_a + \frac{\alpha - \eta}{U_L} G_T \quad (\text{Eq. 4.3})$$

The ambient temperatures are measured at the same sites as the solar irradiances. The outdoor variations in ambient temperatures were discussed in Chapter 3. Together

with the intensity levels, it is then possible to predict the tandem solar cell temperature under outdoor conditions.

One potential advantage of using high-efficiency tandem solar cells instead of conventional single-junction Si or thin-film solar cells is that a lower operating temperature is expected. This is mainly due to the higher PV efficiency and, thus, reduced waste heat, but the lower temperature coefficient resulting from the use of a III-V top cell also helps. As an illustration, the outdoor operating temperatures of a higher-efficiency tandem solar cell are calculated using the implicit equation (Eq. 4.3), and compared with those of a lower-efficiency Si single-junction solar cell. 19% efficiency and an efficiency TC of -0.48 %/K are assumed for the Si solar cell, whereas 29% efficiency and an efficiency TC of -0.30 %/K are assumed for the tandem solar cell. The absorbed portion of the incoming irradiance is 0.76, which accounts for glass transmittance and the useful fraction of the solar spectrum. The ambient temperature is set as 28°C, to reflect the typical ambient air temperature in Singapore. The heat loss coefficient is assumed to be identical for both solar cells, and a value corresponding to a well-ventilated (i.e. air cooled) PV module [104] is chosen. The resulting operating temperatures for different irradiance levels are shown in Figure 4.3.2(a). The operating temperature is still linear with respect to the irradiance level, even after accounting for the temperature dependences of the cell efficiencies. An effective Ross coefficient  $k_{eff}$  can thus be extracted from the slope of the temperature versus irradiance straight line in Figure 4.3.2(a) for each tandem and SJ solar cells, and is shown in Table 4.3.3. It can be seen that, with the same heat loss coefficient, tandem solar cells have lower  $k_{eff}$  than SJ Si solar cells. The temperature difference between the two solar cell types, at

irradiance levels in the 800 to 1000 W/m<sup>2</sup> range, is around 3 to 4 °C, which is not negligible. Since most of the harvested energy per year comes from this irradiance band, the difference in cell temperatures is going to have a noticeable impact on the energy yield. Generally, the larger the PV efficiency difference, the larger the operating temperature difference will be at 1 Sun (Figure 4.3.2(b)).

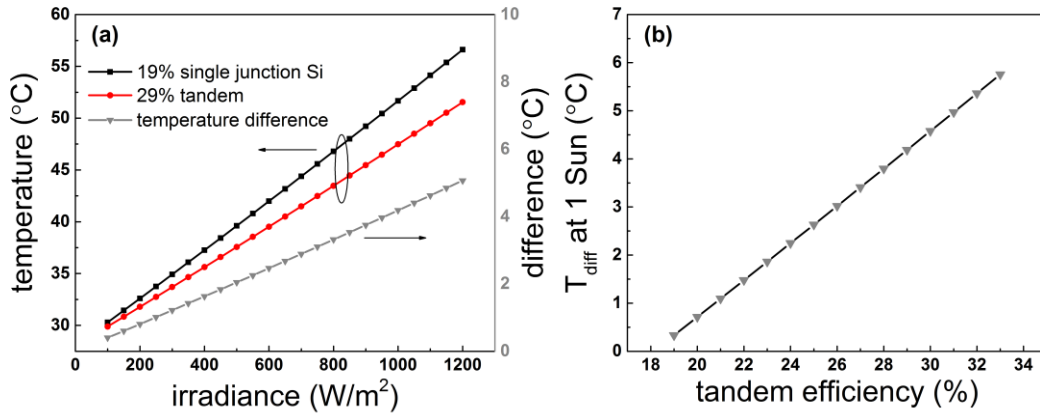


Figure 4.3.2: (a) The calculated operating temperature for a 19% efficient single-junction Si solar cell and for a 29% efficient double-junction tandem solar cell. The temperature difference (right axis) between the two types of solar cells, at 800 - 1000 W/m<sup>2</sup>, can be as much as 3 to 4 °C, which is significant. (b) The calculated operating temperature difference, at 1 Sun intensity, between a 19% Si solar cell and a tandem solar cell with varying efficiency.

Table 4.3.3: Calculated effective Ross coefficients of the investigated tandem solar cells.

	Si SJ	GaAs SJ	GaAs/Si 2T	GaAs/Si 4T	InGaP/Si 2T	InGaP/Si 4T	InGaP/GaAs/Si 2T	GaAs/GaAs/Si 2T
$k_{eff}$ (Km <sup>2</sup> /W)	0.0239	0.0200	0.0201	0.0185	0.0198	0.0197	0.0192	0.0189

#### 4.4. Chapter summary

In this chapter, a methodology for simulating tandem solar cells using optical calculations and PC1D device simulations was introduced. This simulation framework

is comparatively simple and fast, and has the flexibility to simulate tandem solar cell performance under STC as well as non-standard operating conditions. The simulated tandem solar cell efficiencies under various conditions will be used as input for the energy yield calculations in Chapters 5 and 6 of this thesis.

Several Si and III-V sub-cell models were considered. For the Si sub-cell, three models - representing a low-cost approach using UMG silicon feedstock material, an industrial standard, and a relatively high-efficiency concept - were used. For the GaAs sub-cell, two models - representing a baseline and an advanced cell - were used. For the InGaP sub-cell, only one model - representing a high-quality cell - was used. By simulating the STC efficiencies of double-junction tandem solar cells using different sub-cell combinations, it was found that some combinations are not beneficial, as the tandem efficiency was even lower than the efficiencies of the (stand-alone) sub-cells. Generally, this is the case when a lower-efficiency bottom cell is combined with a high-efficiency top cell. Therefore, for actual applications, it is important to combine sub-cells that are of high quality. Correspondingly, for the energy yield calculations in Chapter 6, only tandem models using the best sub-cells will be selected. Their architecture and simulated STC efficiencies were presented in this Chapter. In addition, the influence of a changing spectrum, light intensity level, and operating temperature on the efficiency of tandem cells was studied. Tandem solar cell efficiencies under various outdoor illumination conditions were obtained, which will be used in Chapter 6 for energy yield calculations. It was found that spectral variations indeed have a major impact on tandem solar cells, particularly for the 2-terminal configuration. An empirical model was used to estimate the outdoor operating temperatures of the

investigated single-junction solar cells and tandem solar cells. The calculations showed that III-V/Si tandem solar cells are expected to have a lower temperature coefficient than conventional single-junction Si solar cells, which is due to the use of III-V materials, and also lower operating temperatures in the field due to their higher PV efficiency.

## **Chapter 5. New methodology for energy yield calculation and outdoor loss analysis of tandem solar cells**

As discussed in Chapter 2, energy yield calculation for flat-plate tandem solar cell or modules is significantly different from that for single-junction or concentrated PV (CPV) multi-junction solar cells [134], and a systematic approach to assess their outdoor potential is not very established. In this chapter, a yield calculation methodology and an outdoor loss analysis method are presented that, in Chapter 6, will be used to analyse the outdoor performance of tandem solar cells. Also, some subtleties in the illumination conditions used for yield calculation are examined. In Section 5.1, the methodology for energy yield calculation is introduced. An efficient algorithm to compute energy yield is proposed. This algorithm makes use of device simulation and at the same time provides an easy way for including spectral data, thereby speeding up the calculations by limiting the number of device simulations needed. Subsequently, in Section 5.2, a framework to analyse and break down outdoor efficiency losses due to spectral changes, low irradiance and elevated solar cell temperatures is described. In Section 5.3, comparisons are made between different yield calculation methods using illumination condition inputs with different levels of detail and accuracy. Through this exercise, it is shown how subtleties in the temporal resolution and accuracy of illumination spectra affect the calculated energy yield in the analysis of outdoor performance of flat-plate tandem solar cells. Using simulated spectra, it is found that the conventional method of evaluating spectral effects, as used for concentrating PV



(CPV) devices, is not accurate enough for flat-plate tandem solar cells, as it can underestimate the performance ratio loss by as much as 60%.

## **5.1. Fast yield calculation algorithm**

Normally, yield assessment of PV systems simply uses historical average solar irradiance levels, temperature data and name-plate values of the used PV modules as inputs [3, 135]. The conventional ways of yield estimation is discussed in Section 2.3.3. Since no device simulation is involved, such yield calculation requires little computational effort. However, device simulation may be important for solar cells and modules under development, so as to obtain accurate device responses under various conditions for different device designs. Neglecting device simulation confines the calculations to linear effects. All non-linearity in cell performance is lost. The algorithm used in this work directly couples yield calculation with device simulation. Hence, this is one of the first efforts to include yield calculation at the early stage of solar cell design to, ultimately, optimize the solar cell from the outset towards Levelised Cost of Electricity (LCOE).

A straightforward and rigorous method would be to perform a computation for each time step for the whole time series, and then sum up the calculated energy outputs. In this study, the rigorous calculation was also performed using measured spectra and measured solar irradiance in high temporal resolution (one data point per 5 minutes). For example, the calculated energy yield as a function of time for a 2T GaAs/Si tandem cell is shown in Figure 5.1.1., for Singapore and Denver. This method is undoubtedly

the most accurate, and therefore will be taken as the benchmark for comparison in assessing the proposed fast algorithm. The calculated yield as a function of time also provides useful information on the real-time output of tandem solar cells, and how the output relates to the weather condition or illumination condition at that time. This information may be important for power grid management. However, carrying out device simulation for a long time series requires the processing of a huge number of data points and thus is time consuming and computationally intensive. This is especially true if an elaborate device model is employed. It is also limited in practice due to the extensive use of measured spectral data, which are not available for most locations.

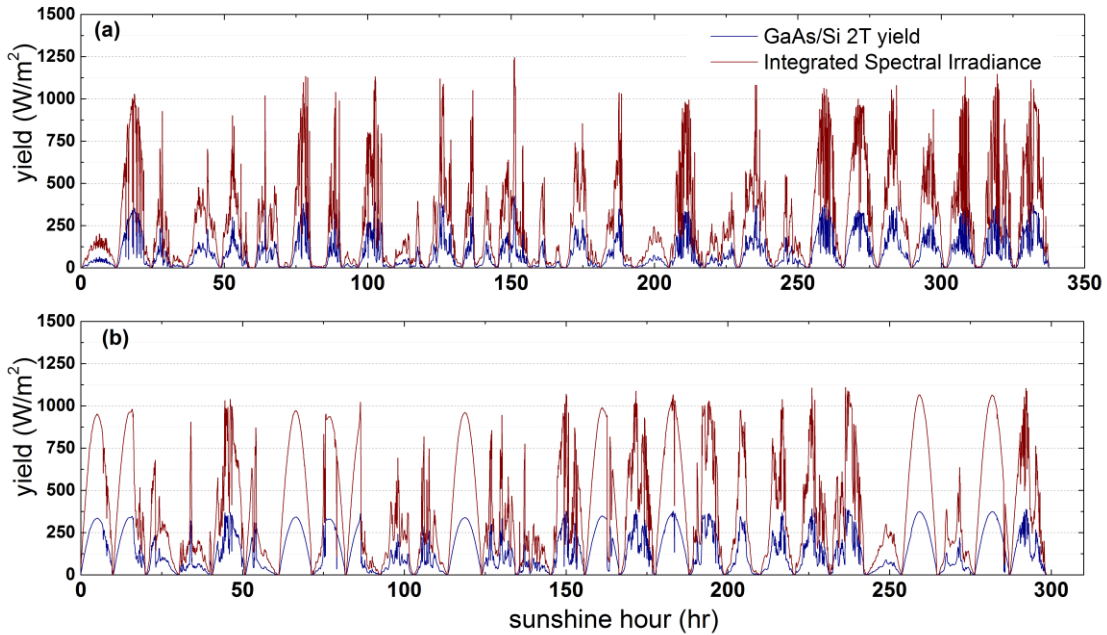


Figure 5.1.1: Time series of the calculated energy yield (blue line) of a 2-terminal GaAs/Si tandem solar cell during Feb 2013 in (a) Singapore and (b) Denver. The available solar irradiance is represented by the brown line. It can be seen that the cloudy nature of Singapore's weather results in significantly more fluctuations in the energy yield compared to that of Denver. The integration time for the energy yield is 5 minutes.

One drawback of this method is that long computation time may be required if elaborate device simulation is involved. As an alternative, the proposed fast algorithm makes use of the characteristic set of spectrum and distribution map of illumination conditions as described in Chapter 3. This distribution map describes the time duration  $t(APE, I)$  during which a condition with a certain  $APE$  and intensity  $I$  occurs, and can be seen as a fingerprint of the illumination conditions in a given location. Then, an efficiency map  $\eta(APE, I)$  as a function of  $APE$  and intensity is obtained by performing device simulations using the characteristic set of spectra (scaled to different intensities) as input. The device models used in this work were explained in Chapter 4. An IV curve, and thus a power output, is calculated using PC1D model with each input spectrum of each intensity level. In fact, the device models can be as elaborate as required (such as a Sentaurus TCAD model for the tandem device), as only a limited number of calculations will be required to generate the efficiency map. Then the efficiency map is corrected by the cell temperature that is prevalent under each illumination condition set to obtain the temperature corrected efficiency  $\eta_{T(APE, I)}$  of the solar cell. In this thesis the correction of temperature effect are done using temperature coefficients, but in principle device output under various temperatures can be directly simulated. More details on the study of the temperature effect will be given in Chapter 6. By combining the distribution map and the efficiency map, the energy output of a unit-area solar cell (referred to as energy yield in this work) in a given time period can be calculated:

$$energy\ yield = \sum_{i=1}^{i=N} \sum_{j=1}^{j=M} \eta_{T(APE_j, I_i)} \times I_i \times t(APE_j, I_i) \quad (\text{Eq. 5.1})$$

The energy yield as defined here has a unit of kWh/m<sup>2</sup>/time. The harvesting efficiency, defined as the ratio between the total electric energy generated and the total solar energy received during the same time period, is then obtained:

$$\eta_{har} = \text{energy yield} / \sum_{i=1}^N \sum_{j=1}^M I_i \times t(APE_j, I_i) \quad (\text{Eq. 5.2})$$

This unit-less value is indicative of the true PV efficiency of a solar cell under specific operating conditions. The loss in harvesting efficiency from the STC efficiency can be translated to an effective performance ratio drop of a PV system (see Section 5.2). The harvesting efficiency is a better measure of cell performance than the energy yield when it comes to rating, as the yield will vary with the amount of solar irradiance, which is the most important source of uncertainty in yield predictions (good and bad solar years). The overall flow of the algorithm, as explained above, is summarized and shown in Figure 5.1.2.

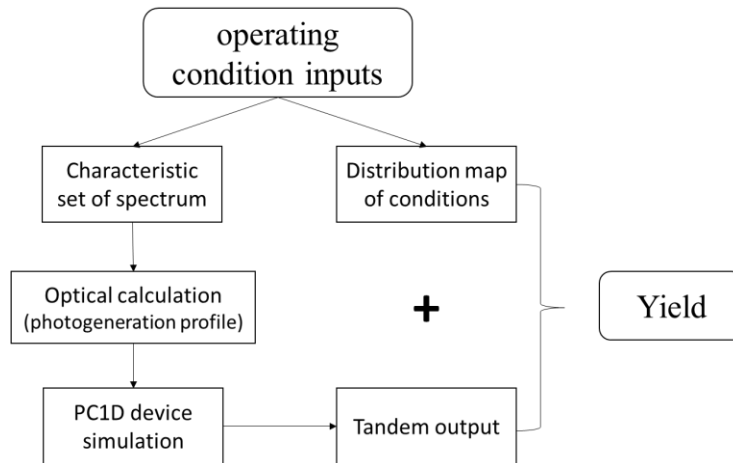


Figure 5.1.2: Schematic flow of the algorithm used in calculating energy yield for tandem solar cells.

The results calculated with this fast algorithm deviate by less than 5% from the results obtained from the rigorous calculation. This is considered accurate enough for the purpose of investigating outdoor loss characteristics of tandem solar cells in this thesis. As the distribution map can be prepared for any time period, this algorithm can be used to calculate both short-term and long-term energy yields. However, similar to the rigorous simulation, this algorithm suffers from the potential lack of realistic spectral data. Nonetheless, the uniqueness and time invariance of the characteristic set of spectra in principle enables wide applications, once it has been obtained for the location of interest. It is well possible to generate the set from a more elaborate radiative transfer modelling that includes cloud coverage [136, 137]. As an alternative to using historically measured data sets, statistical time series forecasting can also be employed to predict movements or distribution of APE and irradiance level.

## **5.2. Theories and framework for outdoor loss analysis**

### **5.2.1. Quantification of outdoor losses**

As discussed in Chapter 2, when solar cells are integrated into systems and are operated under outdoor conditions, they will experience several outdoor losses. The losses come from changing illumination conditions, module temperature, soiling, shading, as well as from various system components.

One important parameter describing the reduced outdoor performance of PV systems relative to their rated capacity at STC is the ‘performance ratio’ (PR) [58, 60]. The performance ratio is commonly defined in relation to the specific energy yield. It

should be noted that the term energy yield (or yield) as used in this thesis is slightly different from the same terminology used in the context of PV systems. In PV systems, “energy yield” commonly refers to the specific final yield ( $Y_f$ ) in  $kWh/kW_p$ . This is simply the annual DC energy produced per installed system capacity in  $kW_p$ . Another useful term is the reference yield ( $Y_r$ ), which is the available incoming solar irradiation (insolation), commonly denoted by the number of peak sunhours per year in the array plane, giving the reference yield the unit of hours. The performance ratio of a system is then given by the ratio of final yield and reference yield:

$$PR = \frac{Y_f}{Y_r} \quad (\text{Eq. 5.3})$$

This unitless quantity is a measure of actual system performance relative to the manufacturers’ nameplate ratings at STC. In fact, both final yield and performance ratio are closely related to, and convertible to, harvesting efficiency and energy yield as defined in this thesis. The final yield is related to yield, harvesting efficiency ( $\eta_{har}$ ), efficiency under standard testing condition ( $\eta_{STC}$ ) and PR by:

$$Y_f = \frac{\text{yield in kWh}}{\text{capacity nameplate rating in kW}_p} = \frac{\eta_{har} \times Y_r \times 1kWh}{\eta_{STC} \times 1kW_p} = PR \times Y_r \text{ (kWh/kW}_p\text{)} \quad (\text{Eq. 5.4})$$

Therefore, performance ratio is related to harvesting efficiency by:

$$PR = \frac{\eta_{har}}{\eta_{STC}} \quad (\text{Eq. 5.5})$$

The yield and harvesting efficiency investigated in this thesis are mainly related to the performance of solar cells, but not yet PV systems. The losses at the cell level

constitute the first component of the PR drop. In PV systems, other losses (such as inverter losses and cabling losses) must be added to obtain the final PR. In this thesis we have also made the simplification by equating the solar cell's STC efficiency to the PV system's rated efficiency.

In the analysis of outdoor losses, or sometimes gains, one can simply calculate the performance ratio drops, or equivalently harvesting efficiency drops, that are related to spectral effect, low irradiance effect, temperature effect, reflections, soiling, and other system related effects. In this work only the first three effects are considered for flat-plate tandem solar cells, since the other effects are expected to be similar to conventional single-junction solar cells.

### **5.2.2. Methodology for breaking down outdoor losses**

A proposed procedure for breaking down harvesting efficiency losses due to individual effects is shown in Figure 5.2.1. Several yield calculations are performed in sequence using different inputs of conditions. The input conditions change from STC to real outdoor conditions by changing one condition at a time. The resulting harvesting efficiency then contains the loss or gain resulting from that single condition deviating from the previous condition. By comparing the differences between harvesting efficiencies of two adjacent steps, one can obtain spectral loss/gain, low irradiance loss, and temperature loss, respectively. This can be easily done with the fast algorithm. Usually, the sequence in which these losses are calculated is not important. However, for tandem solar cells, spectral loss/gain should always be calculated before the low-

irradiance loss. This is because spectral shifts have a large impact on the injection level of all sub-cells. If the low-irradiance effect is calculated first, the subsequent calculation of the spectral effect would have included some additional intensity effects, since the intensity dependence of the solar cell efficiency is highly non-linear at lower injection levels.

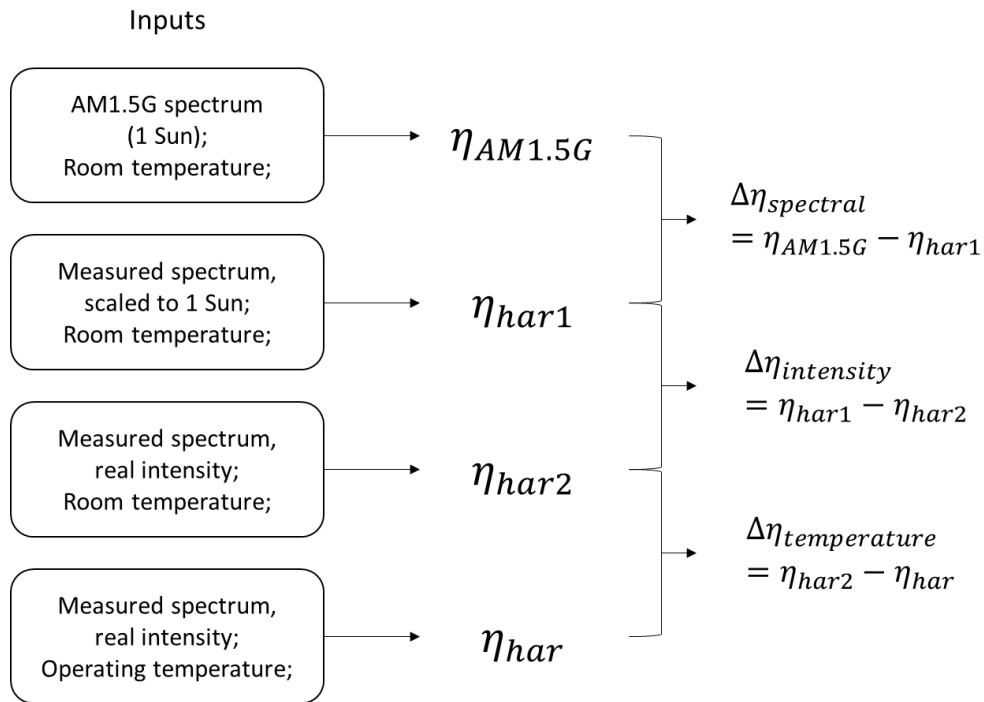


Figure 5.2.1: Procedure for performing the outdoor loss analysis.

### 5.3. Impact of input illumination conditions

#### 5.3.1. Sources of input illumination conditions

In energy yield calculations, the input illumination conditions, including irradiance levels and spectral composition, constitute a major part of the input outdoor conditions. Hence, they are expected to have a large impact on the final energy yield



result. The input illumination conditions need to represent the actual outdoor illumination conditions as accurately as possible. Depending on the availability and quality, the illumination data used as input can differ in both temporal resolution and accuracy. High-quality ground based measurements can produce irradiance and spectrum data with high degree of accuracy, and with high temporal resolution, often to the level of one data point per minute [85, 90]. Satellite derived data usually are less accurate, and have lower temporal resolution [99, 138]. In particular, spectrum data are hard to measure directly by means of remote sensing, and ground measurements are only available for very few locations globally. Therefore, location specific solar spectra are often derived from simulation, using radiative transfer models with various atmospheric parameters as input. One common code to simulate solar spectra for PV applications and research is called ‘Simple Model of the Atmospheric Radiative Transfer of Sunshine’, or SMARTS [84], developed by the National Renewable Energy Laboratory (NREL) in the US. This code computes clear sky spectral irradiance given the position of the sun and a set of specified atmospheric conditions.

Significant differences can exist between sets of illumination conditions obtained from different sources, whether measured or simulated. When used as input to energy yield assessment, they produce different results. Even with the same source of data, the use of different temporal resolution also results in different accuracy and uncertainty of the calculated energy yield. The objective of this study is to quantify the differences that arise from different input illumination conditions.

In addition, energy yield can be calculated for a certain time period - for example a day, a month, or a year. Long-term yield, such as the annual yield, is usually

considered when overall energy generation or LCOE calculations are concerned. However, short-term energy yield is also important, for example for estimating the required PV system size and electricity storage capacity, in forecasting and assessing the impact on power grids, as well as in monitoring system output and fault detection [3]. Therefore, how to calculate the energy yield for different time periods with a firm accuracy is a relevant question.

### **5.3.2. Calculation set up**

In this study, several ways of computing the energy yield for a 2-terminal GaAs/Si and a 2-terminal InGaP/Si tandem solar cell are compared, using different illumination inputs obtained in Denver and tropical Singapore. Different temporal resolutions of one data point per 30 minutes, 1 hour and 2 hours are used to generate distribution maps of a day, a week, and a month. In addition to measured data, SMARTS simulated spectra, and SMARTS simulated spectra scaled to measured intensity levels are also used as input. Therefore, energy yields, and thus the harvesting efficiency loss from STC efficiency, corresponding to inputs with different levels of detail are obtained. The harvesting efficiency loss, which is equivalent to the PR drop from spectral and irradiance effects, rather than absolute yield, is taken as the metric for evaluating outdoor performance. This is because the absolute amount of yield depends primarily on the input solar irradiance amount and absolute cell efficiency, which is less helpful in accurately revealing the subtle outdoor performance difference between different solar cell technologies.

The list of the different calculation methods used is as follows:

- Method A using illumination inputs of one measured spectrum per 30 minutes (abbreviated as “mea. 30 min”);
- Method B using illumination inputs of one measured spectrum per hour (abbreviated as “mea. 1 hr”);
- Method C using illumination inputs of one measured spectrum per 2 hours (abbreviated as “mea. 2 hr”);
- Method D using one SMARTS simulated spectrum per hour, but scaled to actual intensity (abbreviated as “sim. + mea.”);
- Method E using one SMARTS simulated spectrum per hour (abbreviated as “sim. only”);

The results from these calculation methods, all computed with the proposed fast algorithm, are compared against the reference value obtained using the more rigorous full time series calculation. Their accuracy and variation for different time periods are studied. These methods use the same tandem solar cell efficiency map. Once the efficiency map is pre-processed, generating the distribution maps takes very little additional time since no device simulations are involved.

### **5.3.3. Effect of temporal resolution**

The distribution map can be prepared to represent the illumination condition within any time period. The more data points there are within this period, the closer the representation is to the actual distribution. To see the effect of temporal resolution on

energy yield calculation on a daily time scale, the yield for the first seven days of each month from Jan 2013 to Dec 2014 was calculated, forming a sample size of 168. The relative deviation of harvesting efficiency losses calculated using methods A to E from the reference values is obtained for each day. The distribution of daily deviations for methods A to E, calculated for 2-terminal GaAs/Si tandem cells in Singapore, is plotted as a box plot in Figure 5.3.1(a). The whiskers represent the 5 to 95 percentile. Generally, the coarser the time resolution, the greater is the spread in the amount of deviation. This implies higher uncertainty in the calculated yield. However, the accuracy in harvesting efficiency loss is less affected. For longer time scales of a week and a month, the distributions of deviations are calculated and plotted in Figure 5.3.1 (b) and (c). The sample sizes for the weekly and the monthly case are both 24. A similar trend as in the daily case is observed, but the amount of variation is significantly reduced. This means that the effect of rapid fluctuations in illumination condition is averaged out when a long time scale is considered. For monthly or annual yield calculations, the time resolution of 1 hour, as was often used in previous studies in the literature, is quite sufficient. High time resolution is needed mainly in calculating short-term energy production. As comparison, the same study is repeated for GaAs/Si tandem cells in Denver (Figure 5.3.2), and an InGaP/Si tandem cell in Singapore (Figure 5.3.3). Similar observations are obtained.

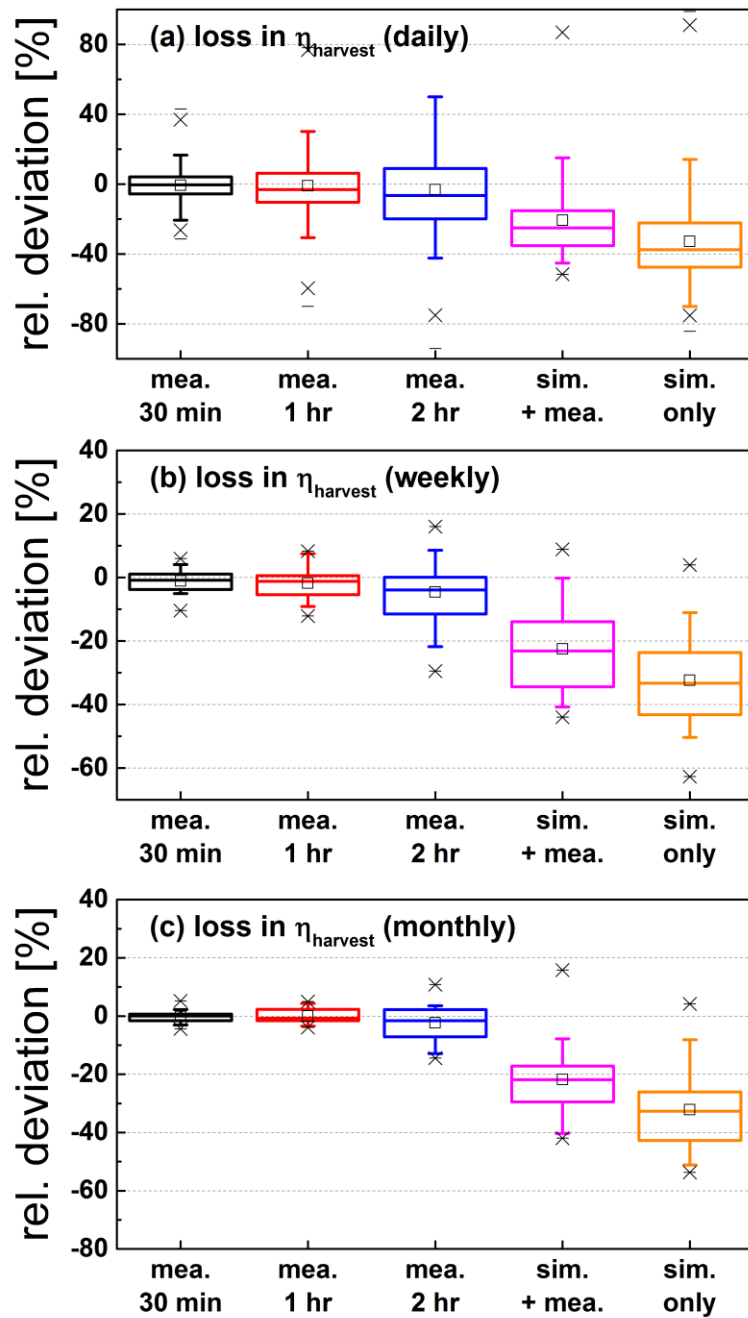


Figure 5.3.1: Box plot of the errors of (a) daily, (b) weekly and (c) monthly losses in harvesting efficiencies of a 2-terminal GaAs/Si tandem solar cell in Singapore. The losses in harvesting efficiencies are calculated from measured spectra with different time resolutions (30 min, 1 hour, 2 hours), as well as from SMARTS generated spectra and their intensity modified version. The errors are represented by the relative deviation from the reference values calculated using the full simulation.

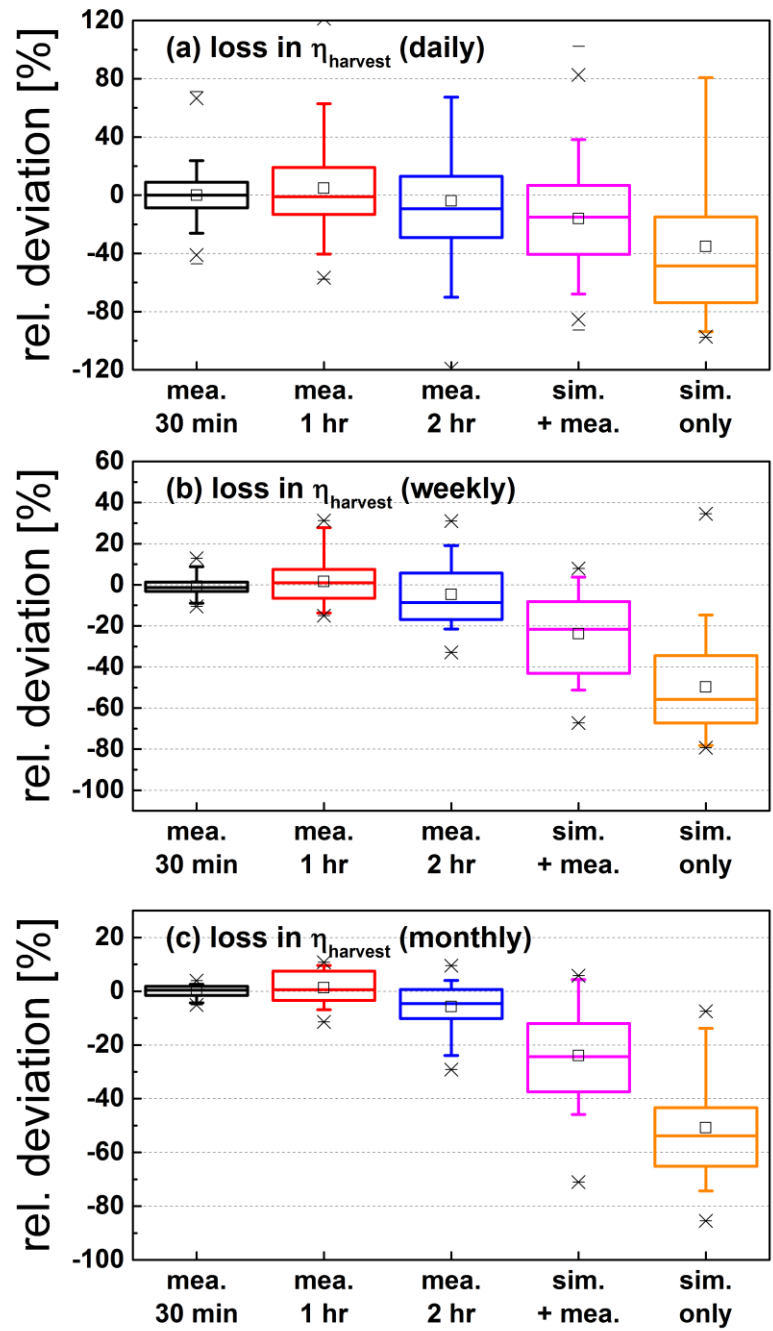


Figure 5.3.2: Box plot of the errors in the calculated (a) daily, (b) weekly and (c) monthly losses in harvesting efficiencies of a 2-terminal GaAs/Si tandem solar cell in Denver.

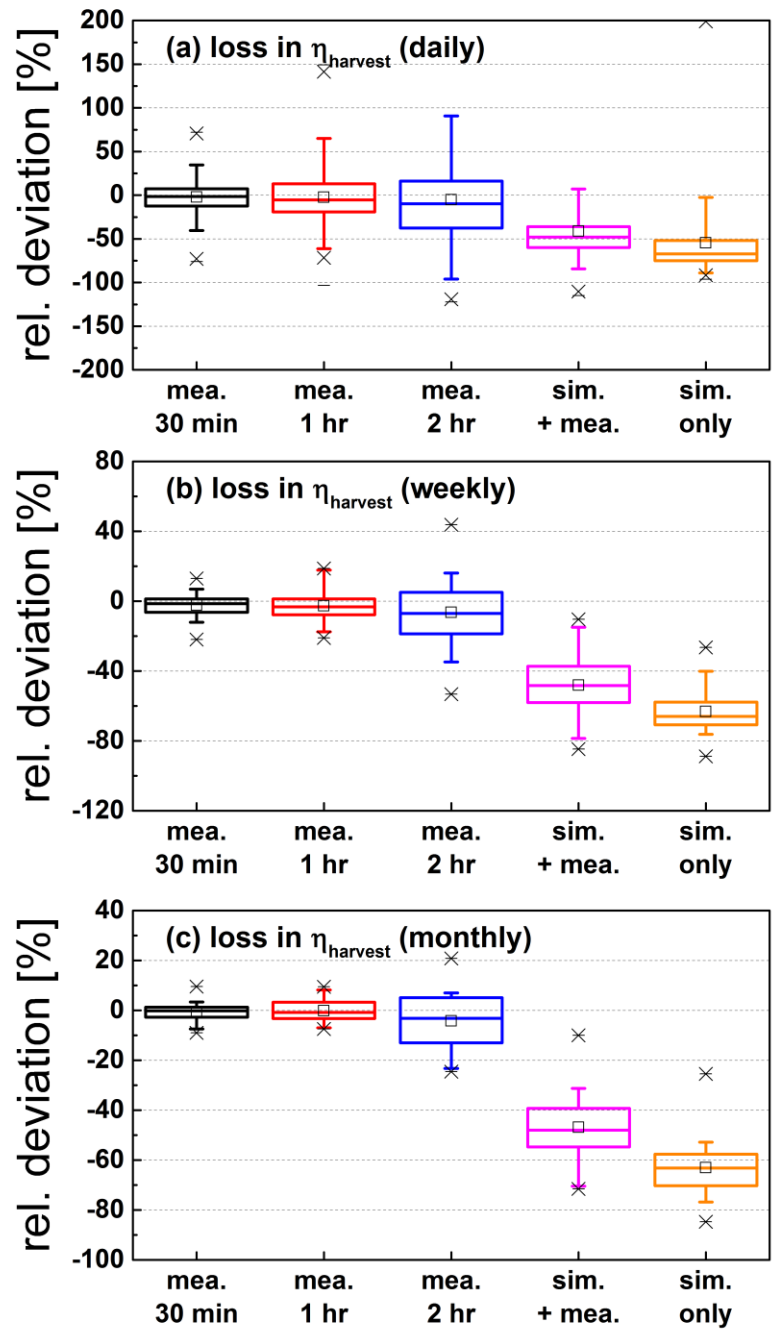


Figure 5.3.3: Box plot of the errors in the calculated (a) daily, (b) weekly and (c) monthly losses in harvesting efficiencies of a 2-terminal InGaP/Si tandem solar cell in Singapore.

#### **5.3.4. Effect of input spectrum**

The relative deviations of methods D and E from the reference value for the case of GaAs/Si in Singapore, GaAs/Si in Denver, and InGaP/Si in Singapore are also shown in Figure 5.3.1, Figure 5.3.2 and Figure 5.3.3, respectively. The calculation using the SMARTS generated spectra consistently underestimates the harvesting efficiency losses by 30% to as much as 60%, and shows much higher variation in all cases. Although the yearly average of the generated SMARTS spectra is found to fit the average of the measured spectra well, SMARTS spectra are still inadequate in representing the real-time illumination condition, in terms of both intensity and spectral composition. Time variation in the spectral composition of the simulated spectra is in fact smaller than in the measured spectra. There are two reasons for this. First, average atmospheric parameters are used, as real time values are hard to obtain. As a result, the effects of fluctuating atmospheric properties are not adequately reflected. Second, the SMARTS model is unable to capture the irradiance attenuation and spectrum change due to cloud coverage, which is very frequent in tropical Singapore. Even with real intensities, the deviation is still larger, suggesting that significant spectral losses are not accounted for. In short, the above observations highlight the importance of considering both realistic intensity and spectral composition in order to accurately predict outdoor performance of flat-plate PV systems, in contrast to conventional yield studies for concentrating PV systems.



## 5.4. Chapter summary

In this chapter, an energy yield calculation framework for flat-plate tandem solar cell PV modules was presented. A methodology to analyse outdoor losses was also introduced. The developed yield calculation and loss analysis methods will be used in Chapter 6 to study the outdoor performance of various III-V-on-Si tandem solar cells.

In particular, a fast and efficient energy yield computation algorithm was developed that is based on the use of a characteristic set of spectra and distribution of operating conditions, which are unique and constant for a given location. Both short-term as well as long-term energy yield calculations are possible with this method. The limited amount of calculations enables the use of elaborate device or PV system models. This is particularly relevant for solar cells or PV modules at the research and development stage, and is also important for capturing non-linear solar cell efficiency effects that are often neglected when evaluating energy yields. Both historical measured average and statistically forecasted time series or distributions can be used as inputs. Another feature of the developed method is the possibility to use the average photon energy (APE) concept directly in the energy yield calculations. Once the characteristic set of spectra is available for a certain location, the time series of APE values can potentially be measured economically by a simple sensor, thus enabling real-time energy yield calculations. Overall, this method provides a useful way to factor in spectrum, which has not been extensively considered in most energy yield assessments conducted so far. In addition, a framework for quantifying and breaking down the contributions from different outdoor loss mechanisms was outlined. This enables a coherent study of outdoor losses for tandem solar cells taking into account

several important and interlinked loss mechanisms at the same time, which was rarely done in the existing literature.

The impact of input illumination conditions was investigated. Different temporal resolutions of data points and different ways of obtaining input spectra (simulated with SMARTS or measured) were found to influence the accuracy and uncertainty of the calculated outdoor losses and energy yield values. For long-term yield calculations, detailed input is not vital. However, for short-term yield calculations, high temporal resolution of at least one input data per 30 minutes is needed if a low uncertainty is desired.

The conventional method of estimating energy yield, using SMARTS simulated spectra, was found to be inadequate for flat-plate tandem solar cells, because of the inability to account for the effects of cloud coverage and changing atmospheric conditions. Even after modifying the SMARTS generated spectra with measured intensity data, the predicted loss in harvesting efficiency was still underestimated by about 30% to 60%. Therefore, a better representation of the actual spectral composition is desired. Overall, there is still an advantage of using high time resolution measured data to accurately calculate the energy yield.

## **Chapter 6. Energy yield of 1-Sun tandem solar cells and implications on design rules**

Using the energy yield calculation framework established in Chapter 5, the energy yields for several Si based 1-Sun (flat-plate) tandem solar cells are evaluated in this chapter using solar irradiance data from Singapore and Denver. This chapter first presents the time resolved energy yield for a GaAs/Si tandem solar cell. Yield behaviour over the course of time is analysed and discussed. Then, the annual harvesting efficiencies and the breakdown of outdoor losses are studied for various III-V/Si tandem solar cells. The performance ratios attainable by these solar cells after considering spectral loss, low-irradiance loss and temperature loss are calculated and compared for Singapore and Denver. Finally, attempts are made to utilize these results to inform tandem solar cell design and optimization.

### **6.1. Time resolved energy yields for GaAs/Si tandem solar cells**

In this study full time series device simulation is carried out for a GaAs/Si tandem solar cell. The tandem configuration consists of the model of an advanced GaAs top cell and a PERC Si bottom cell, as introduced in Chapter 4. The solar irradiance and spectral data for illumination input were introduced in Chapter 3. The full time series of device output, namely time resolved energy yield, is obtained and analysed. This helps to show in detail how the yield and harvesting efficiency change with time, and

how rapidly changing illumination conditions at different moments influence the real-time solar cell output. This can be useful information for many applications, such as power grid management, or the designing of power autonomous devices [139].

### **6.1.1. Device structure and simulation setup**

The simulated device architectures are shown in Figure 6.1.1. Other than the standard 2-terminal (2T) and 4-terminal (4T) architecture, a 4T configuration with a top cell thinned to 215 nm (same as GaAs thickness in the standard 2T architecture) is also included, and is named 4T\_thinned. This configuration helps to analyse the extent of current mismatch losses in the 2T configuration. The measured solar irradiance data, device models and simulation routines were discussed in Chapters 3 and 4. Spectral data of Singapore as well as Denver in the year 2013 is used as illumination input. One data set per five minutes is used. For each data point, an optical calculation is performed using the transfer matrix method (TMM), and a depth-resolved photogeneration profile is obtained for each layer. Subsequently, the electrical characteristics of the tandem device are calculated. Repeating this procedure for every data point, the time-resolved power is obtained. The overall energy yield is obtained by integrating the time-resolved energy output.

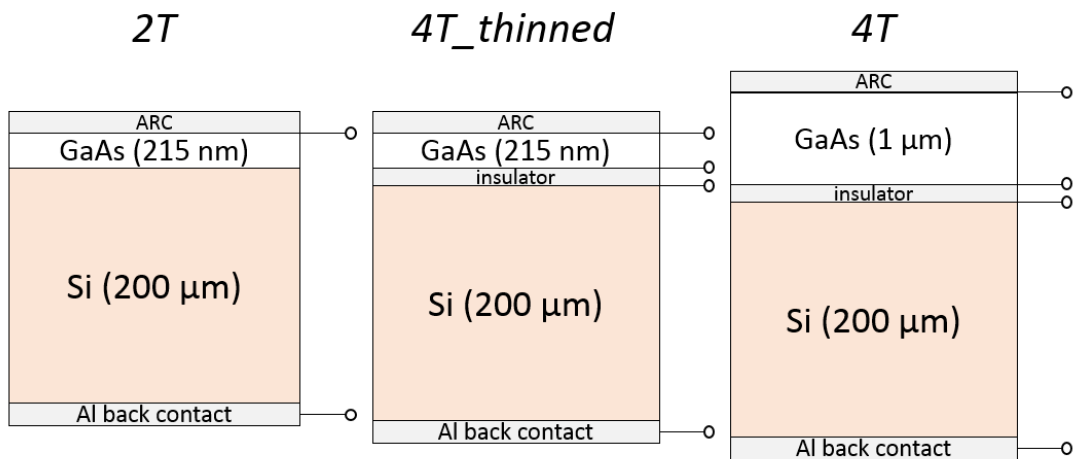


Figure 6.1.1: Schematics of the three simulated GaAs/Si tandem solar cells.

### 6.1.2. Time series of yield and discussion

As an illustration, the time series of energy yield for the two locations considered, together with the available solar irradiance, were shown in Chapter 5, also reproduced here in Figure 6.1.2 for convenience. As can be seen, fluctuations in solar power reaching the ground are very common in Singapore, both on sunny and overcast days, due to cloudiness in an equatorial climate. In comparison, clear days with a bell-shaped irradiance profile are more common in Denver. One typical sunny day with intermittent cloud coverage (day 2) and one very overcast day (day 10) in Singapore are highlighted in Figure 6.1.2. As will be shown later, tandem solar cell efficiencies during the two highlighted days differ significantly.

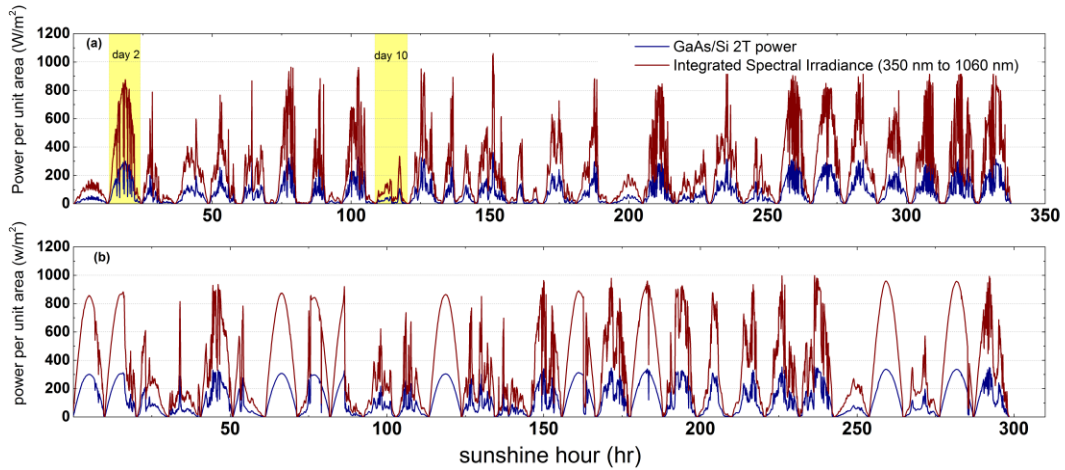


Figure 6.1.2: Integrated spectral irradiance and simulated  $2T$  GaAs/Si power as a function of sunshine hours for Sep 2013, in (a) Singapore and (b) Denver. Fluctuations in solar radiation are captured in fine detail. Two days of particular interest are highlighted for further comparison.

The daily amount of solar insolation available to the solar cell, i.e. the daily total of the integrated spectral irradiance (ISI), and the calculated daily energy yield of the three solar cell configurations for Singapore and Denver are shown in Figure 6.1.3 (a) and (b), respectively. In addition, the 4-terminal detailed balance limit output is also included. This output was calculated using detailed balance method (see Chapter 2), but assuming a realistic optical absorption for the given solar spectrum. This is taken as the highest yield potential for the given tandem architectures, and is used as a benchmark for comparison.

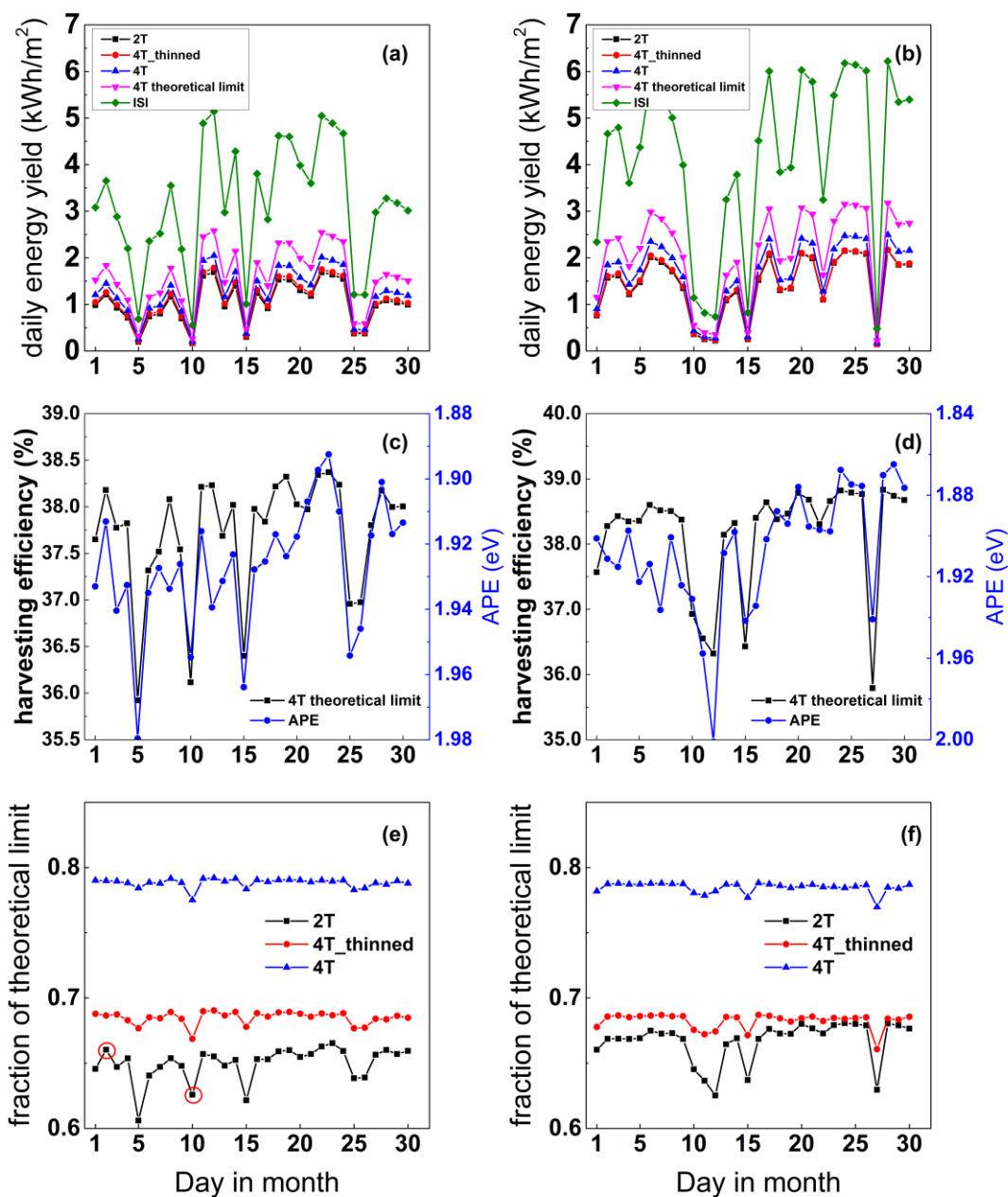


Figure 6.1.3: Simulated daily energy yield of the three investigated tandem solar cell configurations in (a) Singapore and (b) Denver, for September 2013. The integrated spectral irradiance (ISI) of the solar radiation and the theoretical output limit calculated using the detailed-balance method are also shown for comparison. The harvesting efficiency of the detailed-balance limit is shown in (c) for Singapore and (d) for Denver, together with the daily averaged average photon energy (APE) values. Taking the detailed-balance output as the benchmark, the performance of each configuration in (e) Singapore and (f) Denver is shown. The 2T configuration is significantly more sensitive to spectral variations, especially on days with low insolation. The two days of particular interest (days 2 and 10) for Singapore are circled in red in graph (e).

The average daily harvesting efficiency of a 4-terminal GaAs/Si tandem solar cell at its theoretical limit is shown in Figure 6.1.3 (c) for Singapore and (d) for Denver. As can be seen, the theoretical harvesting efficiency limit varies strongly over the course of the investigated month. The trend roughly follows the pattern of daily ISI. This is mainly due to the light intensity dependence of the cell voltage. The cell efficiency is lower at lower intensities, and thus a larger low-irradiance loss occurs. It can be observed that the trend of the harvesting efficiency also roughly agrees with the trend of the average daily photon energy (APE) values. The more blue-rich the spectrum (i.e., the higher the APE value), the lower the harvesting efficiency. However, this is inconsistent with the behaviour of 4T GaAs/Si tandem solar cells under varying spectra, as discussed in Chapter 4. Therefore, the trend match occurs entirely because the spectra of very overcast days tend to be blue-shifted, as discussed Chapter 3. It can thus be concluded that the impact of the light intensity is larger than that of the spectral composition for 4T GaAs/Si tandem cells. Note that no shunt resistance is included in the tandem models. The impact of light intensity may be even larger if the effects of shunt resistances are considered.

To compare the performance of the realistic devices with different configurations, their energy yields as a fraction of the theoretical limit are shown in Figure 6.1.3 (e) and (f) for Singapore and Denver, respectively. In terms of fraction of theoretical limit realized, the realistic device output stays relatively constant, but drops for days with very low insolation. However, for realistic 4-terminal tandem devices this variation is much smaller than the amount of variation in harvesting efficiency at the theoretical limits. This implies injection dependence for the recombination losses present in



realistic devices play a minor role compared to the light intensity dependence of the voltage. In contrast to the 4-terminal case, the calculated output of 2-terminal tandem solar cells fluctuates more. This is mainly due to their increased sensitivity to the spectrum as a result of current mismatch, as can be seen from the difference of the output of the 2T and 4T\_thinned configurations. The 2T output in Singapore is consistently lower than that in Denver, because of Singapore's bluer spectrum, which induces losses in the GaAs top cell, which was designed for operation under the AM1.5g spectrum. The 2T efficiency suffers disproportionately more during very overcast days, a result of the mentioned correlation between average spectral composition and daily insolation. As an illustration, the average spectra of day 2 and day 10 in Singapore are shown in Figure 6.1.4. The spectrum of day 10, which has low insolation, is significantly more blue-rich than that of day 2, causing a much more severe current mismatch. In short, the power output of days with low light intensity is affected over-proportionally because of the additional effect of a changed spectrum.

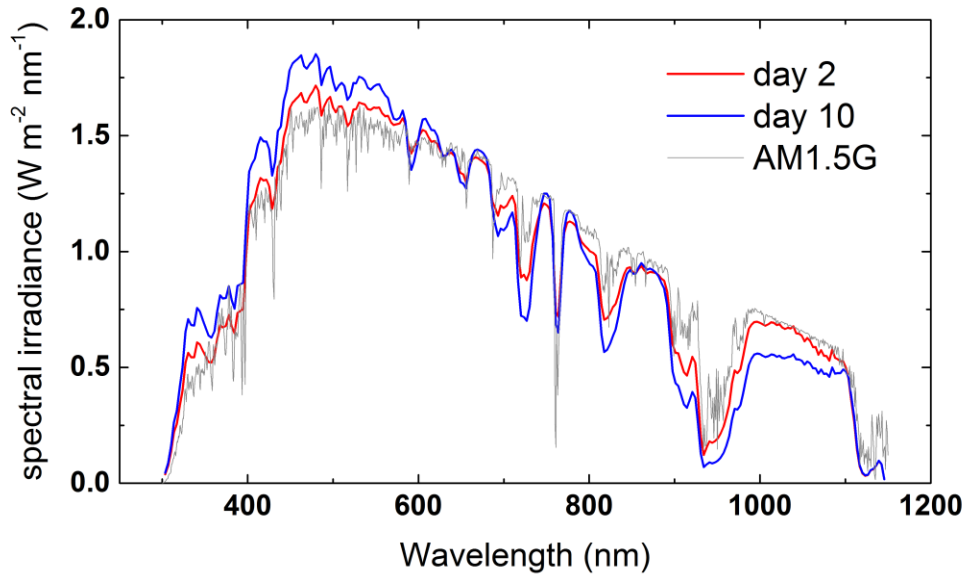


Figure 6.1.4: Comparison of average solar spectra in Singapore on day 2 and day 10 of Feb 2013, for the wavelength range 300 to 1050 nm. The spectrum of day 10 is significantly blue shifted, causing larger current mismatch for the 2T tandem cell configuration. The AM1.5G spectrum is also shown for comparison. All three spectra were normalized to the same integrated spectral irradiance (ISI) of  $761 \text{ W/m}^2$ , which corresponds to an intensity of  $1000 \text{ W/m}^2$  for the complete wavelength range (280 nm to 4000 nm).

In Figure 6.1.5, the calculated average daily energy yield of 2T and 4T GaAs/Si tandem solar cells over 12 months - from Feb 2013 to Jan 2014 - in Singapore and Denver are plotted. As can be seen, an energy yield of over  $1 \text{ kWh/m}^2$  can be expected per day at both locations. The daily average values fluctuate throughout the year, with no clear pattern for Singapore and some seasonal trends for Denver. On average, for both locations, the 4T output is more than 15% higher than the 2T output.

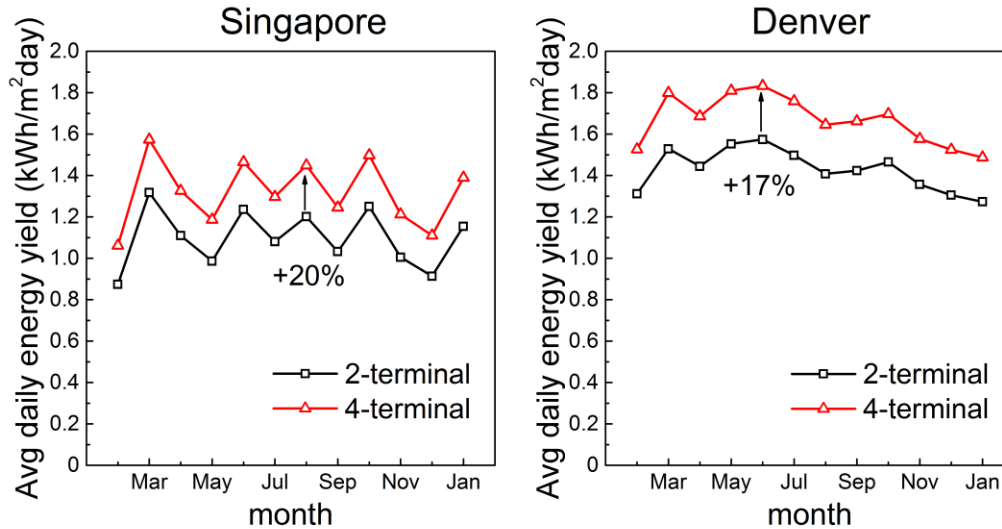


Figure 6.1.5: Simulated average daily energy yield of 2T and 4T GaAs/Si tandem solar cells over 12 months (from Feb 2013 to Jan 2014) at two locations (Singapore and Denver). On average, the 4T output is more than 15% higher than the 2T output.

### 6.1.3. The influence of photon recycling and luminescent coupling

As mentioned in Chapter 4, photon recycling effects may cause a non-negligible improvement to the efficiency in high-quality III-V solar cells, where radiative recombination is the dominant recombination mechanism. The re-emitted photons can also be transmitted to - and absorbed in - the Si bottom cell (“luminescent coupling”). When the spectrum is blue shifted, more e-h pairs are generated in the top cell(s) and thus more photons are emitted by them due to radiative recombination. If the luminescent coupling efficiency is high, the current in the Si bottom will consequently drop less compared to the case where no photon recycling is present. As a result, the current mismatch loss will be mitigated. The yield calculations presented in this thesis do not consider this effect, as otherwise the device simulations would become too time consuming. If this effect is included, the energy yield of the tandem cells would be slightly higher. To give an example of the relative importance of the photon recycling

effect on the calculated energy yield results, the yield for a 2T GaAs/Si was calculated by taking photon recycling into account. The simulations were performed for the month of August 2013, for two locations (Singapore and Denver). As the impact of photon recycling depends on the spectral composition, the ratio of the calculated energy output considering photon recycling ( $E_{\text{with PR}}$ ), and without photon recycling ( $E_{\text{w/o PR}}$ ) is plotted against the APE value of the spectrum for all data points (Figure 6.1.6). As expected, the more blue-rich the spectrum, the greater the photon recycling effect is. After integrating the energy output, the total yield increases by around 1% after including photon recycling in the calculation.

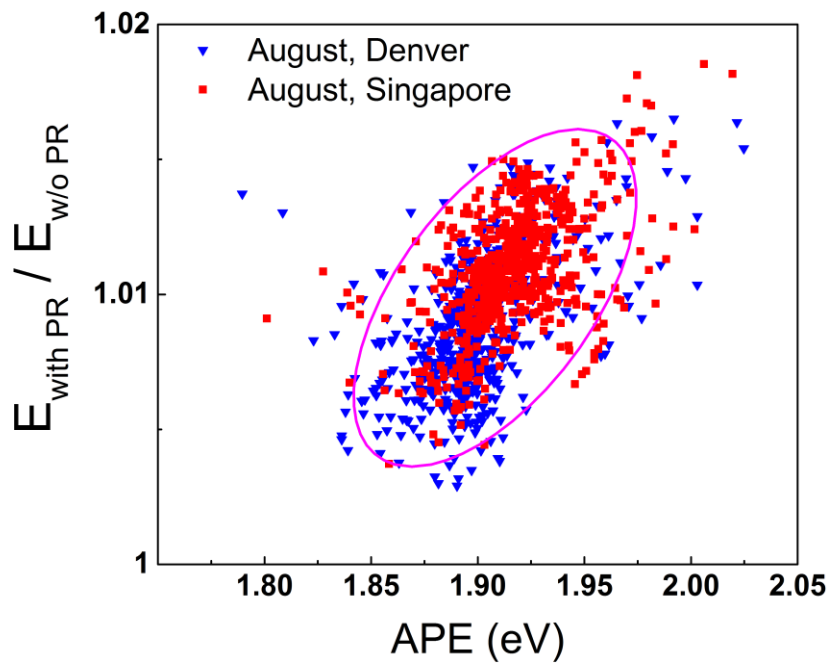


Figure 6.1.6: The ratio of the calculated energy output considering photon recycling ( $E_{\text{with PR}}$ ), and without photon recycling ( $E_{\text{w/o PR}}$ ) versus the APE of the input spectrum, in August 2013. The higher the APE values are, the greater the photon recycling effect is. Overall, the total energy yield increases by around 1% after including photon recycling in the calculation.

## **6.2. Annual harvesting efficiency and outdoor loss analysis**

Detailed energy generation patterns are valuable information, but for overall energy generation and economics, the long-term energy yield is the most important parameter. In this section, the annual yield potentials of various III-V/Si tandems are determined, calculated using the proposed fast algorithm. Assessment of the long-term yield potential provides insights into the competitiveness and viability of these tandem cell technologies. In addition, it is useful to break down the contributions from different mechanisms to the overall outdoor efficiency losses. This section first summarizes the calculated outdoor harvesting efficiencies and losses for the investigated tandem cells, followed by a discussion of the implications on the performance ratios of PV systems that employ these solar cells. The yearly variation of the harvesting efficiency is also briefly discussed.

### **6.2.1. Summary of annual harvesting efficiencies and outdoor losses**

The harvesting efficiencies for several III-V/Si tandem solar cells optimized for STC conditions, a single-junction (SJ) GaAs cell, and a SJ Si cell operating in Singapore as well as Denver are calculated for several years. The outdoor losses are broken down into contributions from spectral variations, low irradiance, and elevated temperatures. The results for Singapore and Denver for the year 2014 are shown in Figure 6.2.1 and Figure 6.2.2, respectively. The STC efficiency of each solar cell is indicated beside the starting point of each “loss waterfall” diagram. The final harvesting efficiency after inclusion of all three loss mechanisms is indicated at the bottom of the

waterfall by bold text. It can be seen that 2-terminal devices, especially triple-junction devices, suffer severely from spectral variations in Singapore, due to the blue-shifted spectrum. The temperature related loss in Singapore is also significant. As a result, 2T GaAs/Si and 2T InGaP/GaAs/Si have harvesting efficiencies that are lower than that of a SJ GaAs cell, despite having a higher STC efficiency. With the cell models used in this study, only the 4T GaAs/Si cell and the 2T GaAs/GaAs/Si cell surpass the final harvesting efficiency of the SJ GaAs cell in Singapore. This highlights the challenge of realizing improved flat-plate PV module efficiencies using tandem solar cells under Singapore’s operating conditions.

In comparison, the losses due to spectral variations and the elevated cell temperature are much smaller in Denver, where the 2T InGaP/GaAs/Si achieves a higher harvesting efficiency than a state-of-the-art single-junction GaAs solar cell. With better InGaP and Si sub-cells, a 4T InGaP/Si tandem cell can reach nearly 30% STC efficiency [56], and thus is also expected to beat the SJ GaAs cell.

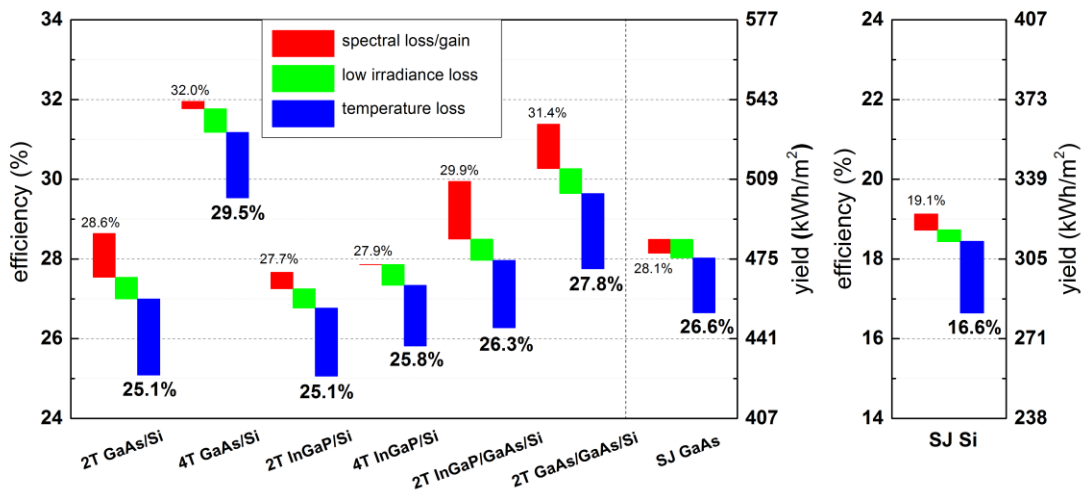


Figure 6.2.1: The breakdown of outdoor losses of Si based tandem solar cells with various III-V top cells, for the year 2014 in Singapore. The loss breakdown for single-junction (SJ) GaAs and Si solar cells using the same device models is also included for comparison. The STC

efficiencies and the final harvesting efficiencies taking into account the three losses are indicated in the graph.

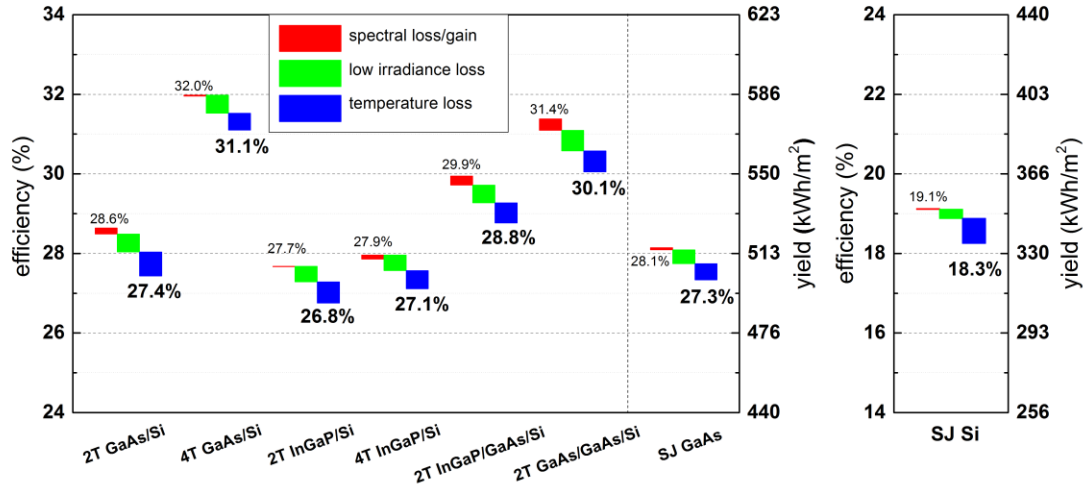


Figure 6.2.2: The breakdown of outdoor losses of Si based tandem solar cells with various III-V top cells, for year 2014 in Denver. The spectral loss and temperature loss are much lower than in the case of Singapore. Several of the investigated tandem cell structures achieve better harvesting efficiency than a high-quality single-junction GaAs solar cell.

Given that the models for InGaP and GaAs used in these calculations already represent high-quality III-V cells, there is limited room for improvement of the top cells. Further improvement of the harvesting efficiency of the tandem cell thus needs to come from a better bottom Si cell. The Si cell model used in this thesis represents an industrial PERC-type cell with approximately 20% STC efficiency. In addition, due to the assumption of planar front and rear surfaces, the long-wavelength region (1000 - 1150 nm) of the solar spectrum is not well utilized. Using a higher efficiency Si solar cell with good light trapping could thus be beneficial.

### **6.2.2. Implication on performance ratio**

As discussed in Chapter 5, the harvesting efficiency losses shown in Figure 6.2.1 and Figure 6.2.2 can be translated into PR losses. This is done by calculating the relative percentage of the respective losses to the STC efficiency. The PR loss here refers to intrinsic losses due to the solar cell's response to variations in the outdoor conditions, which would be part of the overall system PR loss. The PR losses, broken down into the three loss channels, and the resulting PR for the different solar cells in Singapore and Denver are shown in Figure 6.2.3 and Figure 6.2.4, respectively. It should be noted that the PR here only includes the effects from spectral variations, low irradiance, and cell temperature. The three loss mechanisms represent three important sources of performance ratio drops of PV systems due to the solar cells. Other factors such as soiling, reflection, shading, and losses within cabling or other system components are not considered in this thesis. These factors are expected to be similar for systems employing tandem solar cells and conventional Si solar cells. In Singapore, the spectral losses for 2-terminal tandem devices are generally severe, mostly due to systematic current mismatch losses, as the tandem device is optimized for the AM1.5G spectrum, which differs significantly from the actual conditions in Singapore. In contrast, spectral losses are generally insignificant in Denver, as the prevalent spectral composition in Denver is very close to AM1.5G. In general, 4T devices are not susceptible to spectral losses, even less so than a SJ Si solar cell. 4T InGaP/Si and SJ GaAs both experience some PV efficiency gain in Singapore, as higher-bandgap materials benefit from Singapore's blue-shifted spectrum.



The low-irradiance loss in Singapore is more severe than in Denver, due to more frequent cloud coverage and intensity fluctuations. In both locations, the low-irradiance losses for the tandems are slightly higher than single-junction cells, as the sub-cells divide incoming irradiance. Losses for the GaAs/Si and GaAs/GaAs/Si configurations are the highest, most probably due to the extremely thin GaAs cell used in the 2T double-junction or triple-junction case and the low light intensity seen by the Si cell in the 4T case. It should be noted that our device models at this stage may not be very accurate in capturing all low-injection effects, and no shunt resistance was assumed. However, this will not severely affect the energy yield results because low-irradiance conditions contribute little to the total annual energy generation.

Temperature related losses are the largest outdoor loss for all solar cells investigated, both in Singapore and in Denver. However, the temperature related losses are lower for III-V/Si tandems compared to conventional single-junction Si solar cells. Their temperature performance is in fact closer to that of a GaAs solar cell. In addition, 4T configurations investigated here have lower temperature loss than 2T devices, partly because more power conversion takes place in the III-V top cell.

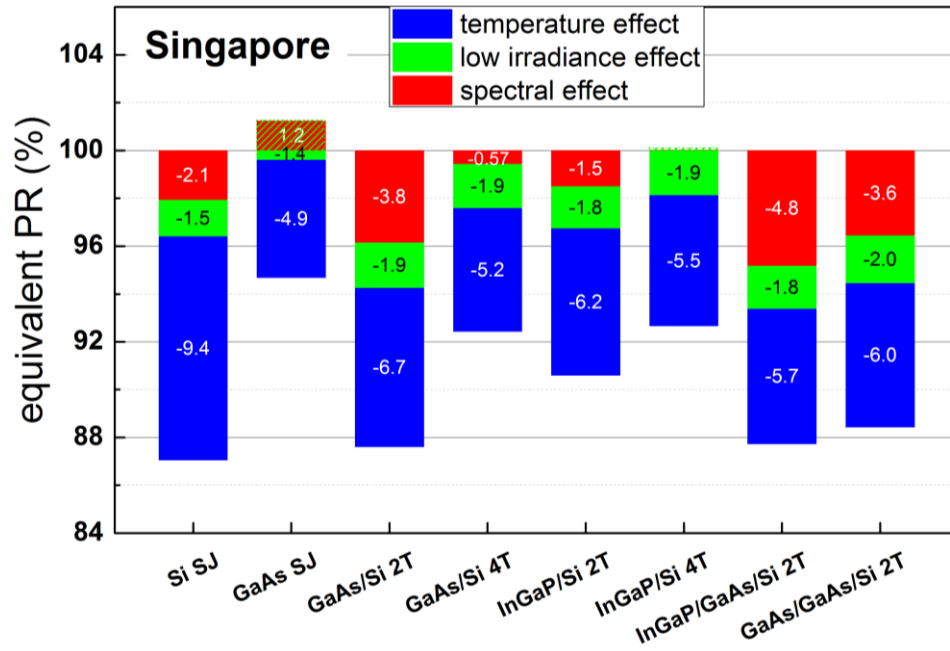


Figure 6.2.3: The predicted PR after taking into account the spectral effect, the low-irradiance effect, and the temperature effect for a single-junction Si and GaAs cell as well as several Si based tandem solar cells operating in Singapore. Single-junction GaAs and 4T InGaP/Si tandem solar cells experience a slight efficiency gain due to the blue-rich spectrum, which increases the PR to over 100%.

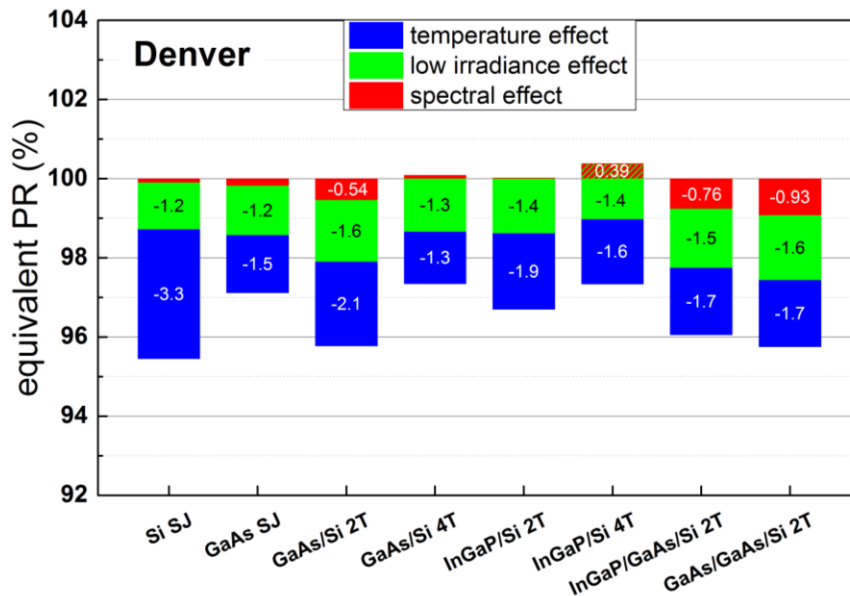


Figure 6.2.4: The predicted PR after taking into account the spectral effect, the low-irradiance effect, and the temperature effect for a single-junction Si and GaAs cell as well as several Si based tandem solar cells operating in Denver. The PR loss due to spectral effect and temperature effect are greatly reduced from Singapore's case. Low-irradiance loss is also slightly less.

Overall, the tandem solar cells can achieve PRs as good as those of a conventional single-junction Si solar cell, or even better for the 4T cases. 2T tandem solar cells indeed suffer more from spectral variations, but this loss is compensated by higher efficiencies and a better temperature tolerance. As will be seen in Section 6.3, it can also be partially mitigated by customization of the tandem design.

### **6.2.3. Variation over the years**

Operating conditions for solar cells vary from year to year (“good” and “bad” solar years). The yearly variations of spectrum, insolation and ambient temperature were described in Chapter 3. Consequently, the harvesting efficiencies and the outdoor loss characteristics fluctuate slightly from year to year. To estimate the degree of fluctuation, the annual harvesting efficiency of a 2T GaAs/Si tandem cell in Denver was calculated for 5 years, 2011 to 2015, see Figure 6.2.5. The harvesting efficiency without the temperature effect includes only the losses resulting from fluctuating illumination conditions, i.e., spectrum and intensity. The amount of variation over the years is around 0.1% absolute (or 0.4% relative). The variation after inclusion of the year-to-year temperature differences is larger, around 0.2% absolute (or 0.8% relative).

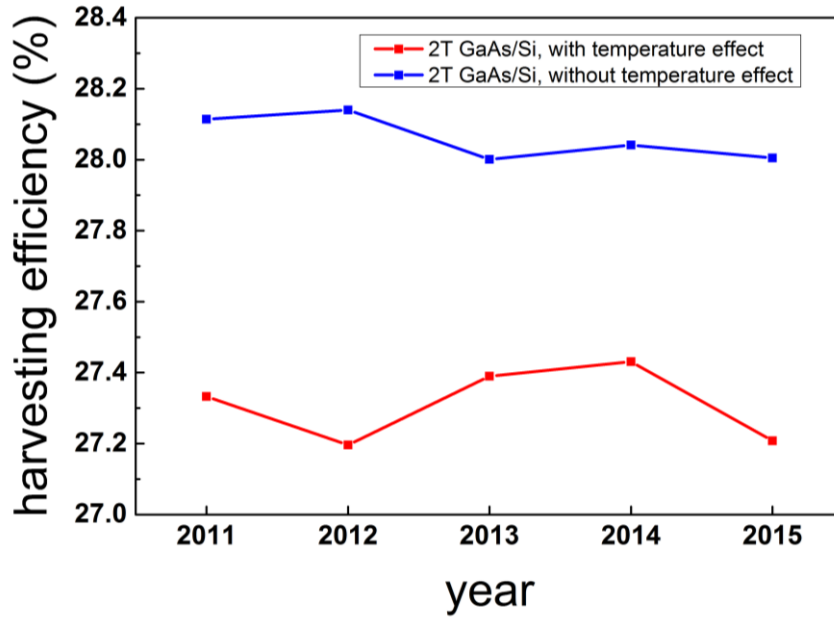


Figure 6.2.5: The annual harvesting efficiency of a 2T GaAs/Si tandem cell in Denver, calculated for five years from 2011 to 2015. The harvesting efficiencies considering only loss from fluctuating illumination conditions show a variation of around 0.1%, where harvesting efficiencies considering both illumination conditions and temperatures show a variation of around 0.2%.

### 6.3. Implications on design

Operating conditions vary for different locations. Calculations show that designing a tandem solar cell towards STC results in considerable current mismatch losses in Singapore. Therefore, it could be economically favourable to move from a “one size fits all” design to customization for local conditions. To see the effect of customization on the spectral loss, the top cell thicknesses for the 2T tandem solar cells were adjusted to achieve current matching under Singapore’s average spectrum. The harvesting efficiencies in Singapore in 2014 were then calculated for the customized designs. The results are shown in Table 6.3.1 and Figure 6.3.1. As can be seen from Table 6.3.1, the PR loss due to spectral effect becomes insignificant after the customization. However, this is partly because the rated efficiency under STC is

reduced for the customized design (see Figure 6.3.1). Therefore, despite significant reduction in the systematic current mismatch loss, not all mismatch losses are eliminated. The losses due to variations in the spectral composition are still present. In terms of total yield, a 0.8% to 1.7% relative gain can be expected from the customization, depending on the weightage of spectral loss in the total losses. It should also be noted that in this case the top cell material usage is reduced for the customized design. This could provide additional benefits in terms of cost. Given that operating conditions vary in different locations, customization for enhanced low-irradiance performance or enhanced temperature tolerance to optimize the cost effectiveness may also be desirable. Even more customization possibilities are available at the PV module level [140].

Table 6.3.1: The PR loss due to spectral effect and annual total yield in Singapore, 2014 before and after customization of top cell thickness to suit Singapore’s local spectrum. The relative gain in yield is shown in the last column.

Configurations	Sub-cell thicknesses ( $\mu\text{m}$ )	PR loss due to spectral effect (%)		Yield ( $\text{kWh}/\text{m}^2$ )		Gain in yield (rel%)
		Before	After	Before	After	
GaAs/Si 2T	0.2 / 200 (before) 0.19 / 200 (after)	3.9	0.056	426	433	1.6
InGaP/Si 2T	2.5 / 200 (before) 2.0 / 200 (after)	1.5	-0.87	425	429	0.8
InGaP/GaAs/Si 2T	0.285 / 0.65 / 200 (before) 0.23 / 0.55 / 200 (after)	4.8	-1.20	446	453	1.7
GaAs/GaAs/Si 2T	0.095 / 0.45 / 200 (before) 0.085 / 0.42 / 200 (after)	3.6	0.036	471	477	1.4

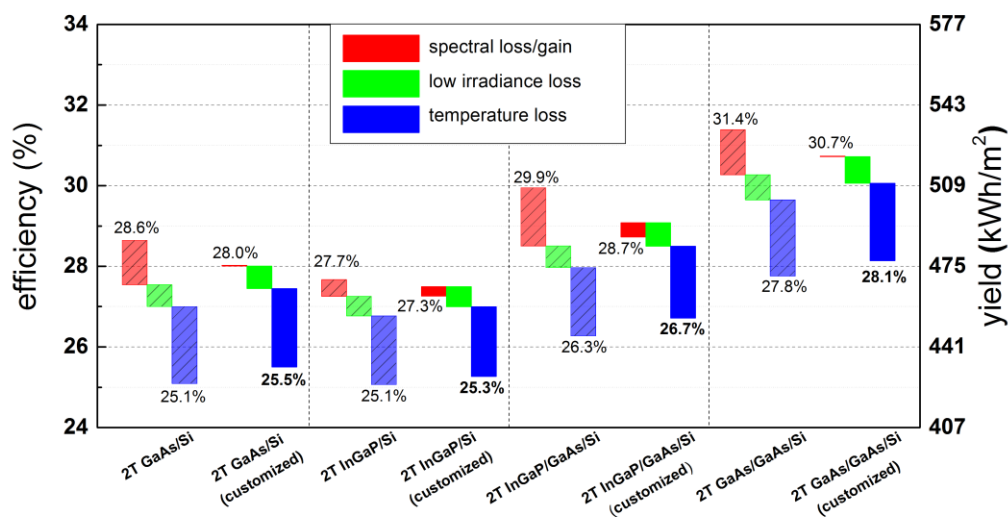


Figure 6.3.1: The loss breakdown for the various 2T III-V/Si tandem configurations before (striped) and after (solid) customizing for the local spectrum of Singapore. The improved harvesting efficiency is indicated in bold text. It should be noted that the STC efficiency would decrease due to these customizations. The improvement in the final harvesting efficiency is mainly due to a reduction in systematic current mismatch loss.

## 6.4. Chapter summary

In this chapter, both time resolved energy yield characteristics and annual energy yields for III-V/Si tandem solar cells were studied. A systematic method to calculate and perform outdoor loss analysis was used. The analysis took into account the effects of spectral deviations from the AM1.5G spectrum, low irradiance levels, and operating cell temperatures, which represent the most important factors affecting the outdoor performance of tandem solar cells for flat-plate PV module applications. These losses cause drops in the performance ratio of PV systems employing tandem solar cells.

Tandem solar cell efficiency varies from day to day. Generally, the harvesting efficiencies for both 2T and 4T configurations tend to be reduced during times of low insolation. The 2T cell efficiency drops tend to be larger than those of 4T devices in

these days, because of larger spectral changes and thus current mismatch. This is because the spectrum tends to be more blue-shifted in days with lower insolation. However, the impact of this on the long-term energy generation is limited, as days with low insolation contribute little to the total insolation. When photon recycling is considered, the calculated yield for the 2T GaAs/Si tandem solar cell is increased by about 1%.

In terms of long-term performance, all simulated tandem solar cells have annual harvesting efficiencies that are lower than their STC efficiencies. The difference was found to be 2% - 4% in Singapore and 1% - 2% in Denver. This corresponds to performance ratios (PR) that are as good, or even better, than those of conventional single-junction Si solar cells.

With the sub-cell models used in this study, only the 4T GaAs/Si tandem cell in Denver achieved a harvesting efficiency of over 30%. For the other investigated tandem configurations, a higher-efficiency Si bottom cell with good light trapping properties is needed to surpass 30% harvesting efficiency. Coupling losses between sub-cells and resistive losses due to integration must be kept as small as possible. A 4T GaAs/Si tandem achieves much higher harvesting efficiency than a world-record level single-junction GaAs solar cell in both Singapore (26.6%) and Denver (27.3%). Generally, it seems that the 4-terminal configuration with best possible sub-cells is most promising for beating single-junction solar cells and for achieving a quantum leap in energy production by flat-plate PV modules.

The contributions from different loss mechanisms to total outdoor PR loss were determined. The analysis showed that the spectral loss can be severe for 2-terminal devices but is generally small for 4-terminal devices. This suggests that the spectral loss mainly comes from current mismatch between the sub-cells in locations where the incoming spectrum differs significantly from the AM1.5G spectrum. Calculations show that this loss can be greatly reduced by customizing the sub-cell thickness to achieve current matching under the average local spectrum. This brings about 0.8% to 1.7% relative gain in the total energy yield in Singapore. The low-irradiance loss is similar for all single-junction and tandem solar cell models considered, but can become slightly larger when a sub-cell operates frequently under very low light intensity. The temperature performance of III-V/Si tandems was predicted to be better than that of a typical single-junction Si solar cell, due to the combined effects of having a smaller temperature coefficient and a lower operating cell temperature.

The developed outdoor loss analysis methodology can also be extended to flat-plate PV modules and PV systems employing tandem solar cells. The insights obtained in this study are also relevant for other Si based tandem solar cells, such as perovskite/Si, especially regarding the expected losses due to variations from the AM1.5G spectrum.



## **Chapter 7. Conclusion**

### **7.1. Summary**

In this work, an energy yield calculation methodology and outdoor loss analysis framework was developed for flat-plate tandem solar cells. Investigations on the energy yield potential and outdoor performance were done for III-V/Si tandems with GaAs, InGaP, dual-junction GaAs/InGaP, and dual junction GaAs/GaAs as top cells, in two different climates represented by Singapore and Denver. The major contributions of this work are as follows:

The realistic outdoor operating conditions in Singapore and Denver, as represented by irradiance level, spectral composition, and ambient air temperature, was described and analysed in Chapter 3. These data were measured with high accuracy and temporal resolution. It was observed that the illumination conditions in Singapore and Denver are significantly different. Singapore has more fluctuations in the irradiance level, due to the abundance of clouds, whereas most insolation comes from high irradiance levels in Denver. The average spectrum in Singapore is more blue-rich than that of Denver. In addition, it was found that the spectral composition and the irradiance level are negatively correlated, particularly for Singapore. Further, using the average photon energy (APE) to characterize the spectral composition, a characteristic set of spectra, which is unique and relatively time invariant for a fixed location, was calculated for each location. An effective way of summarizing the illumination conditions were obtained by sorting measured spectra based on intensities and APE

values. The operating temperature was obtained from ambient air temperature and irradiance level using an empirical model.

In Chapter 4, the tandem solar cells were modelled using optical simulation, physical device simulation (PC1D), as well as analytical temperature models with temperature coefficients. Tandem solar cell outputs under standard testing conditions (STC) as well as other operating conditions were obtained. In addition, several sub-cell models for Si bottom cell and III-V top cells were considered. By simulating the STC efficiencies of double-junction tandem solar cells using different sub-cell combinations, it was found that some combinations were not beneficial, as the tandem efficiency was even lower than the efficiencies of the (stand-alone) sub-cells. Therefore, combination of sub-cells that are of high quality is recommended. By simulating tandem solar cell outputs under a wide range of realistic operating conditions, it was confirmed that spectral variations indeed have a major impact on tandem solar cells, particularly for the 2-terminal configuration. Calculations showed that III-V/Si tandems are expected to have a lower temperature coefficient than conventional single-junction Si solar cells, which is due to the use of III-V materials, and also lower operating temperatures in the field due to their higher PV efficiency.

A fast and efficient energy yield computation algorithm, which is based on the use of a characteristic set of spectra and distribution of operating condition, was developed. This algorithm, outlined in Chapter 5, makes practical the use of very detailed solar irradiance and spectrum data to compute energy yield accurately. Moreover, sophisticated physical device simulation can be employed without consuming too much computational power. This is particularly relevant for solar cells

or modules at the research stage, and is also important for capturing non-linear solar cell efficiency effects that are often neglected when evaluating energy yields. Overall, this method provides a useful way to factor in spectrum in energy yield calculation, by using the average photon energy (APE) concept directly. In addition, a framework for quantifying and breaking down the outdoor losses was proposed. This enables a coherent study of outdoor losses for tandem solar cells taking into account several important and interlinked loss mechanisms at the same time, which was rarely done in the existing literature.

The energy yield methodology for flat-plate tandem solar cells was examined and evaluated in Chapter 5. In particular, the impact of input illumination conditions was investigated. Different temporal resolutions of data points and different ways of obtaining input spectra (simulated with SMARTS or measured) were found to influence the accuracy and uncertainty of the calculated outdoor losses and energy yield values. For long-term yield calculations, detailed input is not vital. However, for short-term yield calculations, high temporal resolution of at least one input data per 30 minutes is needed if a low uncertainty is desired. The conventional method of estimating energy yield, using SMARTS simulated spectra, was found to be inadequate for 1-Sun tandem solar cells, because of the inability to account for the effects of cloud coverage and changing atmospheric conditions. Even after modifying the SMARTS generated spectra with measured intensity data, the predicted loss in harvesting efficiency was still underestimated by about 30% to 60%. Therefore, a better representation of the actual spectral composition is desired.

The realistic outdoor energy yield of several III-V/Si tandem solar cells was calculated in Chapter 6. The tandem structures included double-junction (GaAs/Si and InGaP/Si, in both 2T and 4T configuration) as well as triple-junction (2T InGaP/GaAs/Si and 2T GaAs/GaAs/Si). Time-resolved energy yield revealed how the rapidly changing illumination conditions at different moments influence the real-time solar cell output. Generally, the harvesting efficiencies for both 2T and 4T tandems tend to be reduced during times of low insolation. In terms of long-term performance, all simulated tandem solar cells have annual harvesting efficiencies that are lower than their STC efficiencies, which is consistent across several years. The difference was found to be 2 - 4 % in Singapore and 1 - 2 % in Denver. This corresponds to performance ratios (PR) that are as good, or even better, than those of conventional single-junction Si solar cells. The contributions from different loss mechanisms to total outdoor PR drop were broken down. It was found that current mismatch losses for 2T tandems are significant in Singapore, where the incoming spectrum differs significantly from the AM1.5G spectrum. However, this could be reduced by customizing the sub-cell thickness to achieve current matching under the average local spectrum, which brings about 0.8% to 1.7% relative gain in the total energy yield. The temperature related loss was found to be the largest outdoor loss for all tandems investigated, but the temperature performance of III-V/Si tandems was predicted to be better than that of a typical single-junction Si solar cell, due to the combined effects of having a smaller temperature coefficient and a lower operating cell temperature.

## **7.2. Proposed future work**

In this thesis, a new approach of energy yield calculation was developed that included spectral effects, which was a significant expansion from previous calculation methodologies. This proved to be particularly important for flat-plate tandem solar cells. Moreover, detailed description of operating conditions and detailed device modelling was used to make the yield analysis more accurate. Future work is recommended to further advance this yield calculation approach. There are several aspects for this.

Firstly, it was identified that representation of operating conditions is important. Therefore, more work could be done to improve input data availability and quality. Currently, measured spectrum data are not widely available, and simple spectrum simulation is often inadequate in reproducing the global spectrum. The situation can be improved by performing ground based spectrum measurements in more locations, or by developing better ways to predict solar spectrum, such as via extensive incorporation of satellite measurements of clouds and atmospheric properties. Techniques for reconstructing the illumination conditions from limited data is potentially an important topic for yield analysis.

Secondly, more data analytics could be performed on the measured illumination conditions. For instance, the effects of clouds on global spectrum could be further studied. More investigations can also be performed on the correlations between irradiance level, spectrum, cloud fraction, temperature, or other relevant meteorological parameters. This could be potentially helpful in predicting operating conditions, in understanding the energy output patterns, as well as in the designing of tandem solar cells.

Thirdly, the use of characteristic set of spectra for yield calculation opens up interesting new possibilities of measuring and using APE. Once the characteristic set of spectra is available for a certain location, the time series of APE values can potentially be measured economically by a simple sensor, thus enabling real-time energy yield calculations for PV monitoring. Also, both historical measured average, and statistically forecasted time series (or distributions) of APE values can be used as inputs to yield prediction.

Also, in this thesis, the energy yield potential and outdoor loss characteristics of flat-plate tandem solar cells was studied in depth. This is instrumental in informing tandem solar cell design as well as its economic viability. More accurate and extensive energy yield studies for tandem solar cells could be performed in the future.

For instance, experimental studies and better modelling on the operating tandem solar cell temperature could be beneficial. Also, better device simulation is desired. This can be achieved by using more sophisticated simulation software such as Sentaurus TCAD, and by including more features such as tunnel junctions and contacts. Ray tracing optical calculation can also be used to determine the optical absorption in textured Si bottom cell, adhesion layers or encapsulations. In addition, more connection and wiring configurations are possible for tandem modules, such as “areal” current matching [28, 29, 35] or voltage matching [50]. As a consequence, tandem solar module behaviour can be more complex than a single unit of tandem solar cell. Thus modelling at the module level or even the system level could become important. The energy yield study can also be extended to cover more locations, more module orientations, or more operation environments (such as mobile and indoor applications).

Last but not least, experimental validation of the yield calculation methodology is needed. Outdoor testing using prototype tandem solar cells is required to confirm the calculated energy yields and the predicted outdoor loss characteristics.

## Bibliography

1. NREL, *NREL efficiency chart*, 2015, available: <http://www.nrel.gov/ncpv/>
2. G. Masson, S. Orlandi, and M. Reking, *Global Market Outlook for Photovoltaics 2014-2018*, European Photovoltaic Industry Association, 2014.
3. A. Luque and S. Hegedus, *Handbook of Photovoltaic Science and Engineering, Second Edition*. 2 ed. : John Wiley & Sons, Ltd, 2011.
4. C. Kost, J. Mayer, J. Thomsen, and T. Schlegl, *Levelized Cost of Electricity Renewable Energy Technologies*. Fraunhofer Institute for Solar Energy Systems, 2013.
5. ITRPV, *International Technology Roadmap for Photovoltaic: Results 2015*. 2016.
6. International Renewable Energy Agency, *Renewable Energy Technologies: Cost Analysis Series*. 2012.
7. S. Smith and M. Shiao, *Solar PV Balance of System (BOS) Markets: Technologies, Costs and Leading Companies, 2013-2016*. GTM Research, 2012.
8. International Energy Agency and Nuclear Energy Agency, *Projected Costs of Generating Electricity*, 2015.
9. M.A. Green, K. Emery, Y. Hishikawa, W. Warta, and E.D. Dunlop, "Solar cell efficiency tables (version 47)," *Progress in Photovoltaics: Research and Applications*, **24**(1): p. 3-11, 2016.
10. K. Masuko, M. Shigematsu, T. Hashiguchi, D. Fujishima, M. Kai, N. Yoshimura, T. Yamaguchi, Y. Ichihashi, T. Mishima, N. Matsubara, T. Yamanishi, T. Takahama, M. Taguchi, E. Maruyama, and S. Okamoto, "Achievement of More Than 25% Conversion Efficiency With Crystalline Silicon Heterojunction Solar Cell," *IEEE Journal of Photovoltaics*, **4**(6): p. 1433-1435, 2014.
11. B.M. Kayes, N. Hui, R. Twist, S.G. Spruytte, F. Reinhardt, I.C. Kizilyalli, and G.S. Higashi. "27.6% Conversion efficiency, a new record for single-junction solar cells under 1 sun illumination". in *37th IEEE Photovoltaic Specialists Conference*, 2011.
12. P. Würfel, *Physics of Solar Cells - From Principles to New Concepts*: WILEY-VCH Verlag GmBH & Co, 2005.
13. P. Faine, S.R. Kurtz, C. Riordan, and J.M. Olson, "The influence of spectral solar irradiance variations on the performance of selected single-junction and multijunction solar cells," *Solar Cells*, **31**(3): p. 259-278, 1991.
14. M.A. Green, "Photovoltaic principles," *Physica E: Low-dimensional Systems and Nanostructures*, **14**(1-2): p. 11-17, 2002.
15. C. Honsberg and S. Bowden. *PV Education*. Available from: <http://www.pveducation.org/>.
16. International Electrotechnical Commission, *Photovoltaic devices Part 1: Measurement of photovoltaic current-voltage characteristics*. 2006: Geneva, Switzerland.



17. American Society for Testing and Materials, *Standard Tables for Reference Solar Spectral Irradiances: Direct Normal and Hemispherical on 37° Tilted Surface*. 2012.
18. J.Y. Ye, T. Reindl, A.G. Aberle, and T.M. Walsh, "Effect of solar spectrum on the performance of various thin-film PV module technologies in tropical Singapore," *IEEE Journal of Photovoltaics*, **PP**(99): p. 1-7, 2014.
19. S. Nann and K. Emery, "Spectral effects on PV-device rating," *Solar Energy Materials and Solar Cells*, **27**(3): p. 189-216, 1992.
20. M.A. Green, "General temperature dependence of solar cell performance and implications for device modelling," *Progress in Photovoltaics: Research and Applications*, **11**(5): p. 333-340, 2003.
21. O. Dupré, R. Vaillon, and M.A. Green, "Physics of the temperature coefficients of solar cells," *Solar Energy Materials and Solar Cells*, **140**: p. 92-100, 2015.
22. W. Shockley and H.J. Queisser, "Detailed Balance Limit of Efficiency of p-n Junction Solar Cells," *Journal of Applied Physics*, **32**(3): p. 510-519, 1961.
23. C.H. Henry, "Limiting efficiencies of ideal single and multiple energy gap terrestrial solar cells," *Journal of Applied Physics*, **51**(8): p. 4494-4500, 1980.
24. S. Kurtz, D. Myers, W.E. McMahon, J. Geisz, and M. Steiner, "A comparison of theoretical efficiencies of multi-junction concentrator solar cells," *Progress in Photovoltaics: Research and Applications*, **16**(6): p. 537-546, 2008.
25. S.R. Kurtz, P. Faine, and J.M. Olson, "Modeling of two-junction, series-connected tandem solar cells using top-cell thickness as an adjustable parameter," *Journal of Applied Physics*, **68**(4): p. 1890-1895, 1990.
26. I. Mathews, D. O'Mahony, B. Corbett, and A.P. Morrison, "Theoretical performance of multi-junction solar cells combining III-V and Si materials," *Opt. Express*, **20**(S5): p. A754-A764, 2012.
27. M. Born and E. Wolf, *Principles of Optics: Electromagnetic Theory of Propagation, Interference and Diffraction of Light*. 1997: Cambridge University Press.
28. J. Yang, Z. Peng, D. Cheong, and R.N. Kleiman. "III-V-on-Silicon Multi-Junction Solar Cell with 25% 1-Sun Efficiency via Direct Metal Interconnect and Areal Current Matching". in *27th European Photovoltaic Solar Energy Conference and Exhibition*. 2012.
29. S. Abdul Hadi, E.A. Fitzgerald, and A. Nayfeh, "Theoretical efficiency limit for a two-terminal multi-junction "step-cell" using detailed balance method," *Journal of Applied Physics*, **119**(7): p. 073104, 2016.
30. D.J. Friedman, "Progress and challenges for next-generation high-efficiency multijunction solar cells," *Current Opinion in Solid State and Materials Science*, **14**(6): p. 131-138, 2010.
31. A. Luque, "Will we exceed 50% efficiency in photovoltaics?," *Journal of Applied Physics*, **110**(3): p. 031301-19, 2011.
32. R.R. King, D.C. Law, K.M. Edmondson, C.M. Fetzer, G.S. Kinsey, H. Yoon, R.A. Sherif, and N.H. Karam, "40% efficient metamorphic GaInP/GaInAs/Ge multijunction solar cells," *Applied Physics Letters*, **90**(18), 2007.
33. M. Woodhouse and A. Goodrich, *A Manufacturing Cost Analysis Relevant to Single- and Dual-Junction Photovoltaic Cells Fabricated with III-Vs and III-*

- Vs Grown on Czochralski Silicon*. National Renewable Energy Laboratory, 2013.
34. M. Liu, M.B. Johnston, and H.J. Snaith, "Efficient planar heterojunction perovskite solar cells by vapour deposition," *Nature*, **501**(7467): p. 395-398, 2013.
  35. C.D. Bailie, M.G. Christoforo, J.P. Mailoa, A.R. Bowring, E.L. Unger, W.H. Nguyen, J. Burschka, N. Pellet, J.Z. Lee, M. Gratzel, R. Noufi, T. Buonassisi, A. Salleo, and M.D. McGehee, "Semi-transparent perovskite solar cells for tandems with silicon and CIGS," *Energy & Environmental Science*, (3): p. 956-963, 2015.
  36. K.A. Bush, C.D. Bailie, Y. Chen, A.R. Bowring, W. Wang, W. Ma, T. Leijtens, F. Moghadam, and M.D. McGehee. "Thermal and Environmental Stability of Semi-Transparent Perovskite Solar Cells for Tandems Enabled by a Solution-Processed Nanoparticle Buffer Layer and Sputtered ITO Electrode". in *43rd IEEE Photovoltaic Specialist Conference*. 2016. Portland, USA.
  37. S.F. Fang, K. Adomi, S. Iyer, H. Morkoç, H. Zabel, C. Choi, and N. Otsuka, "Gallium arsenide and other compound semiconductors on silicon," *Journal of Applied Physics*, **68**(7): p. R31-R58, 1990.
  38. J.F. Geisz and D.J. Friedman, "III–N–V semiconductors for solar photovoltaic applications," *Semiconductor Science and Technology*, **17**(8): p. 769, 2002.
  39. J.F. Geisz, M.A. Steiner, I. García, S.R. Kurtz, and D.J. Friedman, "Enhanced external radiative efficiency for 20.8% efficient single-junction GaInP solar cells," *Applied Physics Letters*, **103**(4), 2013.
  40. T. Soga, M. Yang, T. Jimbo, and M. Umeno, "High-Efficiency Monolithic Three-Terminal GaAs/Si Tandem Solar Cells Fabricated by Metalorganic Chemical Vapor Deposition," *Japanese Journal of Applied Physics*, **35** (Part 1, No. 2B): p. 1401, 1996.
  41. M. Umeno, T. Kato, T. Egawa, T. Soga, and T. Jimbo, "High efficiency AlGaAs/Si tandem solar cell over 20%," *Solar Energy Materials and Solar Cells*, **41–42**(0): p. 395-403, 1996.
  42. C.L. Andre, J.A. Carlin, J.J. Boeckl, D.M. Wilt, M.A. Smith, A.J. Pitera, M.L. Lee, E.A. Fitzgerald, and S.A. Ringel, "Investigations of high-performance GaAs solar cells grown on Ge-Si<sub>1-x</sub>Gex-Si substrates," *IEEE Transactions on Electron Devices*, **52**(6): p. 1055-1060, 2005.
  43. J.F. Geisz, J.M. Olson, M.J. Romero, C.S. Jiang, and A.G. Norman. "Lattice-mismatched GaAsP Solar Cells Grown on Silicon by OMVPE". in *4th World Conference on Photovoltaic Energy Conversion*. 2006.
  44. T.J. Grassman, J.A. Carlin, C. Ratcliff, D.J. Chmielewski, and S.A. Ringel. "Epitaxially-grown metamorphic GaAsP/Si dual-junction solar cells". in *39th IEEE Photovoltaic Specialists Conference*, 2013.
  45. K. Hayashi, T. Soga, H. Nishikawa, T. Jimbo, and M. Umeno. "MOCVD growth of GaAsP on Si for tandem solar cell application". in *First World Conference on Photovoltaic Energy Conversion*, 1994.
  46. M.R. Lueck, C.L. Andre, A.J. Pitera, M.L. Lee, E.A. Fitzgerald, and S.A. Ringel, "Dual junction GaInP/GaAs solar cells grown on metamorphic SiGe/Si

- substrates with high open circuit voltage," *IEEE Electron Device Letters*, **27**(3): p. 142-144, 2006.
47. H. Taguchi, T. Soga, and T. Jimbo, "Fabrication of GaAs/Si tandem solar cell by epitaxial lift-off technique," *Japanese Journal of Applied Physics, Part 2: Letters*, **42**(12 Acon): p. L1419-L1421, 2003.
  48. K. Derendorf, S. Essig, E. Oliva, V. Klingner, T. Roesener, S.P. Philipps, J. Benick, M. Hermle, M. Schachtner, G. Siefert, W. Jäger, and F. Dimroth, "Fabrication of GaInP/GaAs//Si Solar Cells by Surface Activated Direct Wafer Bonding," *IEEE Journal of Photovoltaics*, **3**(4): p. 1-6, 2013.
  49. R. Cariou, J. Benick, M. Hermle, D. Lackner, S. Glunz, A.W. Bett, and F. Dimroth. "Development of Highly-Efficient III-V // Si Wafer-Bonded Triple-Junction Solar Cells". in *43rd IEEE Photovoltaic Specialist Conference*. 2016. Portland, USA.
  50. J.M. Gee, "A comparison of different module configurations for multi-band-gap solar cells," *Solar Cells*, **24**(1-2): p. 147-155, 1988.
  51. N. Huang, C. Lin, and M.L. Povinelli, "Limiting efficiencies of tandem solar cells consisting of III-V nanowire arrays on silicon," *Journal of Applied Physics*, **112**(6): p. 064321-9, 2012.
  52. S. Jae Cheol, K. Kyou Hyun, H. Hu, Y. Ki Jun, J.A. Rogers, Z. Jian-Min, and L. Xiuling. "Monolithically grown In<sub>x</sub>Ga<sub>1-x</sub>As nanowire array on silicon tandem solar cells with high efficiency". in *IEEE Photonics Conference*. 2011.
  53. R.R. LaPierre, "Theoretical conversion efficiency of a two-junction III-V nanowire on Si solar cell," *Journal of Applied Physics*, **110**(1): p. 014310-6, 2011.
  54. W. Long, L. Xinhua, Z. Zhifei, B. Shaojiang, Z. XueSong, H. Jin-hua, and W. Yuqi, "Theoretical consideration of III-V nanowire/Si triple-junction solar cells," *Nanotechnology*, **23**(50): p. 505202, 2012.
  55. J. Wallentin, N. Anttu, D. Asoli, M. Huffman, I. Åberg, M.H. Magnusson, G. Siefert, P. Fuss-Kailuweit, F. Dimroth, B. Witzigmann, H.Q. Xu, L. Samuelson, K. Deppert, and M.T. Borgström, "InP Nanowire Array Solar Cells Achieving 13.8% Efficiency by Exceeding the Ray Optics Limit," *Science*, **339**(6123): p. 1057-1060, 2013.
  56. S. Essig, M.A. Steiner, C. Alleb, x00E, J.F. Geisz, B. Paviet-Salomon, S. Ward, A. Descoeur, V. LaSalvia, L. Barraud, N. Badel, A. Faes, J. Levrat, M. Despeisse, C. Ballif, P. Stradins, and D.L. Young, "Realization of GaInP/Si Dual-Junction Solar Cells With 29.8% 1-Sun Efficiency," *IEEE Journal of Photovoltaics*, **PP**(99): p. 1-8, 2016.
  57. E. Lorenzo, *Energy Collected and Delivered by PV Modules*, in *Handbook of Photovoltaic Science and Engineering*, John Wiley & Sons Ltd, 2012, p. 905-970.
  58. N.H. Reich, B. Mueller, A. Armbruster, W.G.J.H.M. van Sark, K. Kiefer, and C. Reise, "Performance ratio revisited: is PR > 90% realistic?," *Progress in Photovoltaics: Research and Applications*, **20**(6): p. 717-726, 2012.
  59. S.P. Philipps, G. Peharz, R. Hoheisel, T. Hornung, N.M. Al-Abbadi, F. Dimroth, and A.W. Bett, "Energy harvesting efficiency of III-V triple-junction

- concentrator solar cells under realistic spectral conditions," *Solar Energy Materials and Solar Cells*, **94**(5): p. 869-877, 2010.
60. International Electrotechnical Commission, *Photovoltaic system performance monitoring - Guidelines for measurement, data exchange and analysis*. 1998.
  61. National Solar Repository. *Solar Basics*. 2016; Available from: <http://www.solar-repository.sg/solar-basics>.
  62. NREL, *National Solar Radiation Data Base*. Available from: [http://rredc.nrel.gov/solar/old\\_data/nsrdb/1991-2005/tmy3/by\\_state\\_and\\_city.html](http://rredc.nrel.gov/solar/old_data/nsrdb/1991-2005/tmy3/by_state_and_city.html).
  63. J.E. Hay and D.C. McKay, "Estimating Solar Irradiance on Inclined Surfaces: A Review and Assessment of Methodologies," *International Journal of Solar Energy*, **3**(4-5): p. 203-240, 1985.
  64. R. Perez, R. Seals, P. Ineichen, R. Stewart, and D. Menicucci, "A new simplified version of the perez diffuse irradiance model for tilted surfaces," *Solar Energy*, **39**(3): p. 221-231, 1987.
  65. R. Perez, R. Stewart, C. Arbogast, R. Seals, and J. Scott, "An anisotropic hourly diffuse radiation model for sloping surfaces: Description, performance validation, site dependency evaluation," *Solar Energy*, **36**(6): p. 481-497, 1986.
  66. C.A. Gueymard, "Direct and indirect uncertainties in the prediction of tilted irradiance for solar engineering applications," *Solar Energy*, **83**(3): p. 432-444, 2009.
  67. M. David, P. Lauret, and J. Boland, "Evaluating tilted plane models for solar radiation using comprehensive testing procedures, at a southern hemisphere location," *Renewable Energy*, **51**: p. 124-131, 2013.
  68. A. de Miguel, J. Bilbao, R. Aguiar, H. Kambezidis, and E. Negro, "Diffuse solar irradiation model evaluation in the North Mediterranean Belt area," *Solar Energy*, **70**(2): p. 143-153, 2001.
  69. *PVSYS V6.46*. 2016; Available from: <http://www.pvsyst.com/>.
  70. G.S. Kinsey, "Spectrum Sensitivity, Energy Yield, and Revenue Prediction of PV Modules," *IEEE Journal of Photovoltaics*, **5**(1): p. 258-262, 2015.
  71. M. Lee, A. Panchula, F. Solar, and S. Francisco. "Spectral Correction for Photovoltaic Module Performance Based on Air Mass and Precipitable Water". in *43rd IEEE Photovoltaic Specialist Conference*. 2016. Portland, USA.
  72. M. Mikofski, A. Oumbe, C. Li, B. Bourne, S. Corp, S.A. Total, P. La, and D. Cedex. "Evaluation and Correction of the Impact of Spectral Variation of Irradiance on PV Performance". in *43rd IEEE Photovoltaic Specialist Conference*. 2016. Portland, USA.
  73. R. Gottschalg, D.G. Infield, and M.J. Kearney, "Experimental study of variations of the solar spectrum of relevance to thin film solar cells," *Solar Energy Materials and Solar Cells*, **79**(4): p. 527-537, 2003.
  74. W. Xiaoting and A. Barnett, "The Effect of Spectrum Variation on the Energy Production of Triple-Junction Solar Cells," *IEEE Journal of Photovoltaics*, **2**(4): p. 417-423, 2012.
  75. M. Alonso-Abella, F. Chenlo, G. Nofuentes, and M. Torres-Ramírez, "Analysis of spectral effects on the energy yield of different PV (photovoltaic) technologies: The case of four specific sites," *Energy*, **67**(0): p. 435-443, 2014.

76. T. Mishima, M. Taguchi, H. Sakata, and E. Maruyama, "Development status of high-efficiency HIT solar cells," *Solar Energy Materials and Solar Cells*, **95**(1): p. 18-21, 2011.
77. K. Araki and M. Yamaguchi, "Influences of spectrum change to 3-junction concentrator cells," *Solar Energy Materials and Solar Cells*, **75**(3-4): p. 707-714, 2003.
78. N.L.A. Chan, T.B. Young, H.E. Brindley, N.J. Ekins-Daukes, K. Araki, Y. Kemmoku, and M. Yamaguchi, "Validation of energy prediction method for a concentrator photovoltaic module in Toyohashi Japan," *Progress in Photovoltaics: Research and Applications*, **21**(8): p. 1598-1610, 2013.
79. E.F. Fernández, F. Almonacid, J.A. Ruiz-Arias, and A. Soria-Moya, "Analysis of the spectral variations on the performance of high concentrator photovoltaic modules operating under different real climate conditions," *Solar Energy Materials and Solar Cells*, **127**(0): p. 179-187, 2014.
80. G.S. Kinsey and K.M. Edmondson, "Spectral response and energy output of concentrator multijunction solar cells," *Progress in Photovoltaics: Research and Applications*, **17**(5): p. 279-288, 2009.
81. S. Senthilarasu, E.F. Fernández, F. Almonacid, and T.K. Mallick, "Effects of spectral coupling on perovskite solar cells under diverse climatic conditions," *Solar Energy Materials and Solar Cells*, **133**(0): p. 92-98, 2015.
82. R. Gottschalg, T.R. Betts, D.G. Infield, and M.J. Kearney, "The effect of spectral variations on the performance parameters of single and double junction amorphous silicon solar cells," *Solar Energy Materials and Solar Cells*, **85**(3): p. 415-428, 2005.
83. Y. Hirata and T. Tani, "Output variation of photovoltaic modules with environmental factors—I. The effect of spectral solar radiation on photovoltaic module output," *Solar Energy*, **55**(6): p. 463-468, 1995.
84. C. Gueymard, *SMARTS2: a simple model of the atmospheric radiative transfer of sunshine: algorithms and performance assessment*. Professional Paper FSEC-PF-270-95. Florida Solar Energy Center, Cocoa, FL, 1995.
85. *Solar Energy Research Institute of Singapore*. 2016; Available from: <http://www.seris.sg/>.
86. L. Dunn, M. Gostein, and K. Emery. "Comparison of pyranometers vs. PV reference cells for evaluation of PV array performance". in *38th IEEE Photovoltaic Specialists Conference*, 2012.
87. K. Zonen. *The Working Principle of a Thermopile Pyranometer*, 2016, Available from: <http://www.kippzonen.com/News/572/The-Working-Principle-of-a-Thermopile-Pyranometer#>.
88. B.J. Brinkworth and T.D.R. Hughes, "Accelerated response of thermopile pyranometers," *Solar Energy*, **18**(5): p. 403-404, 1976.
89. Delta-T Devices. *SPN1 Sunshine Pyranometer*. 2016, Available from: <http://www.delta-t.co.uk/product-display.asp?id=SPN1%20Product&div=Meteorology%20and%20Solar>.
90. A. Andreas and T. Stoffel, *NREL Solar Radiation Research Laboratory (SRRL): Baseline Measurement System (BMS)*, NREL. 1981.

91. G.A. Zerlaut and J.D. Maybee, "Spectroradiometer measurements in support of photovoltaic device testing," *Solar Cells*, **7**(1): p. 97-106, 1982.
92. EKO Instruments. *MS-700 Spectroradiometer*. 2016, Available from: <https://eko-eu.com/products/photovoltaic-evaluation-systems/spectroradiometers/ms-700-spectroradiometer>.
93. T. Ishii, K. Otani, T. Takashima, and Y. Xue, "Solar spectral influence on the performance of photovoltaic (PV) modules under fine weather and cloudy weather conditions," *Progress in Photovoltaics: Research and Applications*, **21**(4): p. 481-489, 2013.
94. M. Krawczynski, M.B. Strobel, and R. Gottschalg. "Intercomparison of spectroradiometers for outdoor performance monitoring". in *24th European Photovoltaic Solar Energy Conference*. 2009. Hamburg, Germany.
95. R. Galleano, W. Zaaiman, A. Virtuani, D. Pavanello, P. Morabito, A. Minuto, A. Spina, S. Bartocci, R. Fucci, G. Leanza, D. Fasanaro, and M. Catena, "Intercomparison campaign of spectroradiometers for a correct estimation of solar spectral irradiance: results and potential impact on photovoltaic devices calibration," *Progress in Photovoltaics: Research and Applications*, 2013.
96. A.E. Curtright and J. Apt, "The character of power output from utility-scale photovoltaic systems," *Progress in Photovoltaics: Research and Applications*, **16**(3): p. 241-247, 2008.
97. A. Kankiewicz, M. Sengupta, and D. Moon. "Observed Impacts of Transient Clouds on Utility Scale PV Fields". in *SOLAR 2010 Conference*, 2010, Phoenix, Arizona.
98. B. Burger and R. Rüther, "Inverter sizing of grid-connected photovoltaic systems in the light of local solar resource distribution characteristics and temperature," *Solar Energy*, **80**(1): p. 32-45, 2006.
99. A. Nobre (2015), *Short-term solar irradiance forecasting and photovoltaic systems performance in a tropical climate in Singapore* (Doctoral dissertation), Universidade Federal de Santa Catarina.
100. T. Minemoto, Y. Nakada, H. Takahashi, and H. Takakura, "Uniqueness verification of solar spectrum index of average photon energy for evaluating outdoor performance of photovoltaic modules," *Solar Energy*, **83**(8): p. 1294-1299, 2009.
101. Y. Du, C.J. Fell, B. Duck, D. Chen, K. Liffman, Y. Zhang, M. Gu, and Y. Zhu, "Evaluation of photovoltaic panel temperature in realistic scenarios," *Energy Conversion and Management*, **108**: p. 60-67, 2016.
102. M. Koehl, M. Heck, S. Wiesmeier, and J. Wirth, "Modeling of the nominal operating cell temperature based on outdoor weathering," *Solar Energy Materials and Solar Cells*, **95**(7): p. 1638-1646, 2011.
103. R.G. Ross Jr. "Interface design considerations for terrestrial solar cell modules". in *12th Photovoltaic Specialists Conference*. 1976.
104. E. Skoplaki and J.A. Palyvos, "Operating temperature of photovoltaic modules: A survey of pertinent correlations," *Renewable Energy*, **34**(1): p. 23-29, 2009.
105. A.J. Veldhuis, A.M. Nobre, I.M. Peters, T. Reindl, R. Ruther, and A.H.M.E. Reinders, "An Empirical Model for Rack-Mounted PV Module Temperatures

- for Southeast Asian Locations Evaluated for Minute Time Scales," *IEEE Journal of Photovoltaics*, **5**(3): p. 774-782, 2015.
106. Z. Ye, A. Nobre, T. Reindl, J. Luther, and C. Reise, "On PV module temperatures in tropical regions," *Solar Energy*, **88**: p. 80-87, 2013.
  107. R.G. Ross, *Flat-Plate Photovoltaic Array Design Optimization*, in *14th IEEE Photovoltaic Specialists Conference*. 1980: San Diego, CA.
  108. S. Siegel, "Nonparametric Statistics," *The American Statistician*, **11**(3): p. 13-19, 1957.
  109. D.A. Clugston and P.A. Basore. "PC1D version 5: 32-bit solar cell modeling on personal computers". in *26<sup>th</sup> IEEE Photovoltaic Specialists Conference*, 1997.
  110. A. Fell, K.R. McIntosh, P.P. Altermatt, G.J.M. Janssen, R. Stangl, A. Ho-Baillie, H. Steinkemper, J. Greulich, M. Muller, B. Min, K.C. Fong, M. Hermle, I.G. Romijn, and M.D. Abbott, "Input Parameters for the Simulation of Silicon Solar Cells in 2014," *IEEE Journal of Photovoltaics*, **5**(4): p. 1250-1263, 2015.
  111. M.M. Hilali, K. Nakayashiki, A. Ebong, and A. Rohatgi, "High-efficiency (19%) screen-printed textured cells on low-resistivity float-zone silicon with high sheet-resistance emitters," *Progress in Photovoltaics: Research and Applications*, **14**(2): p. 135-144, 2006.
  112. S. De Wolf, J. Szlufcik, Y. Delannoy, I. Périchaud, C. Häßler, and R. Einhaus, "Solar cells from upgraded metallurgical grade (UMG) and plasma-purified UMG multi-crystalline silicon substrates," *Solar Energy Materials and Solar Cells*, **72**(1-4): p. 49-58, 2002.
  113. D. Zielke, J.H. Petermann, F. Werner, B. Veith, R. Brendel, and J. Schmidt. "21.7 % Efficient PERC Solar Cells with AlO<sub>x</sub> Tunneling Layer". in *26th European Photovoltaic Solar Energy Conference and Exhibition*. 2011. Hamburg, Germany.
  114. J. Zhao, A. Wang, M.A. Green, and F. Ferrazza, "19.8% efficient "honeycomb" textured multicrystalline and 24.4% monocrystalline silicon solar cells," *Applied Physics Letters*, **73**(14): p. 1991-1993, 1998.
  115. I. Romijn, I. Cesar, M. Koppes, E. Kossen, and A. Weeber. "PASHA: A new industrial process technology enabling high efficiencies on thin and large mc-Si wafers". in *33rd IEEE Photovoltaic Specialists Conference*, 2008.
  116. H.S. Chang, "Effect of passivation process in upgraded metallurgical grade (UMG)-silicon solar cells," *Solar Energy Materials and Solar Cells*, **95**(1): p. 63-65, 2011.
  117. M.A. Green, K. Emery, Y. Hishikawa, W. Warta, and E.D. Dunlop, "Solar cell efficiency tables (Version 45)," *Progress in Photovoltaics: Research and Applications*, **23**(1): p. 1-9, 2015.
  118. M. Yamaguchi, C. Amano, and Y. Itoh, "Numerical analysis for high - efficiency GaAs solar cells fabricated on Si substrates," *Journal of Applied Physics*, **66**(2): p. 915-919, 1989.
  119. S.P. Tobin, S.M. Vernon, C. Bajgar, L.M. Geoffroy, C.J. Keavney, M.M. Sanfacon, and V.E. Haven, "Device processing and analysis of high efficiency GaAs cells," *Solar Cells*, **24**(1-2): p. 103-115, 1988.

120. G.J. Bauhuis, P. Mulder, E.J. Haverkamp, J.C.C.M. Huijben, and J.J. Schermer, "26.1% thin-film GaAs solar cell using epitaxial lift-off," *Solar Energy Materials and Solar Cells*, **93**(9): p. 1488-1491, 2009.
121. S.R. Kurtz, J.M. Olson, D.J. Friedman, J.F. Geisz, K.A. Bertness, and A.E. Kibbler. "Passivation of Interfaces in High-Efficiency Photovoltaic Devices". in *Materials Research Society Spring Meeting 1999*. 1999. San Francisco, California.
122. T. Takamoto, E. Ikeda, H. Kurita, and M. Ohmori, "Structural optimization for single junction InGaP solar cells," *Solar Energy Materials and Solar Cells*, **35**(0): p. 25-31, 1994.
123. T. Takamoto, E. Ikeda, H. Kurita, and M. Ohmori. "High efficiency InGaP solar cells for InGaP/GaAs tandem cell application". in *First World Conference on Photovoltaic Energy Conversion*, 1994.
124. A. Marti, J.L. Balenzategui, and R.F. Reyna, "Photon recycling and Shockley's diode equation," *Journal of Applied Physics*, **82**(8): p. 4067-4075, 1997.
125. E. Yablonovitch, O.D. Miller, and S.R. Kurtz. "The opto-electronic physics that broke the efficiency limit in solar cells". in *38th IEEE Photovoltaic Specialists Conference*, 2012.
126. Z. Ren, J.P. Mailoa, Z. Liu, H. Liu, S.C. Siah, T. Buonassisi, and I.M. Peters, "Numerical Analysis of Radiative Recombination and Reabsorption in GaAs/Si Tandem," *IEEE Journal of Photovoltaics*, **5**(4): p. 1079-1086, 2015.
127. I.M. Peters, S. Sofia, J. Mailoa, and T. Buonassisi, "Techno-economic analysis of tandem photovoltaic systems," *RSC Advances*, **6**(71): p. 66911-66923, 2016.
128. N. Cavassilas, C. Gelly, F. Michelini, and M. Bescond, "Reflective Barrier Optimization in Ultrathin Single-Junction GaAs Solar Cell," *IEEE Journal of Photovoltaics*, **5**(6): p. 1621-1625, 2015.
129. S. Essig, S. Ward, M.A. Steiner, D.J. Friedman, J.F. Geisz, P. Stradins, and D.L. Young, "Progress Towards a 30% Efficient GaInP/Si Tandem Solar Cell," *Energy Procedia*, **77**: p. 464-469, 2015.
130. P. Singh and N.M. Ravindra, "Temperature dependence of solar cell performance—an analysis," *Solar Energy Materials and Solar Cells*, **101**: p. 36-45, 2012.
131. A. Braun, E.A. Katz, and J.M. Gordon, "Basic aspects of the temperature coefficients of concentrator solar cell performance parameters," *Progress in Photovoltaics: Research and Applications*, **21**(5): p. 1087-1094, 2013.
132. G. Siefert and A.W. Bett, "Analysis of temperature coefficients for III–V multi-junction concentrator cells," *Progress in Photovoltaics: Research and Applications*, **22**(5): p. 515-524, 2014.
133. T. Hove, "A method for predicting long-term average performance of photovoltaic systems," *Renewable Energy*, **21**(2): p. 207-229, 2000.
134. H. Liu, A. Aberle, T. Buonassisi, and I.M. Peters, "On the methodology of energy yield assessment for one-Sun tandem solar cells," *Solar Energy*, **135**: p. 598-604, 2016.
135. B. Müller, L. Hardt, A. Armbruster, K. Kiefer, and C. Reise, "Yield predictions for photovoltaic power plants: empirical validation, recent advances and



- remaining uncertainties," *Progress in Photovoltaics: Research and Applications*, **24**(4): p. 570–583, 2015.
136. R. Mueller, T. Behrendt, A. Hammer, and A. Kemper, "A New Algorithm for the Satellite-Based Retrieval of Solar Surface Irradiance in Spectral Bands," *Remote Sensing*, **4**(3): p. 622, 2012.
137. R.W. Mueller, K.F. Dagestad, P. Ineichen, M. Schroedter-Homscheidt, S. Cros, D. Dumortier, R. Kuhlemann, J.A. Olseth, G. Piernavieja, C. Reise, L. Wald, and D. Heinemann, "Rethinking satellite-based solar irradiance modelling: The SOLIS clear-sky module," *Remote Sensing of Environment*, **91**(2): p. 160-174, 2004.
138. P.W. Stackhouse, *NASA Surface meteorology and Solar Energy: Global Data Sets*, NASA, 2016.
139. N. Sahraei, S. Watson, A. Pennes, Z. Ren, W.C. Khaw, F. Oviedo, P. Yen, I.M. Peters, and T. Buonassisi. "Design considerations for solar cell and battery of a persistent solar powered GPS tracker". in *26th International Photovoltaic Science and Engineering Conference*. 2016. Singapore.
140. S. Kurtz, John Wohlgemuth, P. Hacke, N. Bosco, M. Kempe, and R. Smith, "The Challenge to Move from "One Size Fits All" to PV Modules the Customer Needs", in *26th European Photovoltaic Solar Energy Conference and Exhibition*. 2011: Hamburg, Germany.

## Appendix 1: Publications

### Journal papers

- [1] **H. Liu**, A. M. Nobre, D. Yang, J. Y. Ye, F. R. Martins, R. Ruther *et al.*, "The Impact of Haze on Performance Ratio and Short-Circuit Current of PV Systems in Singapore," *IEEE Journal of Photovoltaics*, vol. PP, pp. 1-8, 2014.
- [2] F. J. Ma, **H. Liu**, B. Liao, J. Chen, Z. Du, G. Samudra *et al.*, "Impact of Auger recombination parameterisations on predicting silicon wafer solar cell performance," *Journal of Computational Electronics*, vol. 13, pp. 647-656, 2014.
- [3] **H. Liu**, Z. Ren, Z. Liu, A. G. Aberle, T. Buonassisi and I. M. Peters, "The realistic energy yield potential of GaAs-on-Si tandem solar cells: a theoretical case study," *Optics Express*, vol. 23, pp. A382-A390, 2015.
- [4] Z. Ren, J. P. Mailoa, Z. Liu, **H. Liu**, S. C. Siah, T. Buonassisi *et al.*, "Numerical Analysis of Radiative Recombination and Reabsorption in GaAs/Si Tandem," *IEEE Journal of Photovoltaics*, vol. 5, pp. 1079-1086, 2015.
- [5] A. M. Nobre, S. Karthik, **H. Liu**, D. Yang, F. R. Martins, E. B. Pereira *et al.*, "On the impact of haze on the yield of photovoltaic systems in Singapore," *Renewable Energy*, vol. 89, pp. 389-400, 2016.
- [6] **H. Liu**, A. G. Aberle, T. Buonassisi and M. Peters, "On the methodology of energy yield assessment for one-Sun tandem solar cells," *Solar Energy*, vol. 135, pp. 598-604, 2016.
- [7] **H. Liu**, Z. Ren, Z. Liu, A. G. Aberle, T. Buonassisi and I. M. Peters, "The predicted outdoor performance of several Si based tandem solar cells," manuscript in preparation.
- [8] Z. Liu, Z. Ren, **H. Liu**, N. Sahraei, F. Lin, R. Stangl, A. Aberle, T. Buonassisi, and I.M. Peters, "A Detailed Current Loss Analysis for Stacked 4-Terminal Tandem Solar Cells," *IEEE Journal of Photovoltaics*, under review, 2016.

## Conference papers

- [1] **H. Liu**, Z. Ren, Z. Liu, R. E. Brandt, J. P. Mailoa, S. C. Siah *et al.*, "Theoretical energy yield of GaAs-on-Si tandem solar cells," *MRS Online Proceedings Library*, vol. 1638, 2014.
  
- [2] A.G. Aberle, **H. Liu**, A. Nobre, Z. Ren, T. Buonassisi and I. M. Peters, "Design criteria of GaAs on silicon tandem solar cells for terrestrial applications," in *Light, Energy and the Environment*, Canberra, 2014.
  
- [3] **H. Liu**, A. Nobre, D. Yang, J. Y. Ye, F. R. Martins, R. R  ther *et al.*, "The impact of haze on performance ratio and short-circuit current of PV systems in Singapore," in Technical Digest of the 6th World Conference on Photovoltaic Energy Conversion, Kyoto, Japan, 2015.
  
- [4] Z. Liu, Z. Ren, **H. Liu**, J.P. Mailoa, N. Sahraei, S.C. Siah, S.E. Sofia, L. Fen, T. Buonassisi and I.M. Peters. "Light management in mechanically-stacked GaAs/Si tandem solar cells: Optical design of the Si bottom cell," in *42nd IEEE Photovoltaic Specialist Conference*, New Orleans, USA, 2015.
  
- [5] **H. Liu**, Z. Ren, Z. Liu, A. Aberle, T. Buonassisi, and I.M. Peters. "Predicted outdoor energy yield of Si based tandem solar cells," in *43rd IEEE Photovoltaic Specialist Conference*, Portland, USA, 2016.
  
- [6] Z. Liu, Z. Ren, **H. Liu**, N. Sahraei, F. Lin, R. Stangl, T. Buonassisi and I.M. Peters. "Optical Loss Analysis of Four-Terminal GaAs/Si Tandem Solar Cells". in *43rd IEEE Photovoltaic Specialist Conference*, Portland, USA, 2016.

## Appendix 2: MatLab code for yield calculation

```
function intYieldCalc

% integrated code for fast yield calculation based on spec matrix and
% efficiency matrix methodology.
% author: Liu Haohui, NUS
% V3.8

% V3.0: now able to set temperature;
% V3.1: support batch studies with multiple illumination inputs;
% included the capacity to perform data filter;
% removed load spectrum as a task switch;
% V3.2: made improvement to user input;
% V3.3: small change to user input, fixed some bugs;
% V3.4: included temperature sorting in distribution function generation
% V3.5: included insolation distribution with temperature calculation
% V3.6: change temperature to ambient temperature, modify effMatrix based
% on a temperature model to predict outdoor cell temperature (analytic change);
% V3.7: effective Ross coefficient k is set for each tandem configuration;
% V3.8: some bug fix
% V3.8a: for methodology study

% program outline: load source spectrum --> sort spectrum and provide stats
% on it --> generate spec matrix for efficiency matrix calculation &
% generate distribution function of illumination conditions --> calculate
% energy output of the specified cell configuration --> convert to
% efficiency matrix --> from eff matrix and distribution function,
% calculate yield.
% switch on required steps based on need.

%
*****
% ----- user input -----
%
*****

for month=1:12

    if month<10
        mth = ['0' num2str(month)];
    else
        mth = num2str(month);
    end

    % ~~~~~ general input ~~~~~
    wRange = [350 1060]; %specifies start and end of wavelength range considered
    defaultTemp = 25+273.15; % default: room temperature of 25C is 298.15K
    str = ['Denver2013' mth];
    studyName = [str '_GS_1st7days_smartsIrrMod'];
```

```

caseNum = 7; %total number of cases in this study
version = cell(caseNum,1);
others = cell(caseNum,1);
spec_case = cell(caseNum,1);

% ~~~~~ illumination (spec data) input ~~~~~
% spec_data is required for specMatrix and distribution function generation
spec_data = cell(caseNum,1);
prop_data = cell(caseNum,1);
% path('Z:\05 Data\01 Sunspectra\SINGAPORE SPECTRUM DATA\processed
spectrum data',path)
% path('Z:\05 Data\01 Sunspectra\SINGAPORE SPECTRUM DATA',path)
path('Z:\05 Data\01 Sunspectra\Denver spectrum data\processed spectrum data',path)
% ===== perform data filtering here if required =====
% raw_data = xlsread([str 'g' '.xlsx']); %work with version g for data filtering &
extraction
% wavelength = xlsread('wavelength.xlsx');
raw_data = xlsread('SMARTS spec Dv_IrrMod2013.xlsx'); %work with smart
generated spectra
wavelength = 280:1200;
m=2; %column of month
d=3; %column of day
t=4; %column of time
tem=7; %column of temperature
ins=8; %column of inso
s=5; %9; %start column of data
dayLabel = cell(caseNum,1);
% spec_file = cell(caseNum,1);
for caseIndex=1:caseNum
    spec_case{caseIndex} = str;
    version{caseIndex} = 'g'; %version of density function (version of spectrum data)
    others{caseIndex} = ['1st7' '0' num2str(caseIndex)]; %'_1stWeek'; %additional
attributes;
    % spec_file{caseIndex} = [spec_case{caseIndex} version{caseIndex} '.xlsx']; %if any

    % filter out spec data needed
    pickMonth = (raw_data(:,m)==month); %for SMARTS spec
% if month==8 %take care of data irregularity in Denver2014
% firstDay = 4; %skip 213 to 215, start from day 4
% else
% firstDay = raw_data(1,d);
% end
    pickDay = (raw_data(:,d)-firstDay+1==caseIndex); %pick day (first 7 days)
% pickDay = (raw_data(:,d)-firstDay+1<=7); %pick day (first week)
% pickDay = (raw_data(:,d)-firstDay+1<=31); %pick day (monthly, i.e. no day
filtering)
% pick = pickDay==1; %no time filtering
pick = pickDay==1 & pickMonth==1; %no time filtering for SMARTS spec (always
1 hr)
% pickTime = (mod(raw_data(:,t),100)==0 | mod(raw_data(:,t),100)==30); %pick
time (30 min interval)

```

```

% pickTime = (mod(raw_data(:,t),100)==0); %pick time (1 hr interval)
% pickTime = (mod(raw_data(:,t),100)==0 & mod(raw_data(:,t),200)~=0); %pick
time (2 hr interval)
% pick = pickTime==1 & pickDay==1; % with time filtering
% pick = pickTime==1 & pickDay==1 & pickMonth==1; % with time filtering for
SMARTS spec (not considered)
temp1 = 1:size(raw_data,1);
dayLabel{caseIndex} = temp1(pick);
assignin('base','dayLabel',dayLabel);
if isempty(dayLabel{caseIndex})
    warning('no data is selected in day %s',num2str(caseIndex))
end
spec_select = raw_data(dayLabel{caseIndex},s:end);
inso_select = raw_data(dayLabel{caseIndex},ins);
Tamb_select = raw_data(dayLabel{caseIndex},tem);
spec_data{caseIndex} = [wavelength' spec_select'];
prop_data{caseIndex} = [Tamb_select inso_select];
end
% ===== load spec_data directly if no filtering is needed =====
% for caseIndex=1:caseNum
% version{caseIndex} = 'g'; %version of density function (version of spectrum data)
% others{caseIndex} = "; %additional attributes, add '_' in front;
% spec_case{caseIndex} = str;
%
% spec_select = [];
% Tamb_select = [];
% inso_select = [];
% wavelength = xlsread('wavelength.xlsx');
% if iscolumn(wavelength)
%     wavelength = wavelength';
% end
% for m=1:12
%     if m<10
%         mth = ['0' num2str(m)];
%     else
%         mth = num2str(m);
%     end
%     specRead = xlsread([str mth version{caseIndex} '.xlsx']);
%     spec_select = [spec_select specRead(:,9:end)'];
%     inso_select = [inso_select; specRead(:,8)]; %reads global irradiance
%     Tamb_select = [Tamb_select; specRead(:,7)]; %reads ambient temperature
% end
%
% spec_data{caseIndex} = [wavelength spec_select];
% prop_data{caseIndex} = [Tamb_select inso_select];
% clear spec_select;
%
% % spec_data{caseIndex} = xlsread([str '.xlsx']);
% end

```

```

% ~~~~~ input for DF yield calculation ~~~~~
APErange = [1.7 1.75 1.8 1.85:0.01:1.95 2:0.05:2.15]; %the APE range in efficiency
matrix, row vector
insoRange = 0.1:0.1:1.3;
%in no. of suns, matches the range in efficiency matrix, row vector, right end must be
larger than 1;
tempRange = -10:60; %in deg C
duration = 60; %duration for each spectrum in min

% ~~~~~ device input ~~~~~
tandem_model = 'GaAs/Si'; %further specify sub-cell models below
config = '2T'; %either 2T or 4T or SJ

% ~~~~~ task switches ~~~~~
specMatrixGen = 0; %generate specMatrix (required for deviceSim) from spec_data
% ===== load SpecMatrix manually here if required =====
% SpecMatrix = xlsread(spec_file);
% load('SpecMatrix_InS_Gen2Perc_2TDenver2014g.mat');
% SpecMatrix = SpecMatrix(:,[1 202:end]);
% SpecMatrix = spec_data{1};
% tempList = (25:50)+273.15;
% SpecMatrix = [SpecMatrix(:,1) repmat(SpecMatrix(:,2),1,length(tempList))];

DFuncGen = 1; %generate distribution function (required for yieldCalc)
% no need to load here, make sure "DFunc_" file exist.

tempEff_dsim = 0; %whether to include temperature effect in device simulation.

deviceSim = 0; %perform device simulation (results containing device output required
for effMatrixGen)

modT = 0;

effMatrixGen = 0; %generate efficiency matrix (required for yieldCalc)
% ===== load effMatrix here if required =====
load('effMatrix_GS_BhPerc_2TDenver2014g.mat');

yieldCalc = 1; %calculate final yield and harvesting efficiency

saveCaseStudy = 0; %save workspace of current case as a .mat file

deleteFiles = 1; %delete generated intermediate files

saveStudy = 1; %save study_summary of this study

% ~~~~~ tandem/SJ cell model library ~~~~~
% further specify detailed structures inside respective functions

```

```

switch tandem_model
case 'GaAs/Si'
    %GaAs/Si model
    cell_model = {'GaAs_bauhuis.prm';'Si_perc.prm';'GS_BhPerc_'};
    if strcmp(config,'2T')
        %in nm, scnprt current mathced = 200 (Am1.5G) / 215 (Am1.5D) / 170 (Sg
spectrum), 4T = 1000
        TopThickness = 215; %#ok<*NASGU>
        k = 0.0200531;
    else
        TopThickness = 1000;
        k = 0.0185371;
    end
case 'InGaP/Si'
    %InGaP/Si model
    cell_model = {'InGaP_gen2.prm';'Si_perc.prm';'InS_Gen2Perc_'};
    TopThickness = 2500; %in nm, scnprt current mathced = 1500 (Am1.5G) / 2600
(Am1.5D) / (Sg spectrum)
    if strcmp(config,'2T')
        k = 0.0198218;
    else
        k = 0.0196741;
    end
case 'InGaP/GaAs/Si'
    cell_model
    =
    {'InGaP_gen2.prm';'GaAs_bauhuis.prm';'Si_perc.prm';'InGS_Gen2BhPerc_'};
    TopThickness = 285; %in nm, scnprt current mathced = 250 (Am1.5G) / 285
(Am1.5D) / (Sg spectrum)
    MidThickness = 650; %in nm, scnprt current mathced = 530 (Am1.5G) / 570
(Am1.5D) / (Sg spectrum)
    k = 0.0192015;
case 'GaAs/GaAs/Si'
    cell_model = {'GaAs_bh3J.prm';'Si_perc.prm';'GGS_BhBhPerc_'};
    TopThickness = 95; %in nm
    MidThickness = 450; %in nm
    k = 0.0189295;
case 'GaAs'
    cell_model = {'GaAs_bauhuis.prm';'GaAs_Bh_'};
    config = 'SJ';
    Thickness = 2000;
    k = 0.0199089;
case 'InGaP'
    cell_model = {'InGaP_danny.prm';'InGaP_Dan_'};
    config = 'SJ';
    Thickness = 1000;
%    k = 0.0196741;
case 'Si'
    cell_model = {'Si_perc.prm';'Si_perc_'};
    config = 'SJ';
    Thickness = 200000;
    k = 0.0238768;

```



```

        otherwise
            warning('choice of model not in the current library')
        end

    %
    %*****
    % ----- end of input -----
    %
    %*****

    study_summary = cell(caseNum,4);

    for caseIndex=1:caseNum

        % case label
        caseName = [cell_model{end} config spec_case{caseIndex} version{caseIndex}
others{caseIndex}];
        study_summary{caseIndex,1} = caseName;
        % assignin('base','caseName',caseName);

        % generate spec matrix
        if specMatrixGen

            spectrumSort(spec_data{caseIndex},APERange,wRange,prop_data{caseIndex}); % wavelength
            h and APE info are returned from this function
            if max(APE)<APERange(end-1) || min(APE)>APERange(2)
                warning('empty APE bins present, program will not execute correctly, please
terminate and redefine APE range')
            end
            N = length(APERange)-1; %last APE value not included, interval represented by the
left end

            % obtain weighted avgerage spectra from sorted spectra, then create
            % spec matrix
            SpecMatrix = [];
            for j=1:N
                selectSpec = load(['SpecSort_' num2str(APERange(j)) 'eV-'
num2str(APERange(j+1)) 'eV.dat']);
                if size(selectSpec,2)==1
                    warning('the following bin is empty: %s eV to %s eV, please
terminate',num2str(APERange(j)),num2str(APERange(j+1)))
                end
                avgSpectrum = WgtAvgSpec(selectSpec,'true');
                if j==1
                    WgtAvgSpectrum = avgSpectrum;
                else
                    WgtAvgSpectrum = [WgtAvgSpectrum avgSpectrum(:,2)];
                end

                specBlock = [];
                for i=length(inoRange):-1:1

```

```

        specBlock = [specBlock WgtAvgSpectrum(:,j+1)*insoRange(i)];
    end
    SpecMatrix = [SpecMatrix specBlock];
end

SpecMatrix = [wavelength SpecMatrix];
save(['SpecMatrix_' caseName '.mat'],'SpecMatrix')

% delete('SpecSort_*.dat');
% delete('PropSort_*.dat');
clear selectSpec avgSpectrum WgtAvgSpectrum specBlock N i j
end

% generate distribution function
if DFuncGen
    APERange_DF = APERange(1):0.01:APERange(end);
    insoRange_DF = 0:0.02:insoRange(end); %in no. of suns, any desired resolution
    tempRange_DF = tempRange; %in deg C

spectrumSort(spec_data{caseIndex},APERange_DF,wRange,prop_data{caseIndex});
    [distributionCount,TempDistributionCount_DF] =
DFcount(APERange_DF,insoRange_DF,tempRange_DF,k); % occurrence
    durationFunc = distributionCount*duration; %in min per APE and inso spacing
    densityFunc = distributionCount/sum(sum(distributionCount)); %density
distribution
    tempDistribution =
createTempMatrix(TempDistributionCount_DF,tempRange_DF);

    if ~specMatrixGen
        spectrumSort(spec_data{caseIndex},APERange,wRange,prop_data{caseIndex});
    end

    [~,TempDistributionCount] =
DFcount(APERange,insoRange,tempRange,k); % occurrence, temp distribution for input into
effMatrix generation
    tempMatrix = createTempMatrix(TempDistributionCount,tempRange);

    save(['DFunc_' caseName
.mat'],'APERange_DF','insoRange_DF','tempRange_DF','distributionCount','durationFunc','de
nsityFunc','TempDistributionCount_DF','tempDistribution','tempMatrix')

    delete('SpecSort_*.dat');
    delete('PropSort_*.dat');
end

% perform device simulation, input spec is always termed SpecMatrix
if deviceSim
    if tempEff_dsim
        tempMatrix2 = [tempMatrix tempMatrix(:,end)];
        tempList = [];
    end
end

```

```

        for r=1:size(tempMatrix2,1)
            tempList = [tempList fliplr(tempMatrix2(r,:))+273.15];
        end
    else
        tempList = repmat(defaultTemp,1,(length(APErange)-1)*length(insoRange));
        disp('reminder: no temperature effect is considered in device simulation.')
    end
end
switch tandem_model %#ok<*UNRCH>
    case 'GaAs/Si'

tandemGS(SpecMatrix,cell_model,config,caseName,TopThickness,tempList,wRange);
    case 'InGaP/Si'

tandemInS(SpecMatrix,cell_model,config,caseName,TopThickness,tempList,wRange);
    case 'InGaP/GaAs/Si'

tandemInGS(SpecMatrix,cell_model,config,caseName,TopThickness,MidThickness,tempList
,wRange);
    case 'GaAs/GaAs/Si'

tandemGGS(SpecMatrix,cell_model,config,caseName,TopThickness,MidThickness,tempList
,wRange);
    case 'GaAs'
        SJ_GaAs(SpecMatrix,cell_model,caseName,Thickness,tempList,wRange);
    case 'InGaP'
        SJ_InGaP(SpecMatrix,cell_model,caseName,Thickness,tempList,wRange);
    case 'Si'
        SJ_Si(SpecMatrix,cell_model,caseName,Thickness,tempList,wRange);
end
end

% modify efficiency by including temperature effect
if modT
    % consider only effect on voltage and FF, assume constant Jsc
    matList = ['InGaP' 'GaAs' 'Si'];
    V_coeff = [-1.9 -1.9 -2.2]*0.001;
    FF_coeff = [-0.08 -0.08 -0.13];
    load(['DFunc_' caseName '.mat']); %modified DFunc file from w/o T case already
exist
    tempMatrix2 = [tempMatrix tempMatrix(:,end)];
    tempDiffList = [];
    for r=1:size(tempMatrix2,1)
        tempDiffList = [tempDiffList fliplr(tempMatrix2(r,:))-25];
    end

    eff_data = load(['eff_' caseName(1:end-4) '.dat']); %assume w/o T case already exist

switch config
    case '2T'
        Jm = eff_data(:,end-1);

```

```

Vm = eff_data(:,end);
if size(eff_data,2)==15
    Voc = sum(eff_data(:,[3 7 11]),2);
    Jsc = min(eff_data(:,[2 6 10]),[],2);
    dV = sum(V_coeff(1:3))*tempDiffList;
    dFF = min(FF_coeff(1:3))*tempDiffList*0.01;
else
    Voc = sum(eff_data(:,[3 7]),2);
    Jsc = min(eff_data(:,[2 6]),[],2);
    dV = sum(V_coeff(2:3))*tempDiffList;
    dFF = min(FF_coeff(2:3))*tempDiffList*0.01;
end
FF = Jm.*Vm./(Voc.*Jsc);
Vm_new = (FF+dFF').*(Voc+dV').*Jsc./Jm;
P_new = Vm_new.*Jm;
eff_data(:,1) = P_new;
eff_data(:,end) = Vm_new;
save(['eff_' caseName '.dat'],'eff_data','-ascii');
case '4T'
% assume dual junction only
Vm1 = eff_data(:,5);
FF1 = eff_data(:,4).*Vm1./(eff_data(:,2).*eff_data(:,3));
Vm2 = eff_data(:,9);
FF2 = eff_data(:,8).*Vm2./(eff_data(:,6).*eff_data(:,7));
dV1 = V_coeff(2)*tempDiffList;
dV2 = V_coeff(3)*tempDiffList;
dFF1 = FF_coeff(2)*tempDiffList*0.01;
dFF2 = FF_coeff(3)*tempDiffList*0.01;
Vm1_new = (FF1+dFF1').*(eff_data(:,3)+dV1').*eff_data(:,2)./eff_data(:,4);
Vm2_new = (FF2+dFF2').*(eff_data(:,7)+dV2').*eff_data(:,6)./eff_data(:,8);
eff_data(:,1) = eff_data(:,4).*Vm1_new + eff_data(:,8).*Vm2_new;
eff_data(:,5) = Vm1_new;
eff_data(:,9) = Vm2_new;
save(['eff_' caseName '.dat'],'eff_data','-ascii');
case 'SJ'
Vm = eff_data(:,5);
FF = eff_data(:,4).*Vm./(eff_data(:,2).*eff_data(:,3));
dV = V_coeff(2)*tempDiffList; %***modify index here***
dFF = FF_coeff(2)*tempDiffList*0.01; %***modify index here***
Vm_new = (FF+dFF').*(eff_data(:,3)+dV').*eff_data(:,2)./eff_data(:,4);
eff_data(:,1) = eff_data(:,4).*Vm_new;
eff_data(:,5) = Vm_new;
save(['eff_' caseName '.dat'],'eff_data','-ascii');
%
%     eff=load('effMatrix_Si_perc_SJSingapore2014g.mat','effMatrix');
%     eff=eff.effMatrix;
%     effMatrix=eff-(tempMatrix2'-25)*0.00478.*eff;
end
end

% create efficiency matrix
if effMatrixGen

```

```

    effMatrix = createEffMat(caseName,APERange,insoRange);
    save(['effMatrix_' caseName '.mat'],'effMatrix','APERange','insoRange')
end

% calculate harvesting efficiency
if yieldCalc
    [har_eff,yield_total,inso_total] =
DFyieldCalc(caseName,APERange,insoRange,effMatrix);

    study_summary{caseIndex,2} = har_eff;
    study_summary{caseIndex,3} = yield_total;
    study_summary{caseIndex,4} = inso_total;
    assignin('base','har_eff',har_eff); %contains: final eff, eff with varying APE at 1sun
    efficiency, eff with varying intensity at std APE (or under AM1.5G)
    assignin('base','yield_total',yield_total);
    assignin('base','inso_total',inso_total);
end

if saveCaseStudy
    clear spec_data;
    clear prop_data;
    save([caseName '.mat'])
end

if deleteFiles
%     delete(['SpecMatrix_' caseName '.mat']);
%     delete(['effMatrix_' caseName '.mat']);
    delete(['DFunc_' caseName '.mat']);
%     delete(['eff_' caseName, '.dat']);
end

end

if saveStudy
    save([studyName '.mat'],'studyName','study_summary')
end

end
end

%
*****
% ----- auxiliary functions -----
%
*****

function spectrumSort(spec,APERange,wRange,prop)
% this function sorts spectra from standard processed spectral data files
% into bins of different APE values and writes them to dat files.
% provide a brief summary of spectrum property.

```

```

% select relevant wavelength range
wavelength = spec(spec(:,1)<wRange(2) & spec(:,1)>wRange(1),1);
wavelength = [wRange(1);wavelength;wRange(2)];
assignin('caller','wavelength',wavelength);
spectrum = interp1(spec(:,1),spec(:,2:end),wavelength);

% calculate APE for each time point and some simple descriptive stats
APE = APEcalc([wavelength spectrum]);
assignin('caller','APE',APE);
APE_mean = mean(APE);
assignin('caller','APE_mean',APE_mean);
APE_std = [std(APE) std(APE,1)];
assignin('caller','APE_std',APE_std);
disp(['average APE value for this spectrum data set is ' num2str(APE_mean) ' eV'])
range = linspace(min(APE),max(APE));
count = zeros(1,length(range)-1);
for j=1:length(range)-1
    count(j) = length(APE(APE>=range(j) & APE<range(j+1)));
end
% figure
% plot(range(1:end-1),count)
assignin('caller','range_APE',range);
assignin('caller','count_APE',count);

% sort spectra and write into data files for respective APE bins
for j=1:length(APERange)-1
    index = APERange(j)<=APE & APE<=APERange(j+1);
    selectSpec = spectrum(:,index);
    selectSpec = [wavelength selectSpec]; % spectrum is outputted in std format

    dlmwrite(['SpecSort_' num2str(APERange(j)) 'eV-' num2str(APERange(j+1))
'eV.dat'],selectSpec,'delimiter','\t');
    if ~isempty(prop)
        selectProp = prop(index,:);
        dlmwrite(['PropSort_' num2str(APERange(j)) 'eV-' num2str(APERange(j+1))
'eV.dat'],selectProp,'delimiter','\t');
    end
end

% collect out of APERange spectra
index = APERange(end)<=APE | APE<=APERange(1);
selectSpec = spectrum(:,index);
selectSpec = [wavelength selectSpec]; % spectrum is outputted in std format
% selectProp = prop(index,:);
dlmwrite(['SpecSort_outside ' num2str(APERange(1)) 'eV-' num2str(APERange(end))
'eV.dat'],selectSpec,'delimiter','\t');

missing_ISI = sum(trapz(wavelength,selectSpec(:,2:end)))/3.6e6;
warning('Total number of out of APERange spectra is %s, total ISI = %s
kWh/m2',num2str(size(selectSpec,2)-1),missing_ISI)

```

```

end

function avgSpectrum=WgtAvgSpec(spec,scale)
% this function calculates the weighted average spectrum (scaled to AM1.5G)
% given a set of spectra in std format. The output spectrum can be scaled with
% AM1.5G spectrum in the given wavelength range (so final spectrum can be
% seen as 1sun).

wavelength = spec(:,1);
spectrum = spec(:,2:end);
inso = trapz(wavelength,spectrum);
insoSum = sum(inso);
avgSpectrum = zeros(length(wavelength),1);

%obtain weighted avg spectrum
for i=1:size(spectrum,2)
    avgSpectrum = avgSpectrum + spectrum(:,i)/insoSum*inso(i);
end

if strcmp(scale,'true')
%scale the avg spectrum to that of AM1.5G
path('Z:\99 home\02 PhD students\05 Haohui\Source & materials\useful
parameters',path)
[AM15spec, ~] = xlsread('solar spectrum.xls','Spectra');
lambda = AM15spec(:,1); %in nm
AM15G = AM15spec(:,3); %select global tilt spectrum
specStd = interp1(lambda,AM15G,wavelength);
insoStd = trapz(wavelength,specStd); %AM1.5G intensity in the same wavelength range
as given spectra

ISI = trapz(wavelength,avgSpectrum);
avgSpectrum = avgSpectrum/ISI*insoStd;
end

avgSpectrum = [wavelength avgSpectrum];

end

function
[distributionCount,TempDistributionCount]=DFcount(APERange_DF,insoRange_DF,tempRa
nge,k)
% this function returns occurrence counts of spectra falling in a certain APE
% and intensity range. Intensity is in no. of suns. Wavelength range of
% spectroradiometer is taken care of by comparing with AM1.5G in the same
% wavelength range.
% distribution function has the dimension of APE(row) X Intensity(col)

N = length(APERange_DF)-1;
M = length(insoRange_DF)-1;
distributionCount = [];
propFile = dir('PropSort_*');

```

```

TempDistributionCount = cell(N,M);

path('Z:\99 home\02 PhD students\05 Haohui\Source & materials\useful
parameters',path)
[AM15spec, ~] = xlsread('solar spectrum.xls','Spectra');
lambda = AM15spec(:,1); %in nm
AM15G = AM15spec(:,3); %select global tilt spectrum

for j=1:N
    spec = load(['SpecSort_' num2str(APERange_DF(j)) 'eV-'
num2str(APERange_DF(j+1)) 'eV.dat']);
    if ~isempty(propFile)
        prop = load(['PropSort_' num2str(APERange_DF(j)) 'eV-'
num2str(APERange_DF(j+1)) 'eV.dat']);
    end

    count = zeros(1,length(insoRange_DF)-1); %frequency counts of certain intensity
    if size(spec,2)>1
        wavelength = spec(:,1);
        spectrum = spec(:,2:end);
        inso = trapz(wavelength,spectrum);
        specStd = interp1(lambda,AM15G,wavelength);
        insoStd = trapz(wavelength,specStd); %AM1.5G 1sun intensity in the same
wavelength range as given spectra

        for i=1:length(count)
            index = (inso>=(insoStd*insoRange_DF(i)) &
inso<(insoStd*insoRange_DF(i+1)));
            count(i) = length(inso(index));

            if ~isempty(propFile)
                tempSelect = prop(index,1)+prop(index,2)*k; %simple linear model using
effective ross coefficient
                tempCount = zeros(length(tempRange)-1,1);
                for t=1:length(tempRange)-1
                    if count(i)~=0
                        tempCount(t) = length(tempSelect((tempSelect(:,1)>=tempRange(t) &
tempSelect(:,1)<=tempRange(t+1)),1));
                    end
                end
                TempDistributionCount{j,i} = tempCount;
            end
        end
    end
    distributionCount = [distributionCount; count];
end

end

function effMatrix=createEffMat(caseName,APERange,insoRange)

```



```

M = length(APERange)-1;
N = length(insoRange);
effMatrix = [];

yield_data = load(['eff_' caseName '.dat']);
yield = yield_data(:,1);

for i=1:M
    index1 = 1 + (i-1)*N;
    index2 = i*N;
    effMatrix = [effMatrix;
fliplr(yield(index1:index2))./insoRange(1:end)/10]; %#ok<*AGROW>
end

effMatrix = effMatrix'; % X-axis: APE, Y-axis: intensity

end

function
[har_eff,yield_total,inso_total]=DFyieldCalc(caseName,APERange,insoRange,effMatrix)
% Yield calculation using density (duration) function method

X = APERange(1:end-1);
Y = insoRange';
[X,Y] = meshgrid(X,Y);
Z = effMatrix;

% load density function and interpolate efficiency
load(['DFunc_' caseName '.mat']);
XI = APERange_DF(1:end-1); %#ok<*COLND>
YI = insoRange_DF(1:end-1)';
ZI = interp2(X,Y,Z,XI,YI,'spline');

% compute yearly total insolation implied in the distribution
% compute yield and harvesting efficiency
% eff * # of suns * 1000w/m2 * duration in min * 60s/min = energy yield for that
condition
durationVsAPE = [XI' sum(durationFunc,2)];
assignin('caller','durationVsAPE',durationVsAPE);
durationVsIntensity = [YI' sum(durationFunc,1)'];
assignin('caller','durationVsIntensity',durationVsIntensity);
inso = repmat(YI,1,length(XI)).*1000.*durationFunc'.*60./3.6e6; %insolation
distribution in each small APE and intensity interval, in kWh/m2
assignin('caller','inso_yr',inso);
insoVsAPE = [XI' sum(inso,1)'];
assignin('caller','insoVsAPE',insoVsAPE);
insoVsIntensity = [YI' sum(inso,2)'];
assignin('caller','insoVsIntensity',insoVsIntensity);
for h=1:length(tempRange_DF)-1
    indexT = tempDistribution'>=tempRange_DF(h) &
tempDistribution'<tempRange_DF(h+1);

```

```

        insoTemp(h) = sum(inso(indexT));
    end
    insoVsTemp = [tempRange_DF(1:end-1)' insoTemp']; %describes how much insolation
is associated with each temperature
    assignin('caller','insoVsTemp',insoVsTemp);
    tempVsInso = sum(tempDistribution'.*inso,2)./sum(inso,2);
    tempVsInso(isnan(tempVsInso))=25;
    assignin('caller','tempVsInso',tempVsInso);
    yield = ZI.*0.01.*inso; %in kWh/m2
    assignin('caller','yield',yield);
    yieldVsAPE = [XI sum(yield,1)'];
    assignin('caller','yieldVsAPE',yieldVsAPE);
    yieldVsIntensity = [YI sum(yield,2)'];
    assignin('caller','yieldVsIntensity',yieldVsIntensity);
    yield_total = sum(sum(yield));
    yield_1sun = repmat(ZI(abs(YI-1)<0.0001,:),length(YI),1).*0.01.*inso;
    yield_1sun = sum(sum(yield_1sun));
    % yield_stdAPE = repmat(ZI(:,abs(XI-1.87)<0.0001),1,length(XI)).*0.01.*inso;
    % yield_stdAPE = sum(sum(yield_stdAPE));

    inso_total = sum(sum(inso)); %in kWh/m2
    har_eff = zeros(1,2);
    har_eff(1) = yield_total/inso_total*100;
    har_eff(2) = yield_1sun/inso_total*100;
    % har_eff(3) = yield_stdAPE/inso_total*100;

    % ----- backup code for calculating har eff by varying intensity under AM1.5G ---
    % ----- only useful when eff_am15gSpecMatrix is available -----

    %
    %           effMatrix_AM15G=createEffMat([cell_model{end}           config
'am15gSpecMatrix'],1.87:0.01:1.88,0.1:0.1:1.5);
    % ZIstd = interp1(0.1:0.1:1.5,effMatrix_AM15G,YI,'pchip','extrap');
    % yield_am15g = repmat(ZIstd,1,length(XI)).*0.01.*inso;
    % yield_am15g = sum(sum(yield_am15g));
    % har_eff(3) = yield_am15g/inso_total*100;

end

function APE=APEcalc(spec)
% this function calculates APE values
% spec format is in [wavelength spectrum1 spectrum2 ...]
% returns APE values for each spectrum
% need to ensure match of units, ISI need to be in w/m2

h = 6.63e-34;
c = 3e8;
q = 1.6e-19;

wavelength = spec(:,1);
spectrum = spec(:,2:end);
isi=trapz(wavelength,spectrum);

```

```

isi = isi'; % ISI for each time point in w/m2
Nphoton = zeros(size(spectrum,2),1);
APE = zeros(size(spectrum,2),1);
for i=1:size(spectrum,2)
    flux = spectrum(:,i).*wavelength./(h*c); % photon flux
    Nphoton(i) = trapz(wavelength*1e-9,flux);
    APE(i) = isi(i)/Nphoton(i)/q; % APE in the wavelength range specified in the spectrum
end

end

```

```

function tempMatrix=createTempMatrix(PropDistributionCount,tempRange)
% this function creates property matrix
% V1: only tempMatrix is created

```

```

tempMatrix = repmat(25,size(PropDistributionCount)); %default temperature is 25 deg

```

C

```

%obtain tempMatrix by picking the weighted average of each cell
for r=1:size(PropDistributionCount,1)
    for col=1:size(PropDistributionCount,2)
        tempDistr = PropDistributionCount{r,col};
        if sum(tempDistr)~=0
            wgtAvgTemp = sum(tempDistr'.*tempRange(1:end-1))/sum(tempDistr);
            tempMatrix(r,col) = wgtAvgTemp;
        end
    end
end
end

end

```